

**University of Alberta**

**Electrodeposition of iron-cobalt alloys from a dibasic ammonium  
citrate stabilized plating solution**

by

**Brendan M. Crozier**

A thesis submitted to the Faculty of Graduate Studies and Research  
in partial fulfillment of the requirements for the degree of

Master's of Science

in

Materials Engineering

Department of Chemical and Materials Engineering

©Brendan. M. Crozier

Fall 2009

Edmonton, Alberta

Permission is hereby granted to the University of Alberta Libraries to reproduce single copies of this thesis and to lend or sell such copies for private, scholarly or scientific research purposes only. Where the thesis is converted to, or otherwise made available in digital form, the University of Alberta will advise potential users of the thesis of these terms.

The author reserves all other publication and other rights in association with the copyright in the thesis and, except as herein before provided, neither the thesis nor any substantial portion thereof may be printed or otherwise reproduced in any material form whatsoever without the author's prior written permission.

## Abstract

Iron-cobalt alloys have been extensively studied as potential hard disk drive write head materials due to their potentially high saturation flux densities ( $\sim 2.4\text{T}$ ), low coercivities and ease of deposition. Iron-cobalt plating solutions have, however, been shown to have stability issues, necessitating that they be used at low pH or that a stabilizing agent be added to the solution.

The purpose of this thesis is to evaluate the stability of a dibasic ammonium citrate plating solution and to characterize the deposits which result from its use.

The plating solutions are found to be less stable than previously claimed. The solutions are oxidized by dissolved oxygen, which leads to a valence change in the iron ions and eventually the formation of iron oxide/hydroxide precipitates. These effects are exacerbated by heating or the application of a voltage across the solution. Deposits plated from the solution are fine grained ( $<40\text{nm}$ ) and compact through their thickness. While normally deposited as the equilibrium BCC phase, metastable phases are deposited at elevated temperatures, high pH or in the absence of a stabilizing agent. A metastable phase which is isomorphous to  $\alpha\text{-Mn}$  is deposited at elevated temperatures. This phase transforms to the BCC phase when annealed at  $>174^\circ\text{C}$  and is highly textured. Its presence is detrimental to deposit coercivity.

## **Acknowledgements**

I would like to express my sincere and a heartfelt appreciation to everyone who has helped me with my research over the course of my M.Sc. degree.

I would in particular to like thank Dr. Ivey and Dr. Liu for their guidance and advice over the course of my university career. Their help was indispensable and I wish them the best in their future endeavors.

I would also like to thank Tina Baker for operating the scanning electron microscope and Shiraz Merali for training me on the use of the x-ray diffractometer. Yu XiaoLan at Sun Yat-Sen Univeristy in China made all of the magnetic measurements presented in this thesis. The help of Walter Boddez, with respect to the design of the annealing furnace which was used, is also greatly appreciated.

I would like to thank the people at the Alberta Centre for Surface Engineering and Science (ACSES), and in particular Anqiang He, for taking the x-ray photoelectron spectroscopy (XPS) measurements and for training me on use of the profilometer. Micralyne Ltd. and the NanoFab at the University of Alberta are also acknowledged for providing the metallized silicon substrates and for access to the dicing saw, respectively. I would also like to thank the Natural Sciences and Engineering Research Council of Canada (NSERC) for funding my project.

Finally, I'd like to thank my fellow graduate students who were there to help me both academically and personally during my university career. I wish you all the best with regards to your own graduate degrees and in your future careers.

# Table of Contents

<b>CHAPTER 1</b>	<b>INTRODUCTION.....</b>	<b>1</b>
<b>CHAPTER 2</b>	<b>BACKGROUND.....</b>	<b>4</b>
2.1	Background .....	4
2.1.1	Hard Disk Drives .....	4
2.1.2	Thin film write-heads.....	8
2.2	Magnetism.....	14
2.2.1	Magnetic Properties and Units.....	14
2.2.2	Types of Magnetism.....	17
2.2.2.1	Diamagnetic materials .....	18
2.2.2.2	Paramagnetic materials .....	19
2.2.2.3	Ferromagnetic materials.....	20
2.2.2.4	Antiferromagnetic materials .....	21
2.2.2.5	Ferrimagnetic materials .....	22
2.2.3	Ferromagnetism .....	22
2.2.3.1	Domain Theory .....	22
2.2.3.2	Magnetization .....	24
2.2.3.3	Magnetic Hysteresis.....	25
2.2.3.4	Anisotropy.....	27
2.3	Electrodeposition .....	32
2.3.1	The Electroplating Cell .....	32
2.3.2	Deposition rate and current efficiency .....	34
2.3.3	Electrode potentials.....	35
2.3.3.1	Overpotential.....	36
2.3.4	Metal Deposition.....	40
2.3.5	Alloy co-deposition.....	42
2.3.6	Pulse Electrodeposition.....	44
2.4	Soft-Magnetic Thin-Film .....	50
2.4.1	Electrodeposition of thin-films for write heads .....	50
2.4.2	Iron-cobalt thin-films .....	52
2.4.2.1	Previous research on iron-cobalt thin-films .....	54
2.5	Objectives of the research work.....	65
<b>CHAPTER 3</b>	<b>EXPERIMENTAL PROCEDURE.....</b>	<b>66</b>
3.1	Electroplating cell .....	66
3.1.1	Standard electroplating solution and conditions .....	68
3.1.1.1	Variations on plating solution and parameters.....	69



3.2	Magnetic Annealing.....	70
3.2.1	Annealing furnace and sample holder.....	70
3.2.2	Magnetic annealing parameters .....	73
3.3	Characterization and analysis.....	75
<b>CHAPTER 4 RESULTS AND DISCUSSION.....</b>		<b>77</b>
4.1	Stability of dibasic ammonium citrate plating solutions.....	77
4.1.1	Long term stability of dibasic ammonium citrate stabilized solutions .....	77
4.1.1.1	Effects of dissolved oxygen on solution stability .....	81
4.1.1.2	Effects of aging on solution pH .....	83
4.1.2	Stability of dibasic ammonium citrate stabilized solutions during use .....	87
4.2	Characterization of Iron-Cobalt Thin Films.....	89
4.2.1	Effects of plating temperature on iron-cobalt thin films.....	89
4.2.1.1	Composition of iron-cobalt deposits .....	89
4.2.1.2	Morphology of iron-cobalt deposits.....	91
4.2.1.3	Phases in iron-cobalt deposits.....	94
4.2.2	Effects of current density on iron-cobalt thin-films.....	102
4.2.3	Transmission electron microscopy.....	104
4.3	Annealing of iron-cobalt deposits .....	111
4.3.1	Deposit morphology.....	111
4.3.2	Phase composition.....	115
4.3.2.1	Effects of annealing temperature .....	115
4.3.2.2	Effects of applied magnetic field during annealing .....	117
4.3.3	TEM analysis of annealed deposits.....	120
4.3.3.1	TEM analysis of deposits plated at 20°C and then annealed .....	120
4.3.3.2	TEM analysis of deposits plated at 60°C after annealing .....	124
4.4	Magnetic properties of iron-cobalt thin films .....	129
4.4.1	Saturation flux density of iron-cobalt thin films .....	131
4.4.2	Coercivity of iron-cobalt thin films .....	134
<b>CHAPTER 5 CONCLUSIONS AND RECOMMENDATIONS FOR FUTURE WORK.....</b>		<b>139</b>
5.1	Summary of research results and conclusions .....	139
5.2	Recommendations for future work .....	148
<b>APPENDIX A GIBBS FREE ENERGY CALCULATIONS.....</b>		<b>150</b>

*REFERENCES* .....154

## List of Tables

Table 2-1: Units of magnetic properties in cgs and S.I. systems .....	14
Table 2-2: A summary of different magnetic behaviours [Birmingham09]. .....	18
Table 2-3: Standard electrode potentials [Milazzo78]. .....	36
Table 2-4: Equilibrium phases of iron-cobalt binary system [Betteridge82, Baker92, Crystal04]. .....	53
Table 3-1: Composition of standard electroplating solution. ....	69
Table 4-1: Composition of iron-cobalt thin films plated at various temperatures. ....	90
Table 4-2: Oxygen composition of iron-cobalt deposits at various temperatures. ....	90
Table 4-3: Average thickness of iron-cobalt deposits at various temperatures. ....	93
Table 4-4: Approximate lattice parameters of electrodeposited phases. ....	96
Table 4-5: Oxygen contents of iron-cobalt deposits plated from un-stabilized plating solutions using XPS. ....	99
Table 4-6: The coefficients of thermal expansion of materials present in the iron-cobalt deposits at 20°C [Bonnenberg80 <sup>a</sup> , Bauccio93 <sup>b</sup> ]. ....	112
Table 4-7: Estimated volume loss for iron-cobalt deposit due to cracking and delamination after annealing. ....	130
Table A-1: Gibbs free energy of formation of chemical species [Alberty97 <sup>a</sup> , Garrelts65, Diakonov94 <sup>c</sup> ] .....	150

## List of Figures

Figure 2-1: Hard disk drive with structures labeled [BBC07].	4
Figure 2-2: Schematic cross-section of a thin-film hard disk platter [Wang99].	5
Figure 2-3: Longitudinal magnetization of recording medium by a write head [Computer06].	6
Figure 2-4: Evolution of areal density in hard disk drives [Cooper05].	7
Figure 2-5: Schematics of IBM 3370 read/write-head: a) cross-sectional schematic showing the magnetic layers (A), pole tips (B), copper coil (C), gap layer (D), and electrical insulation layers (E); b) planar view of read/write-head; c) pole tips at air-bearing surface [Chiu96].	9
Figure 2-6: Inductive write head [Daniel98].	10
Figure 2-7: Thin-film fabrication of write heads; corresponds to steps 1-6 in the text [Mallinson97].	12
Figure 2-8: Final dicing and mounting of write heads; corresponds to steps 7-9 in the text [Mallinson97].	13
Figure 2-9: Variation of susceptibility with temperature for paramagnetic materials.	19
Figure 2-10: Magnetization and susceptibility curves below and above the Curie temperature [Cullity72]. Saturation magnetization ( $\sigma_s$ ) describes the maximum magnetization for a material at a particular temperature and $\sigma_0$ is the magnetization at 0K.	21
Figure 2-11: Possible domain structures for unmagnetized ferromagnetic crystals.	23
Figure 2-12: Effects of magnetization on domain structure of a cubic material [Cullity72].	25
Figure 2-13: Limiting and minor magnetic hysteresis loop, where points (a) and (d) show the saturation magnetic flux density of the material, (b) and (e) show the remanent magnetic flux density, and (c) and (f) show the coercivity [NDT09].	26

Figure 2-14: Magnetization curves for a single crystal of Co along its hard and easy axis [Kaya28].	28
Figure 2-15: Electron orbital influence on the magnetostrictive effect; based on figure from [Cullity72].	30
Figure 2-16: Basic electroplating cell.	33
Figure 2-17: Activation polarization curves for both high and low overpotentials. Dotted lines show extrapolated Tafel slopes which intersect at the exchange current density value [Bradford01].	38
Figure 2-18: Effect of concentration overpotential on a cathode polarization curve. Influence of increasing temperature, concentration and agitation on the limiting current density [Bradford01].	40
Figure 2-19: Possible sites for ad-atom addition onto a metal surface; numbering in decreasing order of stability; based on figure from [Paunovic06].	42
Figure 2-20: Cathode potential polarization graphs for possible two cation systems [Raub67].	43
Figure 2-21: Possible waveform of pulsed electrodeposition [Ibl80].	45
Figure 2-22: Reactant concentration change near an electrode as a function of time [Ibl80].	46
Figure 2-23: Effects of diffusion layer thickness on preferential deposition [Ibl80].	48
Figure 2-24: Distortion of an applied waveform due to capacitance effects during electrodeposition [Puipe80]. Case (a) represents a negligible capacitance effect, case (b) represents a moderate effect, and cases (c) and (d) display severe capacitance effects.	49
Figure 2-25: Tertiary diagram showing the saturation flux densities of bulk, annealed CoFeNi alloys [Bozorth51]. Dotted lines separate the BCC, FCC and mixed phase regions [Cooper05]. Not shown is the HCP phase region.	51
Figure 2-26: Tertiary diagram showing the coercivities of bulk, annealed CoFeNi alloys [Bozorth51]. Dotted lines separate the BCC, FCC and mixed phase regions [Cooper05]. Not shown is the HCP phase region.	52

Figure 2-27: Iron-cobalt binary phase diagram [Baker92].....	53
Figure 2-28: $\alpha$ -Mn unit cell with equivalent lattice positions identified by colour [Crystal04].....	63
Figure 3-1: Photograph of polypropylene electroplating cell: (a) Labeled sections of cell showing: the cylindrical vessel (A), the sample holders (B), the spacers (C), the cathode (D), the anode (E), the sample clasps (F) and the tightening screws (G). (b) The assembled electroplating cell.....	66
Figure 3-2: Schematic representation of the electroplating circuit. ....	68
Figure 3-3: Schematic representation of the tube section of the tube furnace: a) side view, (b) top view, (c) view along centre axis. Labels in the figure represent: the quartz tube (A), the fluted outlet (B), the top center opening (C), and the top center opening lid (D). ....	70
Figure 3-4: Schematic representation of quartz heating platform: a) side view of sample platform, (b) top view of sample platform, (c) magnified view along the stem towards the sample platform, (d) magnified view of sample platform. Labels in the figure represent: the heating platform stem (A), the sample platform (B), heating wire rings (C), and heating wire ridges (D). ....	71
Figure 3-5: Schematic representation of copper sample holder: a) top view and, (b) side view. Labels in the figure represent: the sample (A), aluminum nitride wafers (B), the copper plate (C), brass tightening screw (D), and the hole for the thermocouple (E). ....	72
Figure 4-1: Standard iron-cobalt plating solutions, which were exposed to air, in both fresh and aged forms: (a) fresh solution, (b) aged 14 days and (c) aged for more than one year.....	78
Figure 4-2: UV-visible absorption spectra of iron-cobalt plating solution prepared with dibasic ammonium citrate: fresh solution and aged.....	79
Figure 4-3: UV-visible absorption spectra of solution containing only cobalt cations: fresh solution and aged for 9 days.....	80
Figure 4-4: UV-visible absorption spectra of solution containing only iron cations: fresh solution and aged for up to 9 days.....	81

Figure 4-5: UV-visible absorption spectra of iron-cobalt solution sealed from atmosphere and aged for up to 29 days. ....	82
Figure 4-6: UV-visible absorption spectra of iron(III)-cobalt solution at various pH values compared with the spectrum of a heavily oxidized iron(II)-cobalt solution (aged for >1 year).....	83
Figure 4-7: The pH change in iron-cobalt plating solutions over time. ....	84
Figure 4-8: Regions of an XPS spectrum obtained from an iron-cobalt solution precipitate which show: a) iron (2p <sub>3/2</sub> and 2p <sub>1/2</sub> ) peaks and b) oxygen (1s) peaks. ....	86
Figure 4-9: UV-visible absorption spectra of fresh electroplating solutions after heating and/or usage to deposit iron-cobalt thin-films. ....	87
Figure 4-10: SEM SE micrographs of iron-cobalt deposit surfaces when plated using the standard solution (Table 3-1) and conditions (15mA/cm <sup>2</sup> for 9 minutes) at various temperatures.....	92
Figure 4-11: X-ray diffraction pattern for iron-cobalt thin films deposited using the standard plating solution and standard conditions at various temperatures: a) 20°C, b) 30°C, c) 40°C, d) 50°C, e) 60°C. ....	94
Figure 4-12: X-ray diffraction pattern of iron-cobalt film plated at 60°C using the standard plating solution and conditions, which shows additional peaks not observable in Figure 4-11. ....	95
Figure 4-13: XRD patterns from iron-cobalt deposits obtained using an unstabilized plating solution under standard plating conditions at various temperatures: a) 20°C, (b) 40°C and (c) 60°C. ....	97
Figure 4-14: XRD patterns of iron-cobalt deposits plated from the standard dibasic ammonium citrate plating solution under standard plating conditions with the pH adjusted to 2.3: a) 20°C, b) 40°C, c) 60°C. ....	100
Figure 4-15: XRD patterns of iron-cobalt deposits plated from the standard plating solution without dibasic ammonium citrate under standard plating conditions with the pH adjusted to 2.3: a) 20°C, b) 60°C. ....	100
Figure 4-16: XRD patterns showing the effects of current density on phase deposition using the standard plating solution and plating for 9	

minutes at various temperatures: a) 20°C, (b) 40°C and (c) 60°C. ....	104
Figure 4-17: TEM micrographs and electron diffraction patterns from the cross-section of a deposit plated at 20°C: (a) bright field image, (b-c) dark field images from adjacent to the seed layer and the bulk deposit, respectively and (d-e) electron diffraction patterns from adjacent to the seed layer and the bulk deposit, respectively. Dark field images were taken using the portions of the electron diffraction rings denoted with red circles. ....	106
Figure 4-18: TEM micrographs and electron diffraction patterns from the cross-section of a deposit plated at 40°C: (a) bright field image, (b-c) dark field images from adjacent to the seed layer and the bulk deposit, respectively and (d-e) electron diffraction patterns from adjacent to the seed layer and the bulk deposit respectively. Dark field images were taken using the electron diffraction areas denoted with red circles. ....	108
Figure 4-19: TEM micrographs and electron diffraction patterns from the cross-section of a deposit plated at 60°C: (a) bright field image, (b) dark field image and (c-d) electron diffraction patterns from adjacent to the seed layer and the bulk deposit respectively. The dark field image was taken using the electron diffraction area denoted with the red circle. ....	110
Figure 4-20: Optical micrographs of the surfaces of iron-cobalt deposits after annealing at various temperatures. ....	112
Figure 4-21: SEM BSE cross-sectional micrographs of iron-cobalt thin films deposited at 40°C and annealed at: (a) 174°C, (b) 225°C and (c-d) 390°C. ....	114
Figure 4-22: XRD patterns for iron-cobalt deposits plated at 20°C using the standard iron-cobalt plating solution and parameters: a) as deposited, (b) annealed at 174 °C, (c) annealed at 225 °C and (d) annealed at 390 °C. ....	115
Figure 4-23: XRD patterns for iron-cobalt deposits plated at 40°C using the standard iron-cobalt plating solution and parameters: a) as deposited, (b) annealed at 174°C, (c) annealed at 225°C and (d) annealed at 390°C. ....	116
Figure 4-24: XRD patterns for iron-cobalt deposits plated at 60°C using the standard iron-cobalt plating solution and parameters: a) as	



deposited, (b) annealed at 174°C, (c) annealed at 225°C and (d) annealed at 390°C. ....	117
Figure 4-25: XRD patterns for iron-cobalt deposits plated at 20°C using the standard iron-cobalt plating solution and parameters, and annealed under various magnetic fields at: a) 174°C, (b) 225°C and (d) 390°C. ....	118
Figure 4-26: XRD patterns for iron-cobalt deposits plated at 40°C using the standard iron-cobalt plating solution and parameters, and annealed under various magnetic fields at: a) 174°C, (b) 225°C and (d) 390°C. ....	119
Figure 4-27: XRD patterns for iron-cobalt deposits plated at 60°C using the standard iron-cobalt plating solution and parameters, and annealed under various magnetic fields at: a) 174°C, (b) 225°C and (d) 390°C. ....	119
Figure 4-28: TEM micrographs and electron diffraction patterns from the cross-section of a deposit plated at 20°C and annealed at ~174°C: (a) bright field image, (b) dark field image and (c) electron diffraction pattern from the bulk of the deposit. The dark field image was taken from the region marked with a red box using the portion of electron diffraction ring denoted with the red circle. ....	121
Figure 4-29: TEM micrographs and electron diffraction patterns from the cross-section of a deposit plated at 20°C and annealed at ~390°C: (a) bright field image, (b) dark field image and (c-d) electron diffraction patterns from the bulk deposit and the gold seed layer, respectively. The dark field image was taken using the portion of the electron diffraction ring denoted with the red circle. ....	123
Figure 4-30: TEM micrographs and electron diffraction patterns from two grains formed in the reacted region of the silicon substrate after annealing at ~390°C: (a) bright field image showing several grains (bright contrast) in the reacted region, (b) bright field image showing a dark grain in the reacted region, (c) electron diffraction pattern from the light grain at the centre of (a) identified as (Co,Fe)TiSi and (d) electron diffraction pattern from the dark grain at the centre of (b) identified as gold. ....	124
Figure 4-31: TEM micrographs and electron diffraction patterns from the cross-section of a deposit plated at 60°C and annealed at ~174°C: (a) bright field image, (b-c) dark field images near the	

seed layer and the deposit surface, respectively and (d-e) electron diffraction patterns from near the seed layer and the bulk deposit, respectively. The dark field images were taken using the portions of the electron diffraction rings denoted with red circles.....	126
Figure 4-32: TEM micrographs and electron diffraction patterns from the cross-section of a deposit plated at 60°C and annealed at ~390°C: (a) bright field image, (b) dark field and (c) electron diffraction patterns from the bulk deposit. The dark field image was taken using the portion of the electron diffraction ring denoted with the red circle.....	128
Figure 4-33: Saturation magnetic flux densities for iron-cobalt deposits plated at various temperatures, using the standard plating solution and parameters, after being annealed at various temperatures in the absence of an external magnetic field.....	132
Figure 4-34: Magnetic saturation flux densities for iron-cobalt deposits plated at various temperatures, using the standard plating solution and parameters, after being annealed at various temperatures in a 500 Oe external magnetic field.....	133
Figure 4-35: Magnetic saturation flux densities for iron-cobalt deposits plated at various temperatures, using the standard plating solution and parameters, after being annealed at various temperatures in a 2500 Oe external magnetic field.....	134
Figure 4-36: Coercivities for iron-cobalt deposits plated at various temperatures, using the standard plating solution and parameters, after being annealed at various temperatures in the absence of an external magnetic field.....	136
Figure 4-37: Coercivities of iron-cobalt deposits plated at various temperatures, using the standard plating solution and parameters, after being annealed at various temperatures in a 500 Oe external magnetic field.....	138
Figure 4-38: Coercivities of iron-cobalt deposits plated at various temperatures, using the standard plating solution and parameters, after being annealed at various temperatures in a 2500 Oe external magnetic field.....	138

## Abbreviations

<b>AFC</b>	Antiferromagnetically Coupled
<b>BCC</b>	Body Centred Cubic
<b>BF</b>	Bright Field
<b>BSE</b>	Back Scattered Electrons
<b>cgs</b>	Centimeter-Gram-Second
<b>EDX</b>	Energy Dispersive X-ray spectroscopy
<b>DC</b>	Direct Current
<b>DF</b>	Dark Field
<b>FCC</b>	Face Centred Cubic
<b>GMR</b>	Giant Magnetoresistive
<b>HCP</b>	Hexagonal Close-Packed
<b>HDD</b>	Hard Disk Drive
<b>MR</b>	Magnetoresistive
<b>SBA</b>	Sulphur-Bearing Additive
<b>SE</b>	Secondary Electrons
<b>SEM</b>	Scanning Electron Microscopy
<b>SI</b>	Système International
<b>SQUID</b>	Super Quantum Interference Device
<b>TEM</b>	Transmission Electron Microscopy
<b>TMAB</b>	Trimethylamineborane
<b>WDS</b>	Wavelength Dispersive Spectroscopy
<b>XPS</b>	X-ray Photoelectron Spectroscopy
<b>XRD</b>	X-Ray Diffraction

## Symbols

A	area
A	molar mass of metal
a	areal storage density
B	magnetic flux density
B <sub>S</sub>	saturation magnetic flux density
b	Tafel slope
C	Curie constant
D	grain diameter
d	thickness of media
E	electrode potential
E <sup>0</sup>	standard electrode potential
E <sub>eq</sub>	equilibrium electrode potential
E <sub>i</sub>	applied electrode potential
E <sub>C</sub>	crystal anisotropic energy
F	Faraday constant
G	Gibbs free energy
G <sup>0</sup>	standard Gibbs free energy
H	applied magnetic field strength
H <sub>C</sub>	coercivity
I	electrical current
<i>i</i>	electrical current density
<i>i</i> <sub>0</sub>	exchange current density
<i>i</i> <sub>m</sub>	average current density
<i>i</i> <sub>P</sub>	pulse current density
K <sub>N</sub>	anisotropy constant
M	magnetization (volume)
M <sub>r</sub>	remanent magnetization
M <sub>S</sub>	saturation magnetization

$m$	magnetic moment
$N_D$	number of anti-parallel domains
$n$	number of electrons
$R$	ideal gas constant
$R$	resistance
$T$	temperature
$T$	on-time
$T'$	off-time
$T_C$	Curie temperature
$t$	time
$V$	volume
$V$	voltage
$w$	mass
$x$	deposit thickness
$\eta$	overpotential
$\eta_A$	activation overpotential
$\eta_C$	concentration overpotential
$\eta_R$	resistance overpotential
$\Theta$	material constant
$\theta$	pulse plating cycle time
$\lambda$	magnetostriction
$\mu$	permeability
$\mu_0$	permeability of a vacuum
$\mu_r$	relative permeability
$\rho$	density
$\sigma$	specific magnetization (mass)
$\sigma_0$	specific magnetization at 0K
$\sigma_S$	saturation specific magnetization
$\Phi$	cathode current efficiency
$\Phi$	number of magnetic field lines
$\chi$	susceptibility

## Chapter 1 Introduction

Hard-disk drives (HDDs) are the major means of non-volatile data storage in most electronic devices. HDDs operate by imprinting bits of data onto rapidly spinning platter material using a strong magnetic field originating at the HDD write-head. To properly fulfill its role, the HDD write-head must possess a soft magnetic core material that is capable of producing strong magnetic fields, while retaining the ability to switch the direction of magnetization quickly and easily. Magnetic write heads thus require a core material with: a high saturation flux density, low coercivity, near zero magnetostriction, high permeability, and be capable of being electroplated as a uniform and cohesive thin film, which is currently the standard method of HDD manufacturing [Cooper05]. Traditionally these demands were met by iron-nickel alloys; originally by Permalloy ( $\text{Ni}_{80}\text{Fe}_{20}$ ) and later by the more iron-rich  $\text{Fe}_{55}\text{Ni}_{45}$  [Cooper05]. The demand for ever increasing data storage densities, however, necessitates that HDDs be capable of writing at higher frequencies on increasingly coercive platter materials. These requirements will soon exceed the capabilities of traditionally used iron-nickel based write-heads [Andricacos98].

An attractive alternative to the iron-nickel alloys currently used, and one that has been extensively researched, are iron-cobalt alloys. These alloys have been shown to be capable of attaining high saturation flux densities ( $\sim 2.4\text{T}$ ), low coercivities, and can be easily deposited through electrodeposition [Bozorth51, Liao87, Osaka03]. Iron-cobalt alloys typically suffer from higher coercivities than iron-nickel alloys, but through careful control of the compositional and morphological characteristics of the deposits, it has been shown that the coercivity can be reduced. Numerous studies have demonstrated that the best combination of magnetic properties for iron-cobalt thin film deposits require the formation of nano-sized grains. This has previously been accomplished through the codeposition of BCC and FCC phases, which limits grain size due to competitive growth.

Iron-cobalt plating solutions often have long term stability problems due to their tendency to form iron hydroxide precipitates. The stability of the solutions can be improved by lowering the pH of the solution (typically to 2.0-3.0) to reduce the concentration of hydroxyl ions. Lowering the pH of these solutions, however, has the undesirable effect of producing voids in the deposits as a consequence of hydrogen evolution at the cathode during electroplating. As an alternative, stabilizing agents, such as ammonium citrate, have been explored as a means to extend the useful lives of plating solutions without the necessity of reducing the pH of the solutions [Zhang04, Zhang07].

This thesis concerns an analysis of the stability of a dibasic ammonium citrate iron-cobalt plating solution at its natural pH and the characterization of iron-cobalt deposits obtained through its use. The deposits are characterized in terms of their morphological, compositional and magnetic properties. The effects of plating parameters such as plating temperature, current density and pH are analysed and the suitability of the deposits as potential write head materials is evaluated. This thesis is divided into 5 chapters.

Chapter 2 is a comprehensive literature survey, which explains the fundamental concepts associated with HDDs, magnetism, electrodeposition and the electrodeposition of soft-magnetic alloys. The first section of the chapter concerns HDDs (Section 2.1) and outlines their operation, the requirements of their write-heads and the method by which they are manufactured. The magnetism section (Section 2.2) explains the basic concepts associated with classical magnetism and provides the background necessary to understand the magnetic concept that will be referred to in later chapters. The fundamental electrochemical concepts of electrodeposition are explained in Section 2.3. The final section pertains to the electrodeposition of soft magnetic alloys and in particular the electrodeposition of iron-cobalt alloys. This section contains an extensive literature survey containing the works of many research groups which have worked in this area.

The experimental procedure, equipment and methods of analysis are described in Chapter 3. This chapter contains the experimental parameters which

were used to obtain the results described in the following chapter.

Chapter 4 reveals, analyses and discusses the experimental results. This chapter is separated into 4 main sections. The solution stability section (Section 4.1) deals with the stability of the dibasic ammonium citrate stabilized iron-cobalt plating solution. This section evaluates the long term stability of the plating solution and outlines the parameters that affect the stability of the solution. The characterization of the as-plated iron-cobalt deposits is discussed in Section 4.2. This section characterizes the deposits in terms of composition, morphology, and phase composition. Particular attention is paid to the influence of plating temperature and plating current on the deposits. Characterization of deposits which have been annealed at various temperatures and under the influence of external magnetic fields is covered in Section 4.3.2. Finally, the magnetic properties in terms of the saturation flux density and coercivity of as-plated and annealed iron-cobalt deposits are analysed in Section 4.4.

In the final chapter of this thesis, the results are summarized, the main conclusions are outlined and recommendations for future work are made.

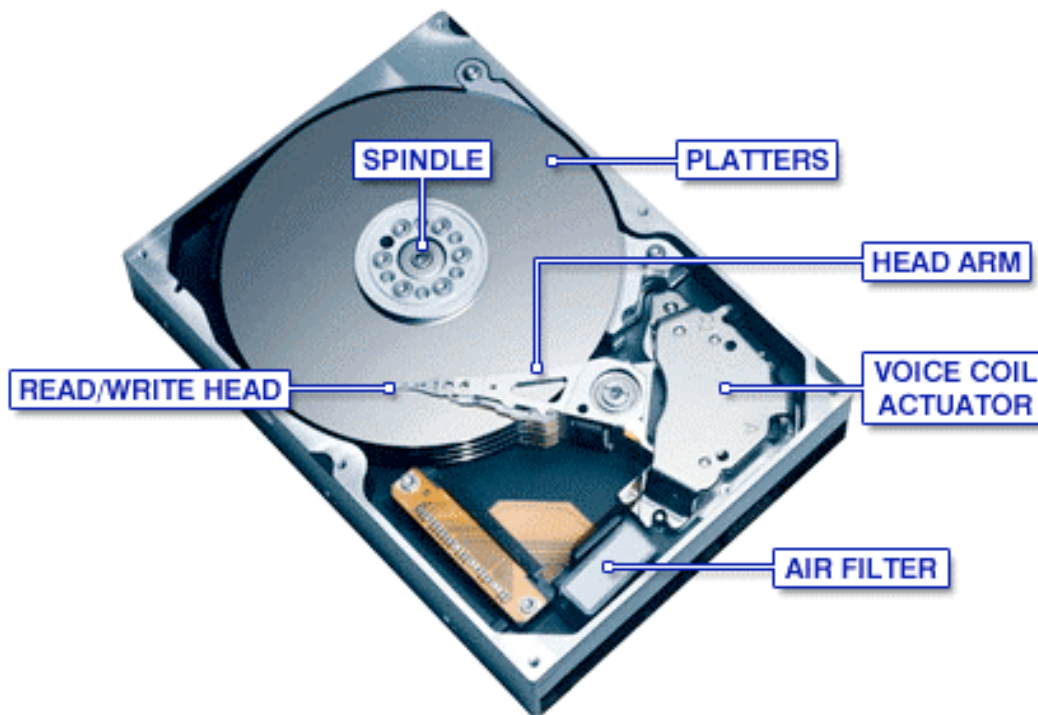


## Chapter 2 Background

### 2.1 Background

#### 2.1.1 Hard Disk Drives

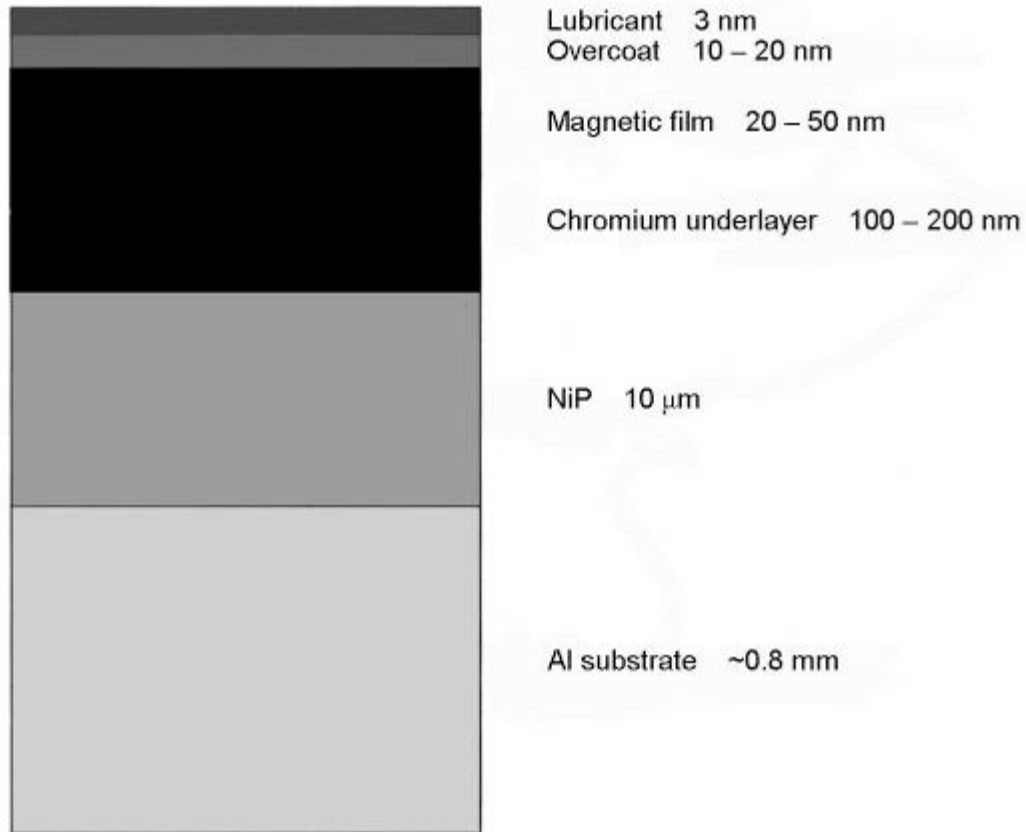
Hard-disk drives (HDDs) operate as the means of non-volatile data storage in most electronic devices. A typical HDD with its casing removed is depicted in Figure 2-1.



**Figure 2-1:** Hard disk drive with structures labeled [BBC07].

Data is stored in HDDs as small, magnetized regions on the surface of a rapidly spinning platter. Platters are typically made of a non-magnetic substrate upon which a thin layer of hard ferromagnetic material is deposited. It is this thin surface layer in which data is imprinted. Additional layers are also deposited for

leveling and protective purposes. Figure 2-2 shows the cross-section of a typical HDD platter.

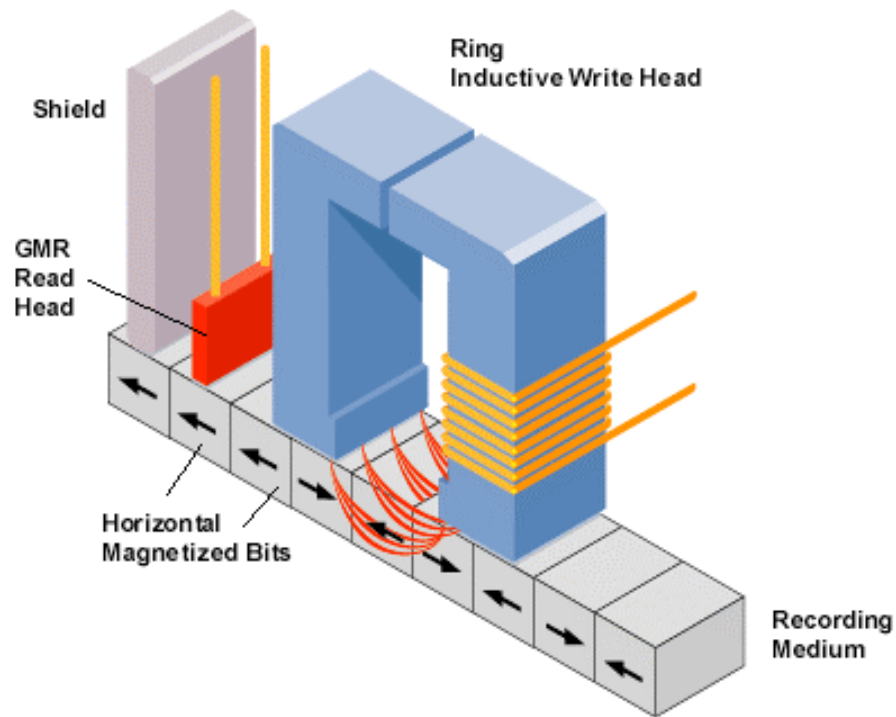


**Figure 2-2:** Schematic cross-section of a thin-film hard disk platter [Wang99].

Data is imprinted onto and read from the platter using read and write heads which are suspended over the platter via the actuator arm. The arm pivots on its axis in order to access different areas of the platter. Movement of the actuator arm is controlled via a voice coil actuator, or by a stepper motor in older HDDs.

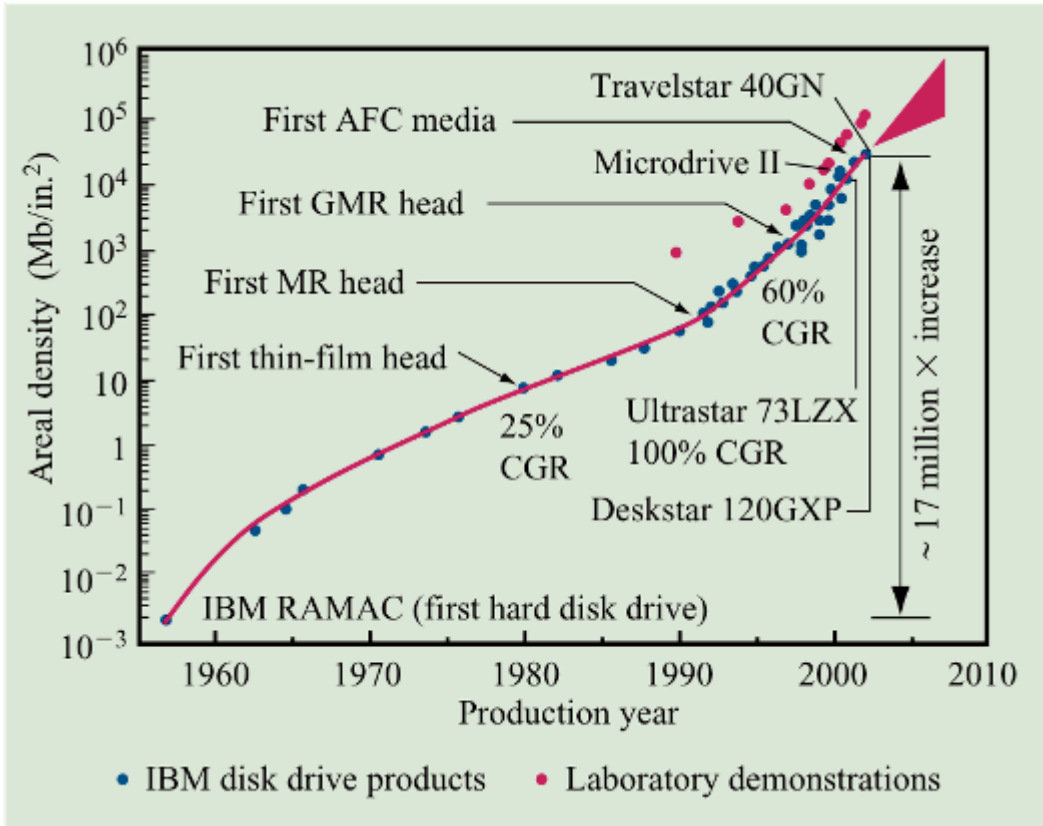
At the write head, a strong magnetic field is induced in the write head's magnetically soft core-material by passing an electrical current through a solenoid. The current passing through the solenoid produces a weak magnetic field, which is able to induce a much stronger field in the core material. As the write head passes over the rapidly spinning platter, it magnetizes small areas of its

surface in alternating directions, Figure 2-3. These regions act as bits and are equivalent to the “0”s and “1”s used in the binary encoding of digital information. The read head can later detect the pattern of magnetization in order to retrieve the corresponding information.



**Figure 2-3:** Longitudinal magnetization of recording medium by a write head [Computer06].

The amount of data that can be stored on a platter is measured in terms of its areal density. In the past, it has been the desire to improve the areal density of HDDs that has acted as the driving force for HDD technological innovation and development, and this trend continues to the present day. Figure 2-4 shows the past trend for improvements in HDD areal density as a function of time, starting with the incorporation of magnetic disk drives, in the form of the IBM 350, into commercial computers in 1956.



**Figure 2-4:** Evolution of areal density in hard disk drives [Cooper05].

From Figure 2-4, it can be seen that in the years following its introduction there was a steady improvement in HDD areal density of  $\sim 39\%$  annually up until the year 1991 [Daniel98]. In the year 1991, the slope of the graph increases sharply. This is due in large part to the development and introduction of the first magnetoresistive (MR) read heads [Thompson00]. Prior to 1991, inductive write heads filled both the reading and writing functions. To adequately fill the reading function, inductive read/write heads required much better magnetic anisotropy, much smaller coercivities, low internal stress, and very low magnetostriction [Cooper05]. In order to fulfill this role, properties beneficial to write-head functioning, such as high saturation magnetization, were compromised. The development of more sensitive MR read-heads allowed for the physical separation of the read and write head components and liberated the write head for optimization. As a result, the areal densities of HDDs have increased steadily by

~60% annually since 1991 [Thompson00]. This trend has been maintained through the development of giant magnetoresistive (GMR) read heads and, more recently, the use of antiferromagnetically coupled (AFC) substrates and perpendicular recording.

Areal density is the combination of the track density, how close the bits can be placed along the platter in the radial direction, and linear density, how close bits can be placed one after the other [Andricacos98]. Smaller bits are, therefore, favorable in terms of areal density. The lower limit of bit size is, however, limited because small bits are prone to demagnetization through thermal disordering; the point at which the bits are no longer thermally stable is called the superparamagnetic limit [Cooper05]. The limiting areal storage density of a platter material can be described in terms of the smallest sustainable bit length ( $a$ ) expressed by the equation:

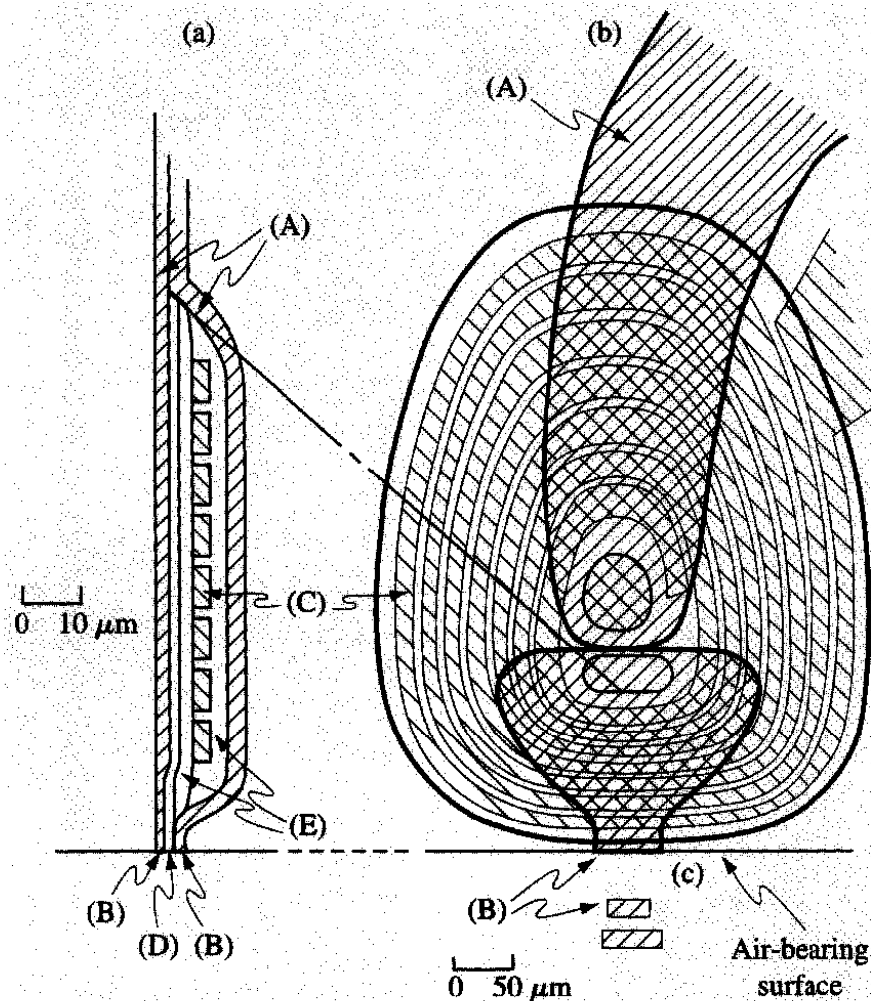
$$a = \frac{M_r d}{2\pi H_C} \quad (2.1.1)$$

where  $M_r$  is the magnetization of the media,  $d$  is the thickness of the media, and  $H_C$  is the coercivity of the media [Andricacos98]. Using SI units, the bit size has the units of m/bit. From Eqn. 2.1.1, it is apparent that the lower limitations of areal storage density can be decreased by using more coercive (magnetically harder) platter materials. There is, therefore, incentive for industry to use magnetically harder materials in the manufacturing of HDDs. As higher saturation flux densities are necessary to imprint on high coercivity materials, additional stress is put on write head performance. One key way in which this can be accommodated is through the use of core materials capable of attaining higher saturation flux densities.

### **2.1.2 Thin film write-heads**

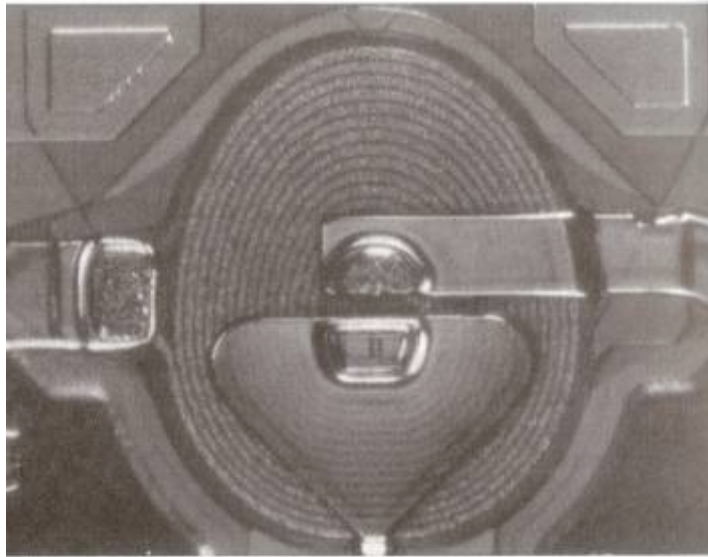
Thin-film read/write heads were first introduced by IBM in 1979 and represented a major improvement in inductive read/write head design [Daniel98].

Thin-film write heads allowed engineers greater precision in the formation of head and spacing dimensions and allowed for high frequency performance which was needed as data rates increased [Daniel98]. The basic design of inductive write-heads is shown in Figure 2-5 and Figure 2-6. Inductive write heads consist of an electroplated copper coil (C) surrounded on both sides by soft magnetic films (A). The copper coil is insulated from the magnetic films by insulating layers (E). During operation, current is passed through the copper coil, which induces a magnetic field in the soft magnetic films. This results in the formation of a magnetic field at the write-head pole tips (B), which are separated by a gap layer (D).



**Figure 2-5:** Schematics of IBM 3370 read/write-head: a) cross-sectional schematic showing the magnetic layers (A), pole tips (B), copper coil (C), gap layer (D), and electrical insulation layers (E); b) planar view of

read/write-head; c) pole tips at air-bearing surface [Chiu96].



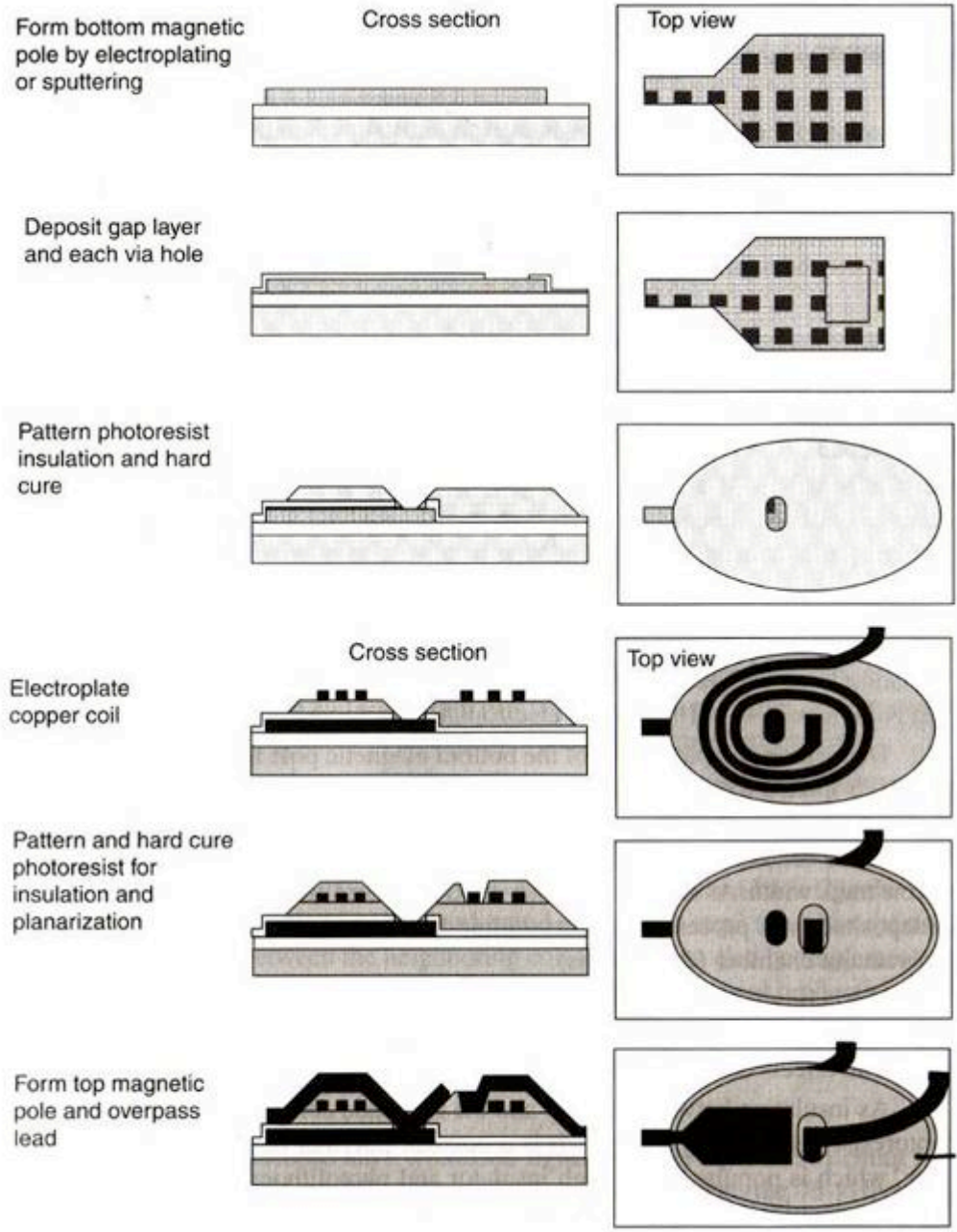
**Figure 2-6:** Inductive write head [Daniel98].

Thin-film HDD write-heads are fabricated using a multi-step combination of thin-film deposition techniques [Paunovic06]. The production steps described are depicted in Figure 2-7 and Figure 2-8.

1. Initially a substrate, typically a wafer composed of aluminum titanium carbide (ALTiC), is sputter coated with  $\sim 15\mu\text{m}$  thick layer of alumina. The alumina layer acts as an insulating layer between the substrate and the magnetic pole material. Following this, the pole material ( $2\text{-}4\mu\text{m}$ ) is electrodeposited through a mask to form the bottom soft magnetic pole.
2. An alumina gap layer ( $0.1\text{-}0.5\mu\text{m}$ ) is sputter deposited over the bottom magnetic pole.
3. Electrically insulating photoresist ( $\sim 5\mu\text{m}$ ) is patterned over the alumina layer.
4. A spiral copper coil ( $\sim 3\mu\text{m}$  thick,  $3\text{-}4\mu\text{m}$  wide, and  $2\mu\text{m}$  between each coil) is electroplated over the photoresist surface. To allow for the electrodeposition over the non-conductive photoresist, a thin conductive seed layer is initially sputtered over its surface and then selectively etched away after the coil has been formed.

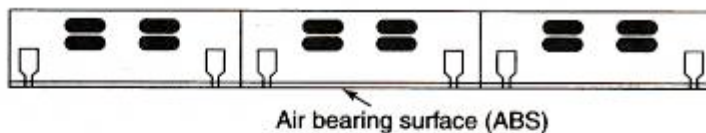
5. A second layer of insulating photoresist is deposited over the copper coil. It is then annealed at a temperature above the softening point in order to smooth its surface in preparation for the deposition of the upper pole tip.
6. The upper pole and overpass lead are electroplated onto the write head. The overpass lead acts as the path for current to reach the copper coil.
7. The wafer is then scribed and sliced into row bars.
8. The row bars of write heads are lapped and etched to expose the air bearing surface. The wafer is then further diced to free the individual write heads.
9. The write heads are tested and bonded to a slider for integration onto the HDD arm assembly.



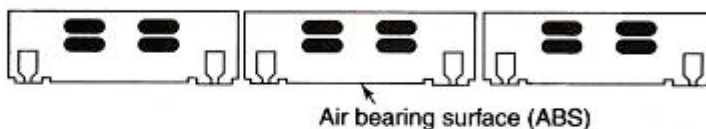


**Figure 2-7:** Thin-film fabrication of write heads; corresponds to steps 1-6 in the text [Mallinson97].

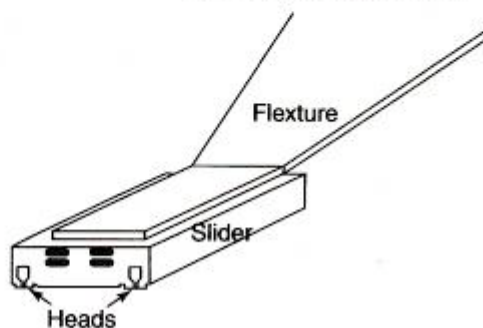
Slice head wafers into row bars



Lap and etch air bearing surface, dice row bar into sliders



Bond slider to flexure, head gimbel assembly is ready to be shipped



**Figure 2-8:** Final dicing and mounting of write heads; corresponds to steps 7-9 in the text [Mallinson97].

## 2.2 Magnetism

### 2.2.1 Magnetic Properties and Units

Unlike many other scientific fields, adoption of S.I. (Système International) units has been relatively slow in regards to quantifying magnetic properties. As a result, literature on the subject often still uses the traditional cgs (centimeter-gram-second) system of units, or to add to the confusion, a combination of cgs and S.I. units. This section will explain some fundamental magnetic properties which will be used. Units of measurement from both the cgs and S.I. systems are summarized in Table 2-1.

**Table 2-1:** Units of magnetic properties in cgs and S.I. systems

	Symbol	CGS units	Conversion to S.I.	S.I. units
Magnetic Moment	m	Emu	$10^{-3}$	A·m <sup>2</sup>
Magnetization (volume)	M	emu/cm <sup>3</sup>	$10^3$	A/m
Magnetization (mass)	$\sigma$	emu/g	1	A·m <sup>2</sup> /kg
Applied Field Strength	H	Oersted (Oe)	$10^3/4\pi$	A/m
Magnetic Flux Density	B	Gauss (G)	$10^{-4}$	Tesla (T)
Susceptibility	$\chi$	emu/(cm <sup>3</sup> ·Oe)	$4\pi$	Dimensionless
		dimensionless	1	
Permeability	$\mu$	dimensionless	$4\pi \cdot 10^{-7}$	H/m
Relative Permeability	$\mu_r$	not defined	-	Dimensionless
Permeability of a Vacuum	$\mu_0$	1	$4\pi \cdot 10^{-7}$	H/m

### Magnetic moment (m)

The magnetic moment is an expression of the torque experienced by a material when placed in a magnetic field. When a magnetic material is placed at some angle to a magnetic field it will experience a torque, which will attempt to align the material parallel to the direction of the magnetization. The magnetic moment is the moment exerted on the material when placed at a right angle to a uniform magnetic field [Cullity72].

### Intensity of magnetization (M, $\sigma$ )

The intensity of magnetization, or simply the magnetization, quantifies the magnetic moment experienced by a material as a function of the amount of material present. In most cases, magnetization is defined in terms of the volume (V) of the material:

$$M = m/V \quad (2.2.1)$$

In cases where it is more desirable to denote magnetization as a function of mass, the specific magnetization ( $\sigma$ ) is used. This is related to the volume magnetization (M) by:

$$\sigma = \frac{m}{w} = \frac{m}{V\rho} = \frac{M}{\rho} \quad (2.2.2)$$

where w is the mass and  $\rho$  is the density of the material [Cullity72].

### Applied field strength/Applied field intensity (H)

The applied field strength is a measurement of the intensity of an external/magnetizing field.

### Magnetic flux density (B)

Magnetic flux density describes the number of magnetic field lines that pass through an object ( $\Phi$ ) divided by its cross-sectional area (A) [Cullity72].

$$B = \Phi/A \quad (2.2.3)$$

The magnetic flux density of a material is thus the result of the combined actions

of the applied field and the field produced by the material itself, which can be expressed in the cgs system by:

$$B = H + 4\pi M \quad (2.2.4)$$

and using S.I. units by:

$$B = \mu_0(H + M) = \mu_0 H + \mu_0 M \quad (2.2.5)$$

where  $\mu_0$  is the magnetic permeability of a vacuum ( $4\pi \cdot 10^{-7}$  H/m).

Confusion often arises over the units use to express the magnetization (M), applied field strength (H) and flux density (B). Using the cgs unit system, H is measured in oersteds (Oe) which are equivalent to the units for B, gauss (G). The equivalency between oersteds and gauss results in the two units being used interchangeably in the literature. Conversely, magnetization, in cgs units, is expressed in terms of emu/cm<sup>3</sup> which necessitates that a factor of  $4\pi$  be included in the magnetization term of Eqn. (2.2.4). To eliminate the  $4\pi$  factor from Eqn. (2.2.4) it is not uncommon to see magnetization also expressed in terms of gauss or oersted.

Using the S.I. system, both H and M are both measured in terms of A/m, however, B is expressed in units of tesla (T). Because 1T is equivalent to 10,000G, it is often the unit of choice when high magnetic fields are involved and, although an S.I. unit, is often used along with cgs units. The permeability of a vacuum ( $\mu_0$ ) must also be included when S.I. units are used. Strictly speaking, the  $\mu_0$  term is also present when using cgs units, however, in the cgs system it has a value of unity and is dimensionless; it is therefore not expressed in Eqn. (2.2.4).

### Susceptibility ( $\chi$ )

Susceptibility describes the amount of magnetization produced in a material in relation to the strength of the magnetic field that produces it [Cullity72]. Susceptibility is expressed by:

$$\chi = \frac{M}{H} \quad (2.2.6)$$

Using the standard cgs units for M and H,  $\chi$  should have units of emu/(cm<sup>3</sup>•Oe), however, because M is often expressed in terms of either oersted or gauss, it is

also common for  $\chi$  to be expressed as a dimensionless number.

### Permeability ( $\mu$ )

Magnetic permeability describes the relationship between the magnetic flux density and the strength of the applied field [Cullity72]. Magnetic permeability can be expressed by:

$$\mu = \frac{B}{H} \quad (2.2.7)$$

Often, when using S.I. units, it is desirable to express permeability in relation to the permeability of a vacuum; in this case the relative susceptibility ( $\mu_r$ ) is used.

$$\mu_r = \frac{\mu}{\mu_0} \quad (2.2.8)$$




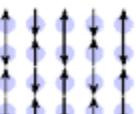
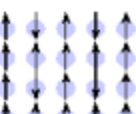
### **2.2.2 Types of Magnetism**

On the atomic level, magnetic forces arise due to the motion of the electrons associated with the atoms' various electron shells. Electrons have associated with them a magnetic moment that is produced due to both orbital motion and the spin of the electrons [Cullity72]. Depending on the electronic configuration of the element, the overall magnetic moment of the atom can be divided into two situations:

1. The magnetic moments of the electrons cancel each other out resulting in an atom with no net magnetic moment. These are known as diamagnetic species.
2. The magnetic moments of the electrons do not cancel each other out and the atom is left with an overall magnetic moment. These species can be paramagnetic, ferromagnetic, ferrimagnetic or antiferromagnetic, depending on the nature of their interaction with surrounding atoms.

A summary of these types of magnetism is shown in Table 2-2.

**Table 2-2:** A summary of different magnetic behaviours [Birmingham09].

Type of Magnetism	Susceptibility	Atomic / Magnetic Behaviour	Example / Susceptibility
Diamagnetism	Small & negative.	Atoms have no magnetic moment 	Au -2.74x10 <sup>-6</sup> Cu -0.77x10 <sup>-6</sup>
Paramagnetism	Small & positive.	Atoms have randomly oriented magnetic moments 	β-Sn 0.19x10 <sup>-6</sup> Pt 21.04x10 <sup>-6</sup> Mn 86.10x10 <sup>-6</sup>
Ferromagnetism	Large & positive, function of applied field, microstructure dependent.	Atoms have parallel aligned magnetic moments 	Fe ~100,000
Antiferromagnetism	Small & positive.	Atoms have anti-parallel aligned magnetic moments 	Cr 3.6x10 <sup>-6</sup>
Ferrimagnetism	Large & positive, function of applied field, microstructure dependent.	Atoms have mixed parallel and anti-parallel aligned magnetic moments 	Ba ferrite ~3

### 2.2.2.1 Diamagnetic materials

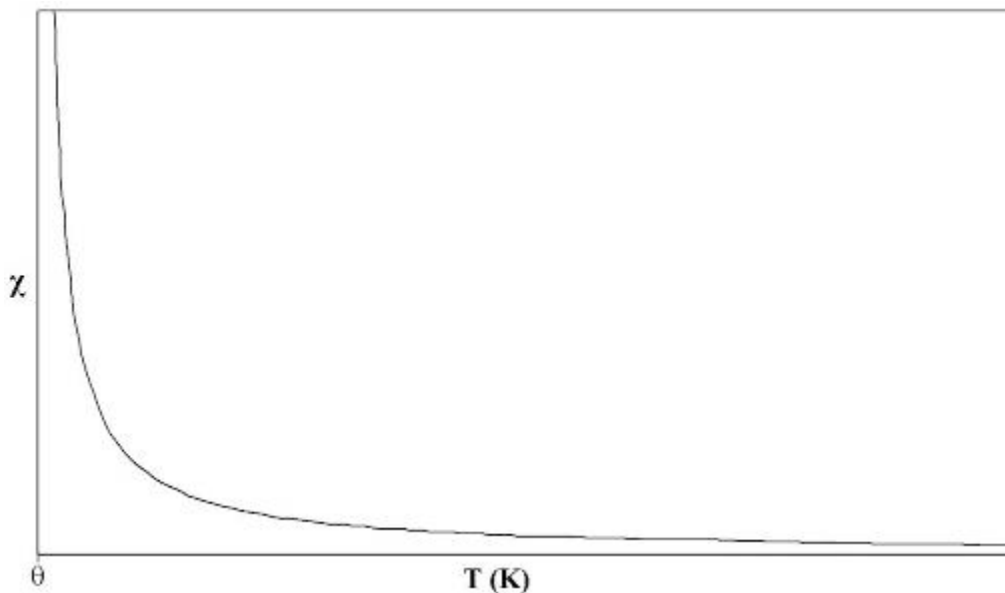
As stated above, diamagnetic materials result when the atoms which compose them have no net magnetic moment. These materials, when exposed to an external field produce a magnetization, which opposes that of the applied field in accordance with Lenz's Law [Cullity72]. Diamagnetic materials, thus, have negative susceptibilities which are unaffected by temperature changes. Although diamagnetic behaviour is present in all materials, its effects are typically insignificant when compared with the much stronger magnetic phenomena that arise when the atoms have a net magnetic moment associated with them.

### 2.2.2.2 Paramagnetic materials

Paramagnetic materials are composed of atoms which have net magnetic moments; however, these magnetic moments are randomly orientated with respect to each other, resulting in no net magnetization for the material as a whole [Cullity72]. Under the effects of a magnetic field, there is a tendency for the moments to align; this effect is opposed by the randomizing effects of thermal vibrations. As a result, paramagnetic materials show only small positive susceptibilities. As thermal vibrations hinder the magnetization of paramagnetic materials, temperature has a large influence on susceptibility; this relationship is shown in the Curie-Weiss Law:

$$\chi = \frac{C}{(T - \Theta)} \quad (2.2.9)$$

Susceptibility,  $\chi$ , is a function of: the Curie constant (C), temperature (T), and a material constant ( $\Theta$ ). In the case of a perfectly paramagnetic material, the material constant,  $\Theta$ , is equal to zero, Figure 2-9 shows the variation of susceptibility with temperature for paramagnetic materials according to the Curie-Weiss Law. Note that the Curie-Weiss Law becomes discontinuous when  $T = \Theta$ .



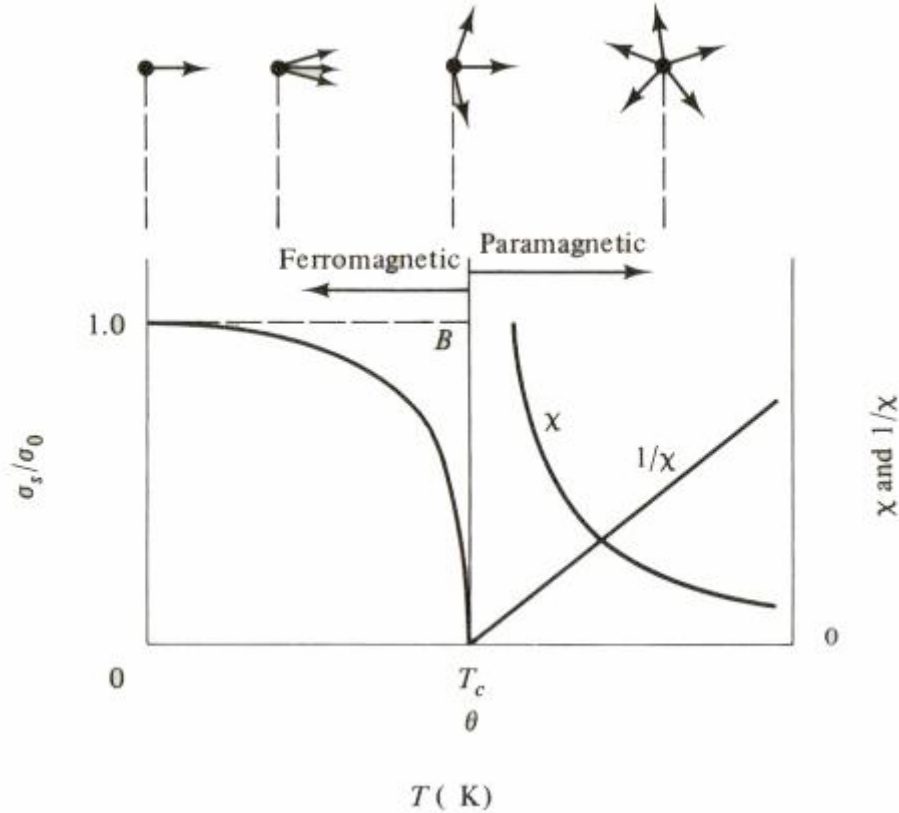
**Figure 2-9:** Variation of susceptibility with temperature for paramagnetic materials.



### 2.2.2.3 Ferromagnetic materials

Ferromagnetic materials, like paramagnetic materials, are composed of atoms with a net magnetic moment; however, these magnetic moments are strong enough to resist the randomizing effects of thermal vibrations. Through exchange interactions, they align themselves so that their magnetic moments lie parallel to those atoms which surround them [Cullity72]. Regions of atoms with uniformly aligned magnetic dipoles are known as domains. Only three pure elements are ferromagnetic at room temperature: iron, nickel and cobalt.

Under the influence of an external magnetic field the magnetic domains tend to shift in the direction of magnetization resulting in the overall magnetization of the material. Ferromagnetic materials have very large and positive susceptibilities. Thermal vibrations limit the ability of the domains to align perfectly and, therefore, susceptibility of ferromagnetic materials decreases with increasing temperature. The magnetic behaviour of a ferromagnetic material as a function of temperature is shown in Figure 2-10. The point at which thermal vibrations completely overcome the exchange interactions which align the atoms is known as the Curie temperature ( $T_C$ ). Above the Curie temperature ferromagnetic materials display properties similar to paramagnetic materials. The Curie-Weiss Law is applicable to ferromagnetic materials when above their Curie temperature; in this case the value of  $\Theta$  is equal to the Curie temperature of the material.



**Figure 2-10:** Magnetization and susceptibility curves below and above the Curie temperature [Cullity72]. Saturation magnetization ( $\sigma_s$ ) describes the maximum magnetization for a material at a particular temperature and  $\sigma_0$  is the magnetization at 0K.

Ferromagnetism and domain theory are discussed further in Section 2.2.3.

#### 2.2.2.4 Antiferromagnetic materials

Exchange interactions among the atoms of antiferromagnetic materials behave in such a way that they tend to align the magnetic moments of neighbouring atoms in a manner anti-parallel to each other [Cullity72]. Antiferromagnetic materials, therefore, in essence form two interwoven sub-lattices of atoms with opposite magnetic alignments. Since the two sub-lattices act in opposition to each other, there is no net magnetization of the material and it acts similar to a paramagnetic material. Antiferromagnetic materials display a transition to true paramagnetic behavior, i.e., random orientation of atomic

magnetic moments, when heated above their Neel's temperature. Antiferromagnetic materials obey the Curie-Weiss Law in their paramagnetic region; however,  $\Theta$  has a negative value which is not equivalent to the Neel's temperature. Chromium is the only element to display antiferromagnetic behaviour in its equilibrium form.

#### **2.2.2.5 Ferrimagnetic materials**

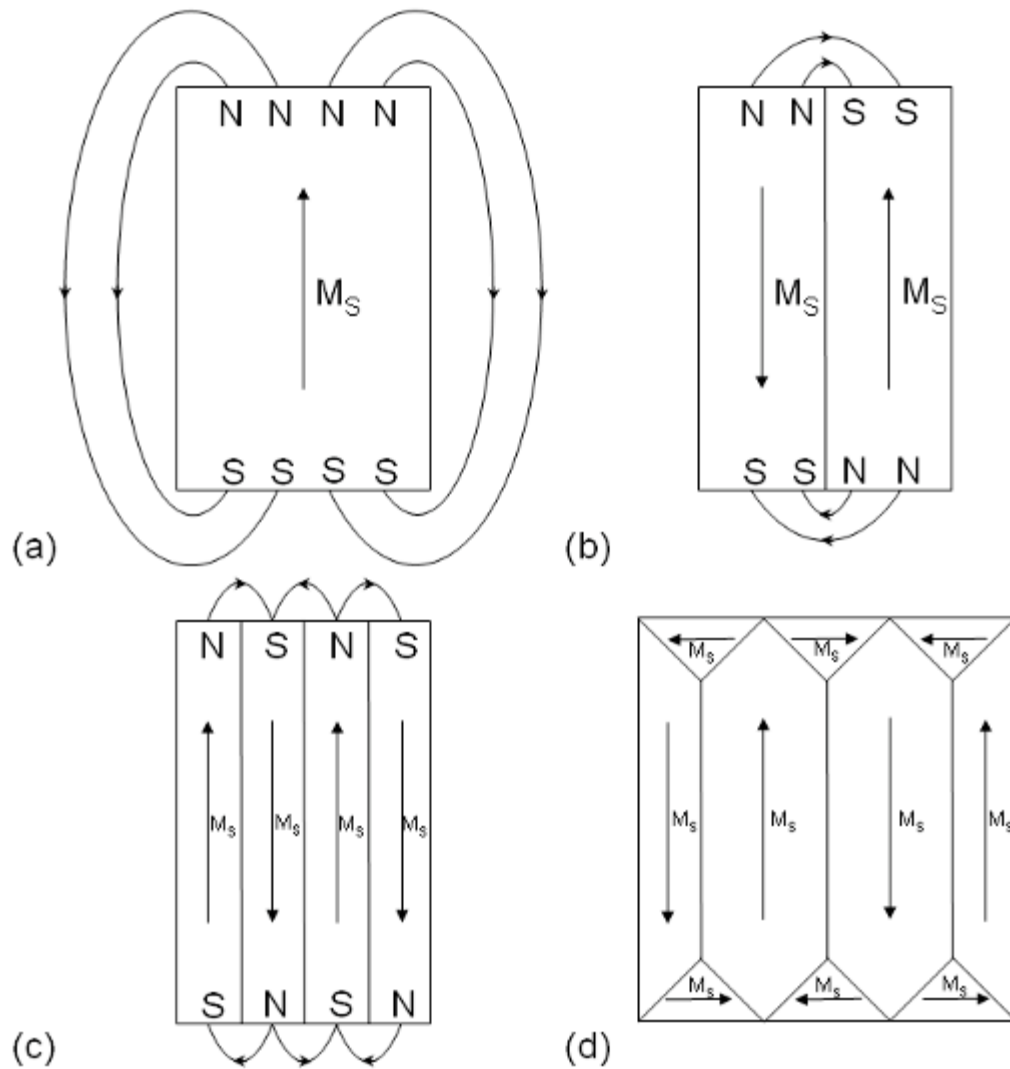
Ferrimagnetic materials are crystalline compounds that show many similar properties to ferromagnetic materials. Like ferromagnetic materials they can be magnetized at room temperature and are composed of magnetically saturated domains [Cullity72]. Where ferrimagnetic materials differ, however, is some species of atoms magnetically align anti-parallel to the dominant magnetically aligned species. The result is that a net magnetization can be produced in ferrimagnetic materials; however, since some of the atoms counteract the dominant direction of magnetization, the overall magnetization will be less than it would be for a ferromagnetic material.

### **2.2.3 Ferromagnetism**

#### **2.2.3.1 Domain Theory**

The concept of magnetic domains was first introduced by Pierre Weiss in 1906 to account for the very high susceptibilities of ferromagnetic materials as well as the characteristic shape of their magnetic hysteresis curves (see Section 2.2.3.3). Weiss postulated that, while above their Curie temperatures thermal vibrations cause ferromagnetic materials to behave paramagnetically, below the Curie temperature the dipoles of ferromagnetic atoms are strong enough to allow for extended regions where atoms will self-align with their neighbouring atoms. These regions are known as domains [Cullity72]. Because domains consist of regions where the atoms are perfectly aligned, these regions have the highest

possible magnetization for the material, or are magnetically saturated. Although ferromagnetic materials are composed of magnetically saturated domains, misalignment between these domains results in a lower magnetization for the overall material. To saturate the overall material, an external magnetic field is required to align the domains.



**Figure 2-11:** Possible domain structures for unmagnetized ferromagnetic crystals.

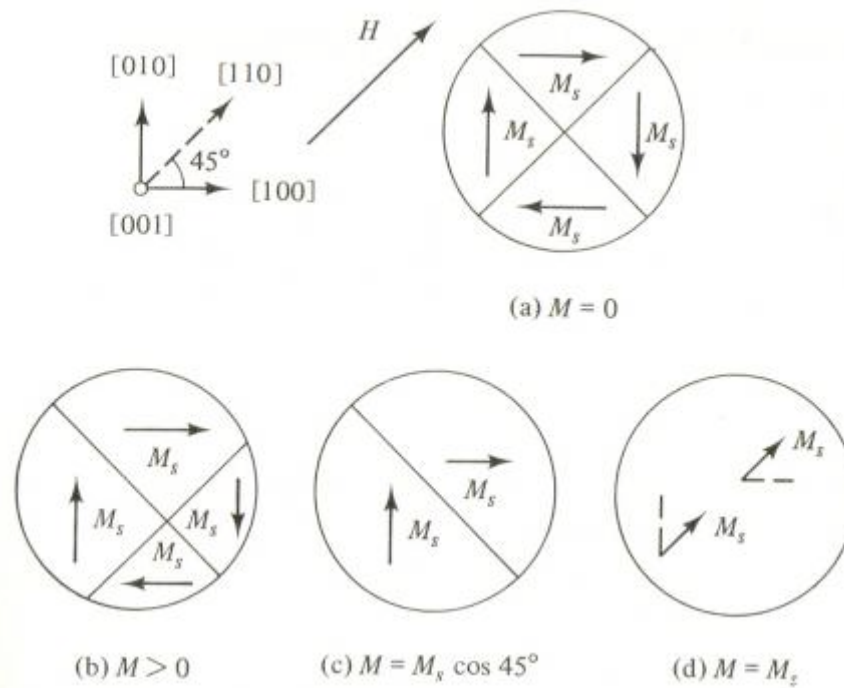
In the absence of a magnetic field, the domains are magnetized along their easy axes of magnetization (see Section 2.2.3.4) and arrange themselves in such a way as to minimize the magnetostatic energies. Magnetostatic energies arise due

to the formation of a demagnetizing field around uniformly magnetized regions [Cullity72]. For instance, Figure 2-11 (a) shows a single rectangular domain with uniaxial anisotropy. At either end of the domain are free poles which produce a magnetic field which, by convention, moves from the north to the south pole. The exterior magnetic field induces a magnetic field which acts in opposition to the interior magnetic field of the material. This self-demagnetizing effect produces magnetostatic energies which are energetically unfavourable [Craik65]. These energies can be reduced by limiting the strength of the external magnetic field, which can occur by decreasing the area of the free poles via the formation of a second domain which runs anti-parallel to the first, as shown in Figure 2-11 (b). The formation of this second domain reduces the electrostatic energy of the material by a factor of two, and the formation of successive anti-parallel domains will continue to reduce the magnetostatic energy to a value of  $1/N_D$ , where  $N_D$  is the number of anti-parallel domains [Cullity72]. Therefore the magnetostatic energy of the crystal in Figure 2-11 (c) is  $\frac{1}{4}$  of the magnetostatic energy of (a). Reduction in this way, however, cannot continue indefinitely as the formation of new domain walls in itself requires energy. At some point equilibrium is reached where the formation of new domains is no longer energetically favorable. Magnetostatic energies can be reduced further in crystals systems which have perpendicular easy axes of magnetization; e.g., cubic crystals, as this allows for the formation of “closure” domains at free surfaces (Figure 2-11 (d)). These closure domains eliminate external fields and so greatly reduce the magnetostatic energy [Craik65].

### 2.2.3.2 Magnetization

A ferromagnetic material in its demagnetized state is divided into domains which are orientated in such a way that there is no net magnetization (Figure 2-12 (a)). The process of magnetization is one by which a material is taken from a multi-domain state and placed into a single domain states in the direction of the applied magnetic field. Once a magnetic field is applied to the material there is a

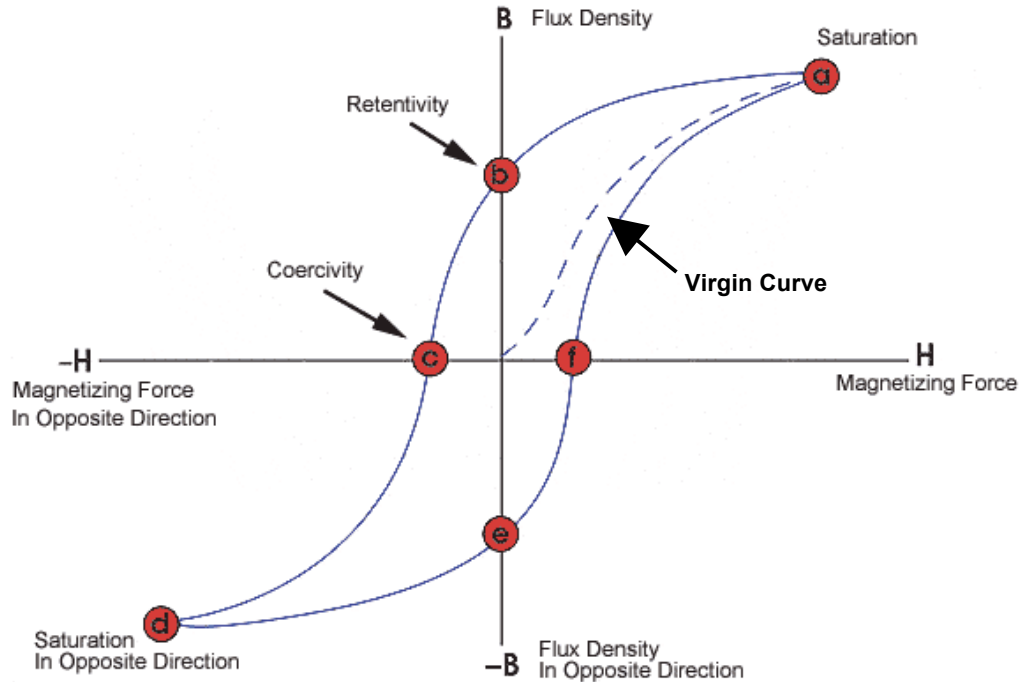
tendency for domains which are more closely oriented with the magnetic field to grow at the expense of other domains. This phenomenon persists until a state is reached where only the domains which lie closest to the applied field direction remain (Figure 2-12 (b-c)). In this state the domains are still oriented along their easy axis. To further magnetize the material the applied field must shift the direction of magnetization to a non-easy direction in order for saturation to occur (Figure 2-12 (d)).



**Figure 2-12:** Effects of magnetization on domain structure of a cubic material [Cullity72].

### 2.2.3.3 Magnetic Hysteresis

The limiting, or major, hysteresis loop depicts the magnetization behaviour of a material which is magnetized to saturation using an applied field ( $H$ ), first in one direction and then in the opposite direction. A typical limiting hysteresis loop is shown in Figure 2-13.



**Figure 2-13:** Limiting and minor magnetic hysteresis loop, where points (a) and (d) show the saturation magnetic flux density of the material, (b) and (e) show the remanent magnetic flux density, and (c) and (f) show the coercivity [NDT09].

From the limiting hysteresis loop several properties can be identified: the saturation magnetic flux density ( $B_S$ ), the remanent magnetic flux density ( $B_R$ ) and the coercivity ( $H_C$ ). Also shown is the so called “virgin curve” which indicates the magnetization behaviour of the material from its demagnetized state. If the material is placed in an alternating magnetizing field but does not reach saturation then a minor hysteresis loop is produced. Once magnetized, a demagnetized state may be obtained by annealing the material at a temperature above its Curie temperature and then quenching it in the absence of a magnetic field; or by the application of a cyclic magnetic field of gradually decreasing intensity.

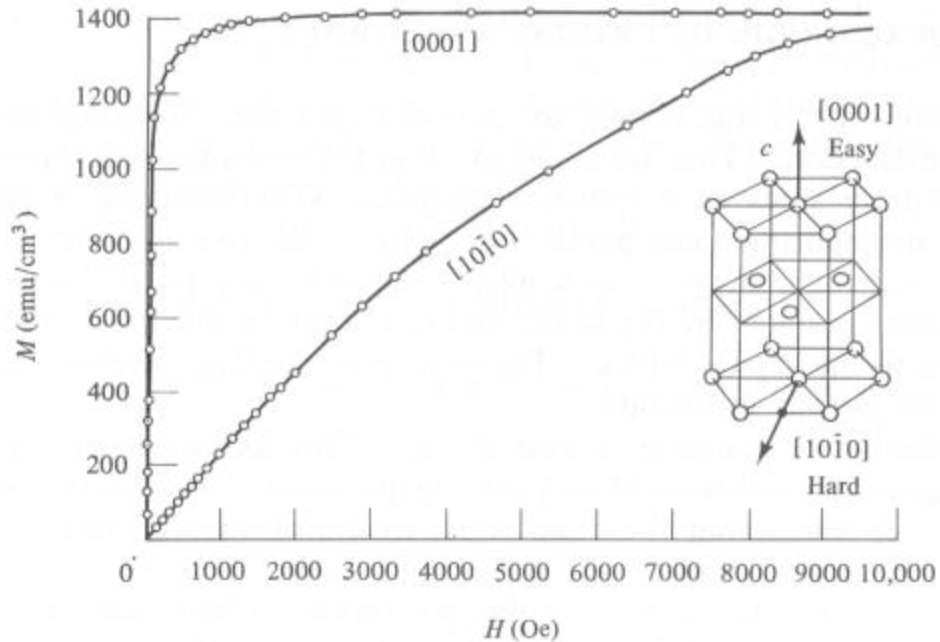
The saturation magnetization ( $B_S$ ) of a material is a function of: the strength of the dipoles of the atoms which compose the material, the density of the atomic packing of the material and the degree of alignment of the magnetic domains that can be obtained. The presence of thermal vibrations prevents

complete alignment of the dipoles; saturation magnetization is therefore at its maximum value at 0K but is reduced as the temperature increases (Figure 2-10). Remanent magnetization ( $B_R$ ) is the degree of magnetization which persists in the material after the applied magnetic field is reduced to zero. The coercivity of the material ( $H_C$ ) reflects the amount of reverse magnetic field required to reduce the magnetization back down to zero. Materials with high coercivities are considered magnetically “hard” materials, while “soft” magnetic materials have low coercivity values. By applying a magnetic field  $H$ , the domains that compose the material are aligned in the direction of the applied field. Increasing the applied field improves the alignment until all the domains are aligned in the same direction; at this point the material has reached its maximum level of magnetization and is magnetically saturated. If the applied field is removed the domains are allowed to misorient in order to reduce the material’s magnetostatic energy. Some directional orientation is preserved, however, and the magnetization is reduced to the remanent magnetization level.

#### **2.2.3.4 Anisotropy**

The hysteresis loop of a material can provide a lot of information about the magnetization behaviour of a particular material. The orientation of a ferromagnetic object in relation to the magnetizing field, however, can produce hysteresis loops with radically different characteristics. This behaviour is called magnetic anisotropy and is due to the fact that materials are more easily magnetized in some directions than others. The direction along which a material is most easily magnetized is the “easy” axis of magnetization, while the most difficult direction of magnetization is the “hard” axis. Figure 2-14 shows the magnetization behaviour for cobalt when magnetized along its easy and hard axes.





**Figure 2-14:** Magnetization curves for a single crystal of Co along its hard and easy axis [Kaya28].

Anisotropy is typically expressed by the anisotropic energy, which is the amount of additional energy required to magnetize a material from its easy direction to its hard direction. The anisotropy of a material comes primarily from the effects of three different sources of anisotropic energy: crystallographic, shape and stress anisotropy. Anisotropy in materials can be induced through special processing such as magnetic annealing. Magnetic annealing will be explained further in Section 2.2.3.4.4.

#### 2.2.3.4.1 Crystallographic Anisotropy

Crystallographic anisotropy stems from the preference for atoms to align their dipoles in a particular direction with respect to their crystallographic configuration. This is the only source of anisotropy which is intrinsic to the material itself. For cubic crystals, the crystallographic anisotropy energy can be described by the expression:

$$E_C = K_0 + K_1(\alpha_1^2\alpha_2^2 + \alpha_2^2\alpha_3^2 + \alpha_3^2\alpha_1^2) + K_2(\alpha_1^2\alpha_2^2\alpha_3^2) + \dots \quad (2.2.10)$$

where  $\alpha_i$  are the cosines between the direction of magnetization and the crystal axes and  $K_N$  are constants for a particular material, in ergs/cm<sup>3</sup> [Cullity72]. Generally, the  $K_N$  values greater than  $K_2$  are considered negligible. The easy axis of magnetization is the direction of magnetization which minimizes the value of  $E_C$ .

Fundamentally, this behaviour is known to result from the coupling of the magnetic moments between the spin and orbit of the electrons; however, the specifics of the behaviour are not well understood. As a result, it is not yet possible to predict the anisotropy constants and anisotropy must be determined experimentally. There are, therefore, no precise rules for determining the easy axis of magnetization based on crystal structure. For instance, pure Ni has a FCC crystal structure and a  $\langle 111 \rangle$  easy axis, however, a 25%Fe-Ni alloy has a  $\langle 100 \rangle$  easy axis, even though the FCC crystal structure is retained [Cullity72].

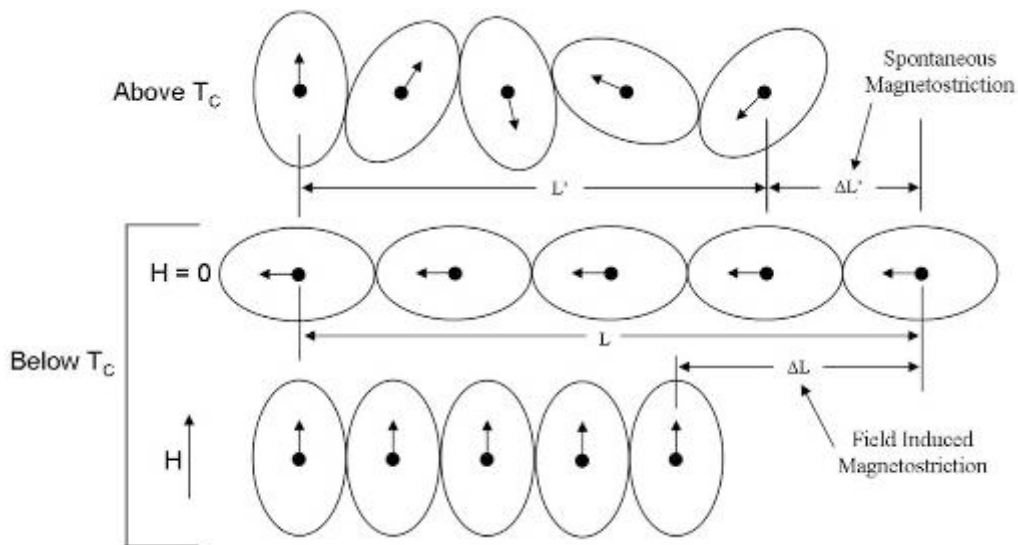
#### **2.2.3.4.2 Shape Anisotropy**

As stated in Section 2.2.3.1, the magnetization of a material leads to the formation of free poles on the material's surface. These free poles lead to the formation of magnetostatic energies caused by the demagnetizing field which is produced in magnetized materials. The demagnetizing energies required to magnetize the material along the short axis are higher because the free poles form over a larger surface area. This leads to the preference for materials to magnetize along their long axis. The effects of shape anisotropy are non-existent in spherical particles as all their axes are equivalent.

#### **2.2.3.4.3 Stress Anisotropy**

Magnetization of a material is often accompanied by a change in the material's dimensions; this effect is known as magnetostriction ( $\lambda$ ).

Magnetostriction results from the interaction between the magnetic moment of an atom and the shape of the electron cloud that surrounds it. Materials that display magnetostriction have electron clouds which are elliptical, the long direction of the ellipse is related to the direction of magnetization. The elliptical electron clouds cause neighbouring atoms to be pushed further away from each other in one direction. Thus, when the direction of magnetization is changed, the dimensions of the material are also changed. This behaviour is depicted in Figure 2-15. Stresses, which oppose the magnetostrictive effect, make it more difficult to magnetize the material in that direction leading to the formation of a hard axis. Conversely, stresses that complement the magnetostrictive tendency of the material improve the ease of magnetization in that direction.



**Figure 2-15:** Electron orbital influence on the magnetostrictive effect; based on figure from [Cullity72].

#### 2.2.3.4.4 Magnetic Annealing

Magnetic annealing is a process by which an easy axis of magnetization can be induced in a material through a heat treatment followed by cooling in the presence of an external magnetic field. In ferromagnetic materials, magnetic annealing results in the formation of uniaxial anisotropy with an easy axis parallel

to the direction of the external magnetic field. To be effective, magnetic annealing is performed at a temperature below the material's Curie temperature, but must be high enough to allow for significant atomic diffusion. The magnetic field must also be strong enough to saturate the material if the highest possible uniaxial anisotropy is to be produced. Since the external field only determines the direction of the anisotropy, an alternating magnetic field is as effective as a unidirectional field [Cullity72].

In solid solutions there is a tendency for like-atoms to align parallel to the direction of magnetization; this phenomenon is known as directional ordering. During the annealing process, the ferromagnetic material is heated to allow for easier diffusion of its atoms. The application of an external magnetic field then creates a slight preference for like atoms to order parallel to the field; this persists in the material even after it has been cooled. The mechanism by which directional ordering leads to the formation of uniaxial anisotropy is not well understood; however, it is theorized that it is related to spin-orbit coupling effects. These coupling effects lead to the formation of an easy axis in the direction of magnetization [Cullity72].

## 2.3 Electrodeposition

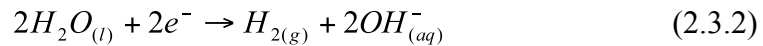
### 2.3.1 The Electroplating Cell

The electroplating cell is composed of 5 fundamental components: a DC power source, an electrolytic plating solution, solid electronic conductors (usually wires), and two electrodes which act as the anode and cathode. The electrodes are submerged in the electrolytic solution and connected electrically to the DC power source; the anode to the positive terminal and the cathode to the negative terminal [Kanani04, Paunovic06]. When the power source is activated, electrons are extracted from the anode and passed to the cathode through the power source. This produces a voltage across the plating solution between the positively charged anode and negatively charged cathode. To remove accumulating charge on the electrodes, ions migrate to the electrodes' surfaces where reduction/oxidation reactions provide or consume the electrons necessary to complete the electrical circuit. A representation of a basic electroplating cell is shown in Figure 2-16.

The cathode of the electroplating cell acts as the site of metal deposition. Electrons are consumed and used to reduce aqueous metal ions into a metallic film which forms on the cathode surface [Paunovic06]:



In addition to the intended metal deposition, other side reactions are possible at the cathode. Other possible cathode reactions involve the evolution of hydrogen gas either by the reduction of water, in basic or neutral solutions [Bradford01, Paunovic06]:

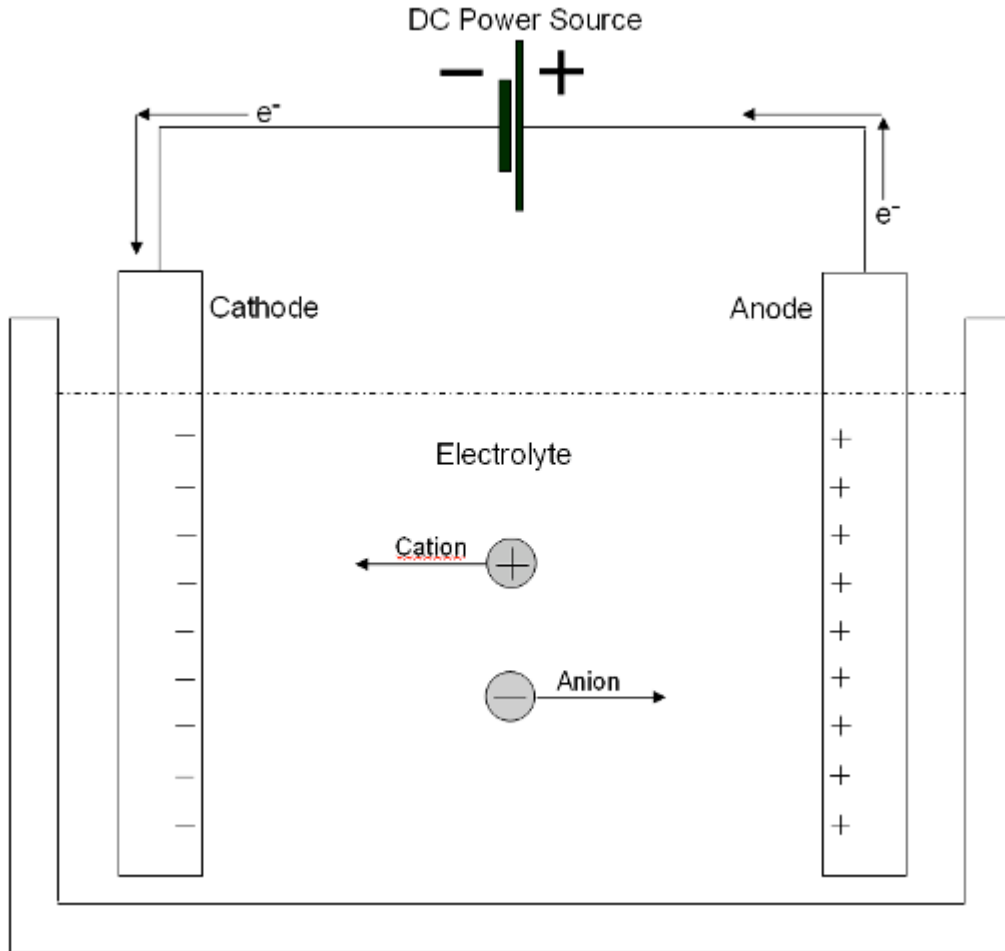


or by the reduction of hydrogen ions in acidic solutions [Bradford01, Paunovic06]:



These reactions are typically undesirable because they consume current, and thus

reduce the efficiency of the electroplating cell. The evolution of hydrogen at the cathode also produces bubbles which interfere with deposit growth and lead to porosity in the deposits [Paunovic06].

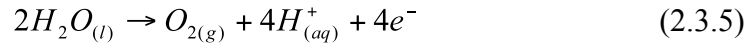


**Figure 2-16:** Basic electroplating cell.

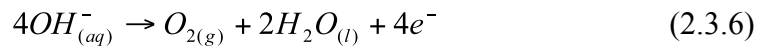
The anode complements the reduction reactions at the cathode by acting as a site of oxidation. During these reactions, free electrons are produced which are conducted to the positive terminal of the DC power source. Anode reactions involve either the oxidation of species in the electrolyte, or of the anode material itself. When the anode is itself oxidized, it dissociates into solution as metal ions. In this case the anode is consumed in the electroplating process and can be used to provide the metal ions which are plated out on the cathode [Kanani04, Paunovic06].



When an inert electrode is used, the anode reaction oxidizes species in the electrolyte. These reactions are often pH dependent and result in the evolution of oxygen gas. In neutral and acidic solutions the anode reaction typically proceeds as [Bradford01]:



In basic solutions, the anode reaction usually involves the oxidation of hydroxide ions [Bradford01].



### 2.3.2 Deposition rate and current efficiency

Unlike the conduction of electricity in a metal, which occurs via a conduction band, conduction through an electrolytic solution during electroplating occurs through the movement of charged ions. This phenomenon is known as “conductance of the second kind” [Raub67] through a plating solution, which limits the rate at which electrode reactions can occur and therefore is closely related to the rate of metal deposition. The relationship between current and deposit thickness can be expressed by:

$$\frac{x}{t} = \frac{\Phi i A}{\rho n F} \quad (2.3.7)$$

where  $x$  is the thickness of the deposit,  $t$  is the time,  $\Phi(\leq 1)$  is the cathode current efficiency,  $i$  is the current density,  $A$  is the molar mass of the metal,  $\rho$  is the mass density of the deposit,  $n$  is the number of electrons required to reduce each ion to its neutral state and  $F$  is the Faraday constant (96,485.34 C/mol) [Sun98]. Current efficiency ( $\Phi$ ) is a measure of the amount of current which is used in the intended reaction. Side reactions, such as the evolution of hydrogen at the cathode, will lower the current efficiency.

### 2.3.3 Electrode potentials

When a metal is placed in a solution of its own ions, equilibrium is established between the ions dissociating into the solution and the ions adsorbing onto the metal surface. Metal ions dissociating into the solution leave the metal electrode with an excess of electrons and it becomes negatively charged relative to the solution. When metal ions adsorb onto the surface of the electrode then there is an electron deficiency on the metal surface and it is positively charged relative to the solution [Tan93]. The charge on the electrode surface repels similarly charged ions and attracts oppositely charged ions. This results in the formation of a concentration gradient with a relative abundance of oppositely charged ions immediately adjacent to the metal surface. The space between the charged metal surface and the layer of oppositely charged ions adjacent to it is known as the double-layer. The potential across the double layer is the surface potential of the metal. Many different models have been used to describe the nature of charge distribution in the double layer. The simplest assumes that the double-layer is analogous to a capacitor where oppositely charged ions line up along a plane at a fixed distance from the electrode surface. The plane along which the ions are lined is called the Helmholtz plane and its distance from the electrode is determined by the hydration sphere of water molecules which surround the ions. This model is known as the Helmholtz compact double-layer model. [Paunovic06]

Electrode potential can be used as an indication of the relative stability of a metallic species. Species which tend not to dissociate into solution, i.e., have a positive electrode potential are considered noble and are easily reduced. Species which easily dissociate into solution, i.e., have a negative electrode charge, are anodic and are oxidized. The electrode potential is only a relative value and is usually reported in comparison to the reduction potential of hydrogen under standard conditions. Standard conditions are 1 molar ion concentration, 1 atm of pressure and 25°C [Paunovic06]. The standard electrode reduction potentials of several species are shown in Table 2-3.



**Table 2-3:** Standard electrode potentials [Milazzo78].

Metal/Metal-Ion Couple	Electrode Reaction	Standard Value (V)
Au/Au <sup>+</sup>	Au <sup>+</sup> + e ⇌ Au	1.692
Au/Au <sup>3+</sup>	Au <sup>3+</sup> + 3e ⇌ Au	1.498
Pd/Pd <sup>2+</sup>	Pd <sup>2+</sup> + 2e ⇌ Pd	0.951
Cu/Cu <sup>+</sup>	Cu <sup>+</sup> + e ⇌ Cu	0.521
Cu/Cu <sup>2+</sup>	Cu <sup>2+</sup> + 2e ⇌ Cu	0.3419
Fe/Fe <sup>3+</sup>	Fe <sup>3+</sup> + 3e ⇌ Fe	-0.037
Pb/Pb <sup>2+</sup>	Pb <sup>2+</sup> + 2e ⇌ Pb	-0.1262
Ni/Ni <sup>2+</sup>	Ni <sup>2+</sup> + 2e ⇌ Ni	-0.257
Co/Co <sup>2+</sup>	Co <sup>2+</sup> + 2e ⇌ Co	-0.28
Fe/Fe <sup>2+</sup>	Fe <sup>2+</sup> + 2e ⇌ Fe	-0.447
Zn/Zn <sup>2+</sup>	Zn <sup>2+</sup> + 2e ⇌ Zn	-0.7618
Al/Al <sup>3+</sup>	Al <sup>3+</sup> + 3e ⇌ Al	-1.662
Na/Na <sup>+</sup>	Na <sup>+</sup> + e ⇌ Na	-2.71

It should be noted that the above values are only under standard conditions, and do not reflect the electrode potentials of the same species at different temperatures, pressures, and ion concentrations. Under non-standard conditions, electrode potentials can be calculated using the Nernst equation:

$$E = E^0 - \frac{RT}{nF} \ln \left( \frac{\prod([\text{reduced}]^i)}{\prod([\text{oxidized}]^j)} \right) \quad (2.3.8)$$

where R is the gas constant, T is the absolute temperature, n is the number of electrons exchanged, and F is the Faraday constant (96 485.339 C/mol) [Paunovic06].

### 2.3.3.1 Overpotential

Under equilibrium conditions, charge carriers pass through the double layer in opposite directions at the same rate. There is thus no net gain or loss of atoms on the electrodes in such situations. For electroplating to be possible, a current must be made to flow in one net direction. The shift in potential that arises due to a flow of current is known as the “polarization” [Bradford01]. A current can be generated internally, such as in a galvanic cell, or through the application of a voltage via an external power source. Electrodeposition uses an external voltage to induce the deposition of metallic species which would otherwise be

energetically unfavorable. The voltage across the cell, however, must not only overcome the reduction potential of the material, but must also overcome several hindrance effects associated with electrode reactions and mass transport in the plating cell. The additional voltage is called the overpotential ( $\eta$ ), and is represented by:

$$\eta = E_i - E_{eq} \quad (2.3.9)$$

where  $E_i$  is the potential across the cell, and  $E_{eq}$  is the equilibrium electrode potential. The total overpotential of an electrolytic cell is the sum of several hindrance effects: activation overpotential ( $\eta_A$ ), concentration overpotential ( $\eta_C$ ), and resistance overpotential ( $\eta_R$ ) [Bradford01].

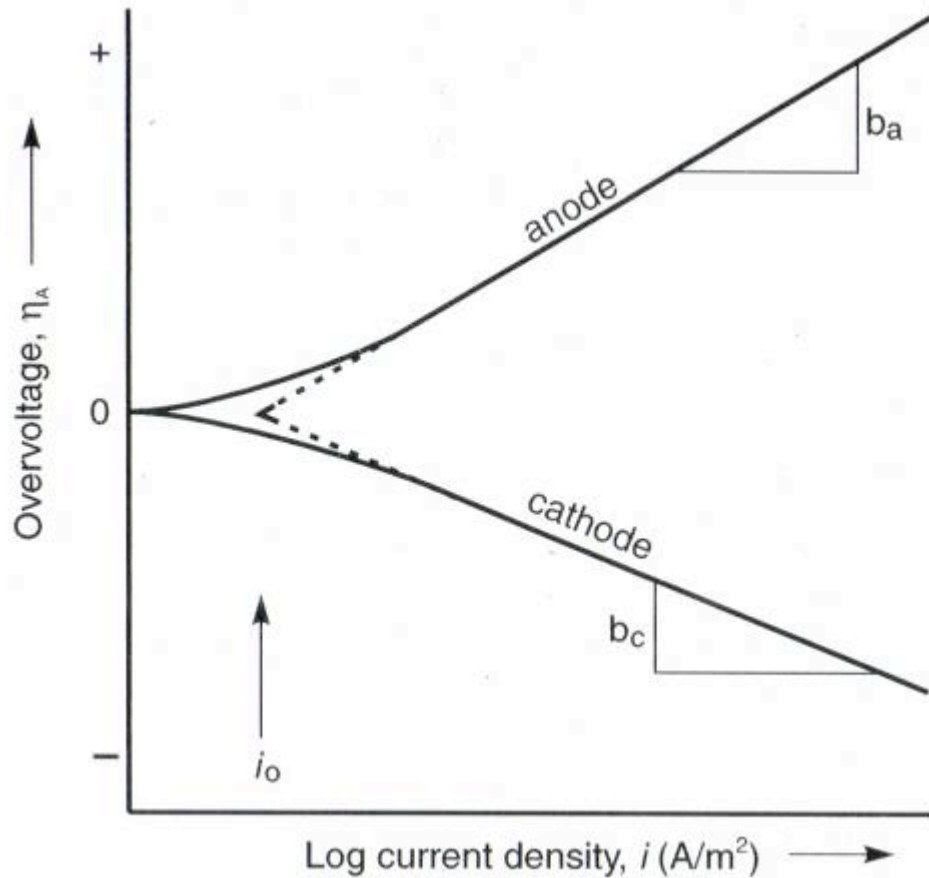
Activation overpotential ( $\eta_A$ ) is the voltage required to overcome the energy barrier for the electrode reactions to occur. Electrode reactions are not one step reactions, but the results of several phenomena: transfer of ions across the double layer, adsorption and desorption of species on the electrode surface, the reaction itself, and incorporation of the metal ad atoms into the lattice [Paunovic06]. For the sake of this explanation we will consider these effects collectively as the activation potential. Increasing the voltage across the cell increases the charge on the electrodes, which means that reactants are attracted, and products repelled, faster to and from the electrode surface. At high overpotentials, the relationship between activation overpotential and current can be described using the Tafel equation:

$$\eta_A = \pm b \log \frac{i}{i_0} \quad (2.3.10)$$

where  $i$  is the current density,  $i_0$  is the exchange current density (i.e., current density when the overpotential is zero) and  $b$  is the constant known as the Tafel slope which is positive at the anode and negative at the cathode [Bradford01]. The Tafel equation, however, does not hold within  $\pm 50\text{mV}$  of the equilibrium potential [Bradford01]. At low potentials, overpotential can be described by the equation:

$$\eta_A = \frac{i_0 n F}{i R T} \quad (2.3.11)$$

Experimentally measured activation polarization curves for both the anode and cathode are shown in Figure 2-17.



**Figure 2-17:** Activation polarization curves for both high and low overpotentials. Dotted lines show extrapolated Tafel slopes which intersect at the exchange current density value [Bradford01].

As electrodeposition proceeds reactants near the electrodes are consumed, which results in a concentration gradient between the electrode surfaces and the bulk solution. The concentration overpotential ( $\eta_c$ ) is the voltage required to overcome the concentration gradient that forms near the electrode surface [Bradford01]. At low overpotentials, reactants diffuse to the cathode fast enough that the effects of the concentration gradient are not obvious and the activation overpotential dominates the system. The effects of concentration overpotential are not typically observed until relatively high overpotentials where the scarcity of

reactants near the electrode's surface begins to impede electrode reactions. Increasing the overpotential further will cause ions to diffuse through the concentration barrier more quickly allowing the current density to increase; however, at some point the concentration gradient between the electrode surface and the bulk solution becomes so wide that reactants are consumed faster than they arrive; at this point a limiting current density ( $i_L$ ) is reached [Bradford01]. The concentration overpotential can be described by the equation:

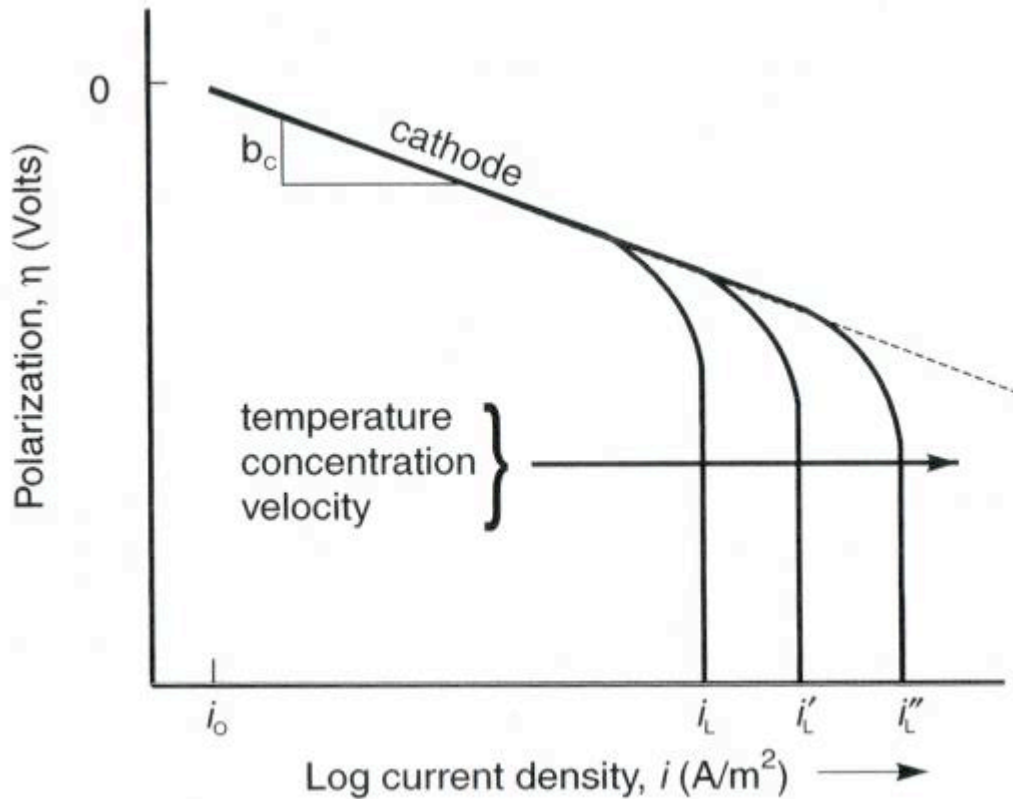
$$\eta_c = \frac{RT}{nF} \ln \left[ \frac{(1-i)}{i_L} \right] \quad (2.3.12)$$

The limiting current density can be increased by reducing the width of the concentration gradient; this can be accomplished by agitating the solution, increasing the concentration of reactants in the solution, or by increasing the solution temperature [Bradford01]. The effect of concentration overpotential and the results of decreasing the diffusion layer thickness are shown in Figure 2-18.

The resistance overpotential is the additional voltage necessary to overcome the intrinsic resistance of the electrolyte and the product films on the electrodes. This can be easily described using Ohm's Law:

$$\eta_r = IR \quad (2.3.13)$$

where I is the current and R is the resistance between the anode and the cathode. Resistance (R) is directly proportional to the current path length [Bradford01].



**Figure 2-18:** Effect of concentration overpotential on a cathode polarization curve. Influence of increasing temperature, concentration and agitation on the limiting current density [Bradford01].

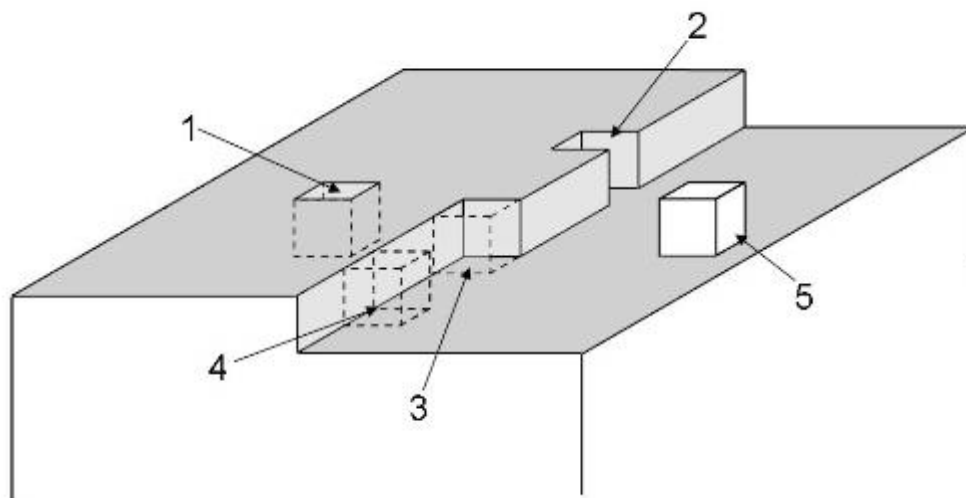
### 2.3.4 Metal Deposition

Metal deposition involves the migration of cations out of the bulk solution, across the double layers, and onto the metal surface. This process is, however, complicated by the fact that cations, due to their positive charge, are often complexed by other species while in the bulk solution. Before the cation can be deposited on the cathode these complexing agents must be stripped. Stripping these complexing agents from the metal cations requires additional energy and, depending on the stability of the complex, can greatly increase the necessary activation overpotential [Raub67]. Complexing agents are often used beneficially as a means of stabilizing particularly noble metal species in solution and to aid in

their codeposition.

In the simplest case, metal cations are complexed by surrounding water molecules to form hydrated cation complexes. The formation of these complexes is favorable because water, being a polar molecule, has a dipole which allows a weak bond to be formed between the positively charged cation and the slight negative charge on the oxygen atom in water molecules [Raub67]. This results in the formation of a water envelope around the cations. When the charged ions contact the cathode surface they lose most of their charge and as a result most of the water envelope surrounding them is also lost [Kanani04]. Partial charge on the adsorbed atoms (“ad-atoms”) remains, however, until they are incorporated permanently into the deposit. Only when the ad-atom permanently integrated into the deposit is the water envelop completely shed.

Cations, once they contact the cathode surface, are reduced to their atomic form and attempt to incorporate themselves into the deposit. Depending on the location at which these ad-atoms contact the cathode surface, they may not be immediately incorporated into the metal lattice [Paunovic06]. In general, the stability of the ad-atom is a function of the number of metallic bonds that it can form with the cathode surface. Positions such as vacancies and ledges, formed by incomplete layers of deposit, are favorable positions for ad-atoms; these are known as “kink sites”. If an ad-atom does not form a stable bond with the metal surface upon adsorption, it will migrate across the surface until a suitable kink site is reached [Paunovic06]. Possible sites for ad-atom addition are depicted in Figure 2-19 and are numbered in decreasing order of stability.



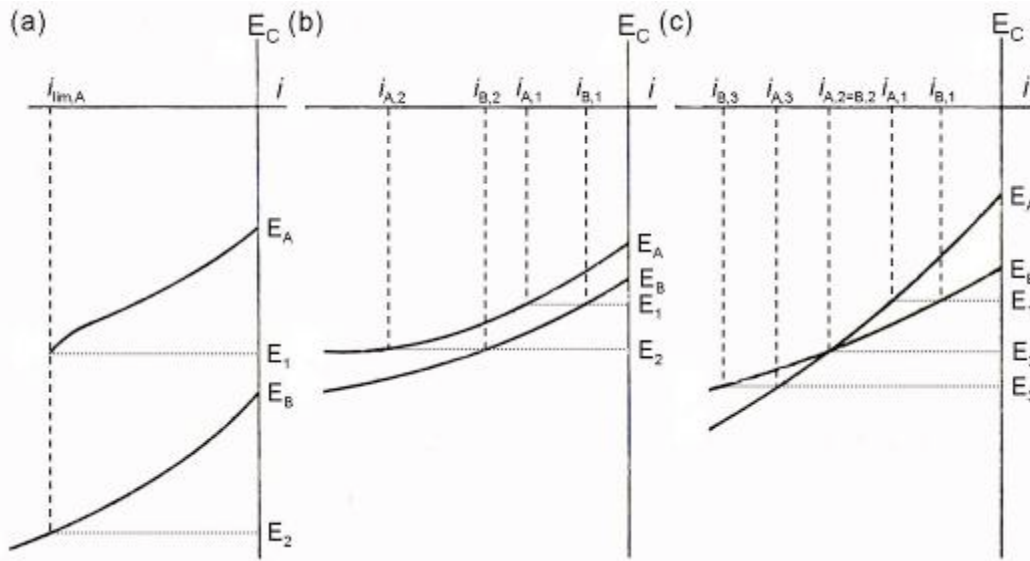
**Figure 2-19:** Possible sites for ad-atom addition onto a metal surface; numbering in decreasing order of stability; based on figure from [Paunovic06].

From Figure 2-19, it can be seen that vacancy sites (1) provide ad-atoms with an opportunity to form the most possible number of bonds with the surrounding surface. They are, therefore, very favorable to ad-atom addition; these sites, however, are not very common. Ledge sites (2-4) do not allow ad-atoms to form as many bonds as vacancies, but are much more common. The formation of a new layer of atoms (5) is the least favorable because the ad-atom only forms one bond with the deposit.

### 2.3.5 Alloy co-deposition

Codeposition of an alloy involves the simultaneous deposition of more than one metal species from the same plating solution. While similar in principle to the deposition of a single metal species, codeposition presents its own set of challenges and requires that much tighter control be exercised over plating conditions in order to produce the desired alloy composition. More noble metal species preferentially deposit on the cathode often to the exclusion of less noble metals [Lowenheim78]. Since an electrode can have only one potential at any

particular moment, in order for co-deposition to occur, the potential at the cathode must be sufficient for the deposition of both metal species. Figure 2-20 shows the polarization curves for several systems involving two cationic species.



**Figure 2-20:** Cathode potential polarization graphs for possible two cation systems [Raub67].

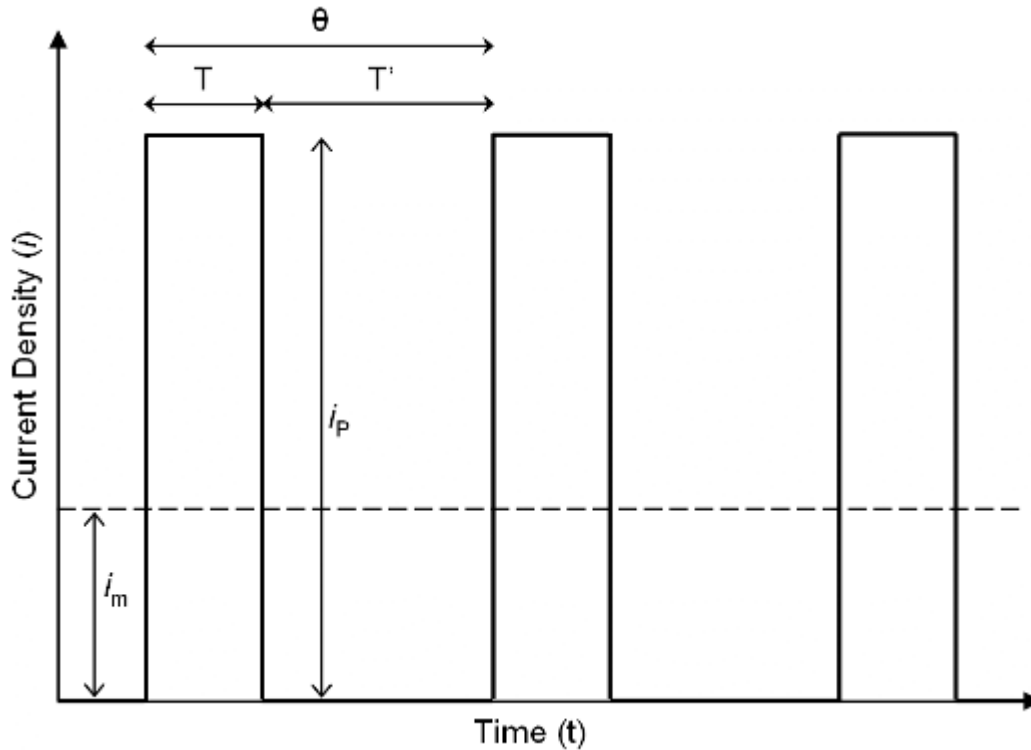
Figure 2-20 (a) shows a situation in which two cationic species having significantly different reduction potentials are deposited. When a negative potential greater in magnitude than  $E_A$  is applied across the cell then the more noble species A will be reduced at the cathode. As the potential is increased in magnitude from  $E_A$  to  $E_1$ , the plating rate of the metal is increased which is indicated by the increasing current density. At  $E_1$  the limiting current density is reached and any increase in the magnitude of the negative potential beyond this point does not change the deposition rate of species A. At  $E_1$ , however, the potential is still too low to reduce species B. Only when the negative potential is increased beyond  $E_B$ , will the two species be co-deposited. Increasing the potential in the negative direction further will increase the relative amount of species B in the deposit; and a 50:50 deposit will result when a potential equivalent to  $E_2$  is used. Figure 2-20 (b) shows a situation with two species whose polarization curves lie close together. In this case a much lower potential is



required to co-deposit the two species. The ratio of cation deposition between the two species is equivalent to the ratio between the current densities for the species. Therefore at  $E_1$  the deposit should have a composition of  $\sim i_{A,1}:i_{B,1}$ . When the negative potential is increased to  $E_2$  the ratio between the species becomes  $\sim i_{A,2}:i_{B,2}$ . This shows how small changes in overpotential can greatly affect the overall composition of some alloys. Figure 2-20 (c) shows a situation where the polarization curves cross. While at  $E_1$  species A plates preferentially to species B, at  $E_3$  this trend is reversed and the less noble metal (B) has the faster deposition rate. At the point where the two curves cross,  $E_2$ , both species plate at the same rate and an alloy with a 50:50 composition should theoretically result.

### 2.3.6 Pulse Electrodeposition

Unlike regular DC electrodeposition, pulse electrodeposition uses an intermittent current to repetitively deposit thin layers of metal on the cathode surface. An example of a pulsed electrodeposition waveform is shown in Figure 2-21. From Figure 2-21 it can be seen that there are three independent manipulable parameters, which can be adjusted to alter the waveform: the pulse current density  $i_p$ , the on-time  $T$  and the off-time  $T'$  (during which the current density may or may not equal zero), the average current density  $i_m$  and the complete cycle time  $\theta$  resulting from the manipulation of these parameters [Ibl80].



**Figure 2-21:** Possible waveform of pulsed electrodeposition [Ibl80].

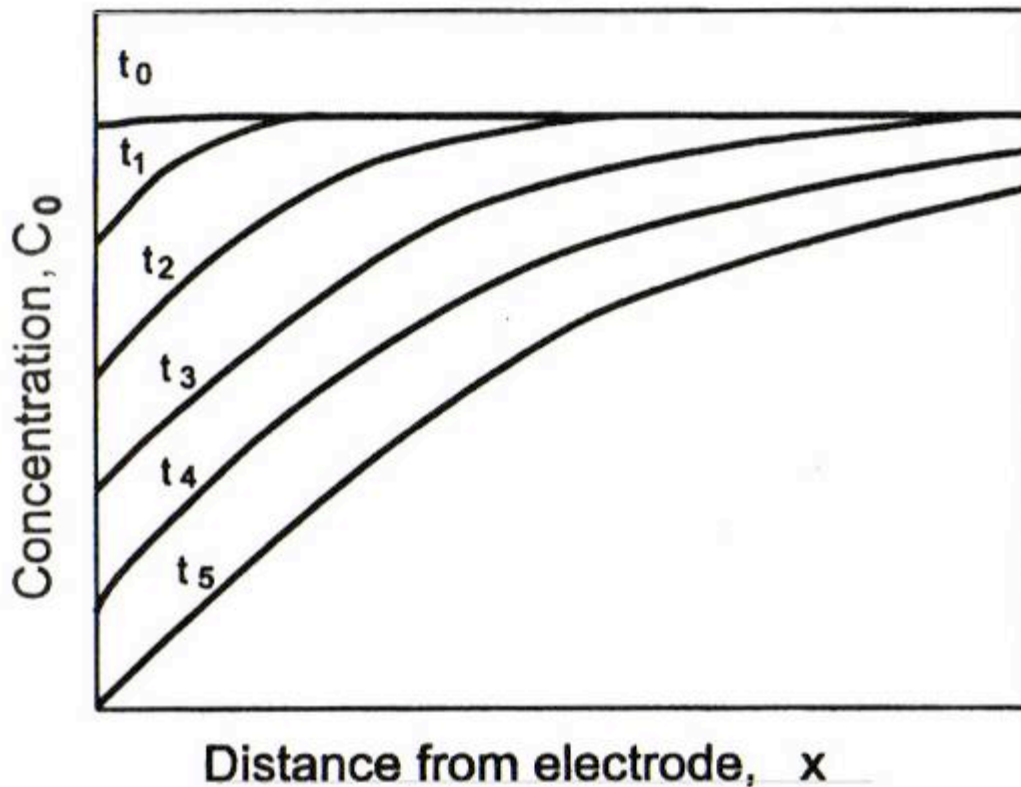
The overall rate of deposition is controlled by the average current density, which can be related to the pulsed electroplating parameters by the equation:

$$i_m = i_p \frac{T}{(T + T')} \quad (2.3.14)$$

The use of repetitive electrical pulses produces two important features in pulsed electrolysis. Firstly, it enables the generation of high instantaneous current densities/potentials. Producing high potentials allows the operator to manipulate the rate of reactions of species at the cathode surface. It can also greatly increase the nucleation rate at the cathode [Ibl80]. Pulsed electrodeposition, therefore, tends to produce a finer grain structure. The second feature is the off-time which allows for adsorption and desorption phenomena as well as recrystallisation phenomena at the deposit to occur [Ibl80]. As a result, pulse electrodeposition allows for much more flexibility during plating in comparison to regular DC electrodeposition. Pulsed electrodeposition has been used to improve the properties and quality of cathode deposits, as well as to increase the operational

control over plating rate and thickness [Gladstein02]. These abilities make pulse electrodeposition very attractive for use in electronics.

Initially during electrodeposition there is a rapid decrease in cationic species near the cathode as they are plated out of solution. This produces a concentration gradient immediately adjacent to the cathode surface. This effect is even faster in pulse electrodeposition where the current densities used are usually much higher than those used during regular DC electrodeposition. As the pulse is prolonged the concentration gradient extends further away from the cathode [Ibl80]. This phenomenon is demonstrated in Figure 2-22.



**Figure 2-22:** Reactant concentration change near an electrode as a function of time [Ibl80].

At the termination of the pulse the cations in the depleted region are replenished through diffusion from the bulk solution. Hence, at the cathode, the concentration of cationic species pulsates with the same frequency as the current [Ibl80]. During

pulse electrodeposition, it is generally preferable to use very short bursts of high density current followed by off-times long enough for the replenishment of the diffusion layer. This is not only to promote the formation of grain nuclei, but also as a means of maintaining a uniform rate of deposition over the entire cathode surface.

During normal DC electrodeposition, a diffusion layer is established at a set distance from the cathode. Since cations must diffuse across the diffusion layer in order to be deposited, areas where the diffusion layer is thinner are established as points of preferred deposition. By keeping the on-time brief when using pulse electrodeposition, the diffusion layer is kept very thin and coherent to the cathode's surface. This results in much more uniform deposition over the cathode's surface. These effects are depicted in Figure 2-23 where the dashed-line represents the diffusion layer,  $\delta$  is the thickness of the diffusion layer and the arrows represent areas of preferred deposition [Ibl80].

Pulsed electrodeposition can also aid in leveling the surface of the deposits if the current is temporarily reversed during the off-times. By reversing the current, the cathode temporarily becomes anodic which causes some of the deposited metal to be oxidized back into solution. This may seem counter-productive to the aims of electroplating, however, if the diffusion layer is allowed to progress far enough away from the cathode surface, oxidation will occur preferentially on the elevation points of the deposit resulting in the elimination of elevated points on the cathode's surface.

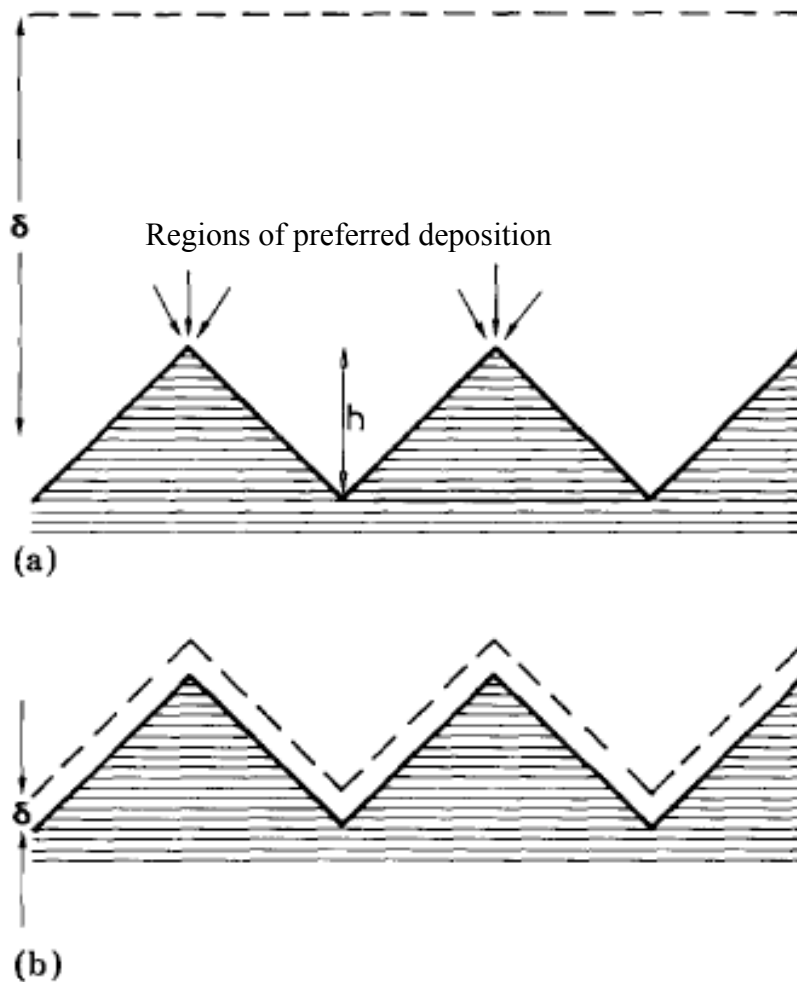
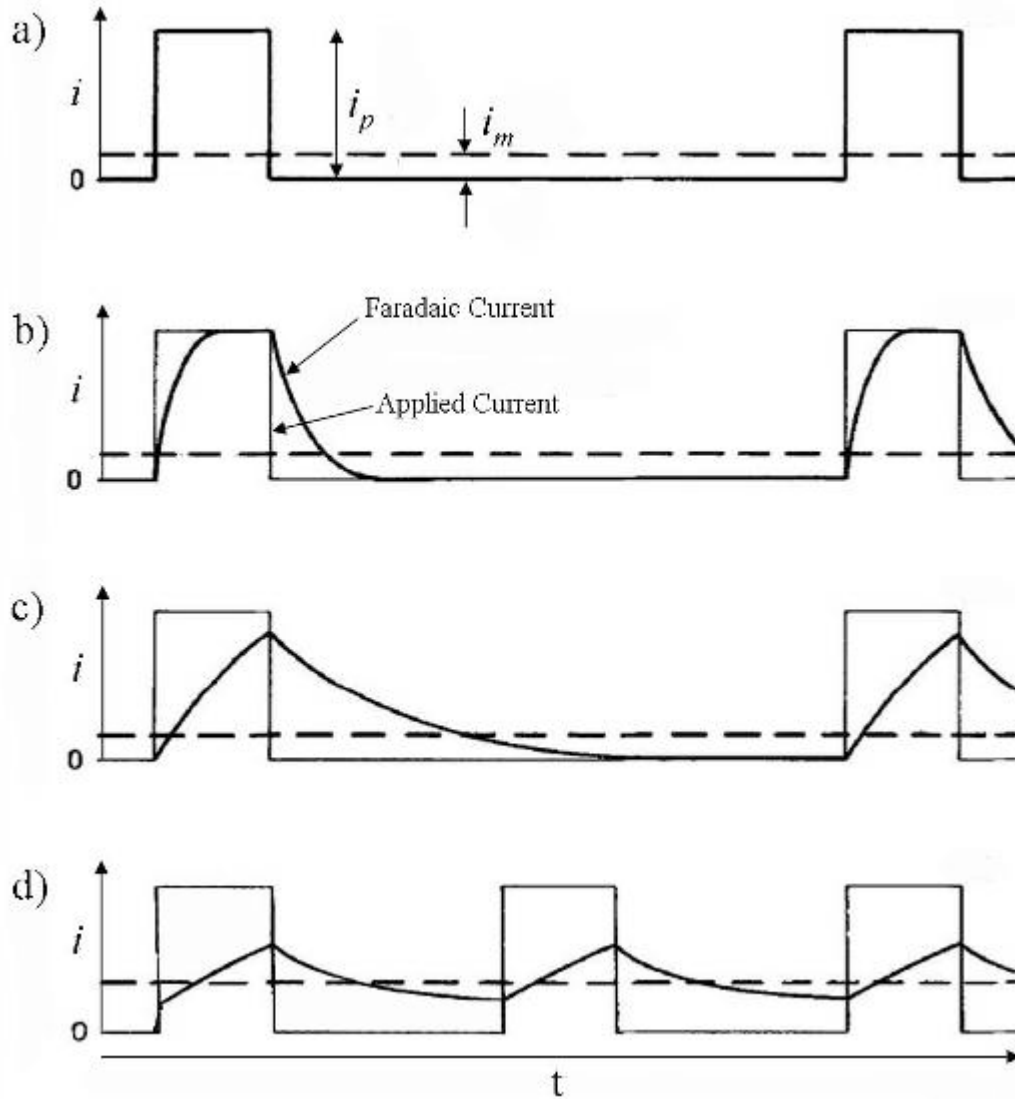


Figure 2-23: Effects of diffusion layer thickness on preferential deposition [Ibl80].

During pulsed electrodeposition the waveform that is expected based on the applied current may not reflect the electrical behavior in the actual system. The waveform used in pulsed electrodeposition is susceptible, by varying degrees, to distortion effects caused by capacitance in the electronic double layer near the cathode surface [Ibl80]. The effect can be approximated as a plate capacitor with a gap of less than 1 nm. [Ibl80]. The capacitance of the electrical double layer affects the waveform by initially absorbing much of the applied current to charge the electrical double layer and by retaining and slowly dissipating current after the current pulse has stopped. The effects of these capacitance effects are shown in Figure 2-24, where the thin lines represent the applied current across the electroplating cell and the thick lines represent the Faradaic current, i.e., the current used in deposition at the cathode.



**Figure 2-24:** Distortion of an applied waveform due to capacitance effects during electrodeposition [Puipe80]. Case (a) represents a negligible capacitance effect, case (b) represents a moderate effect, and cases (c) and (d) display severe capacitance effects.

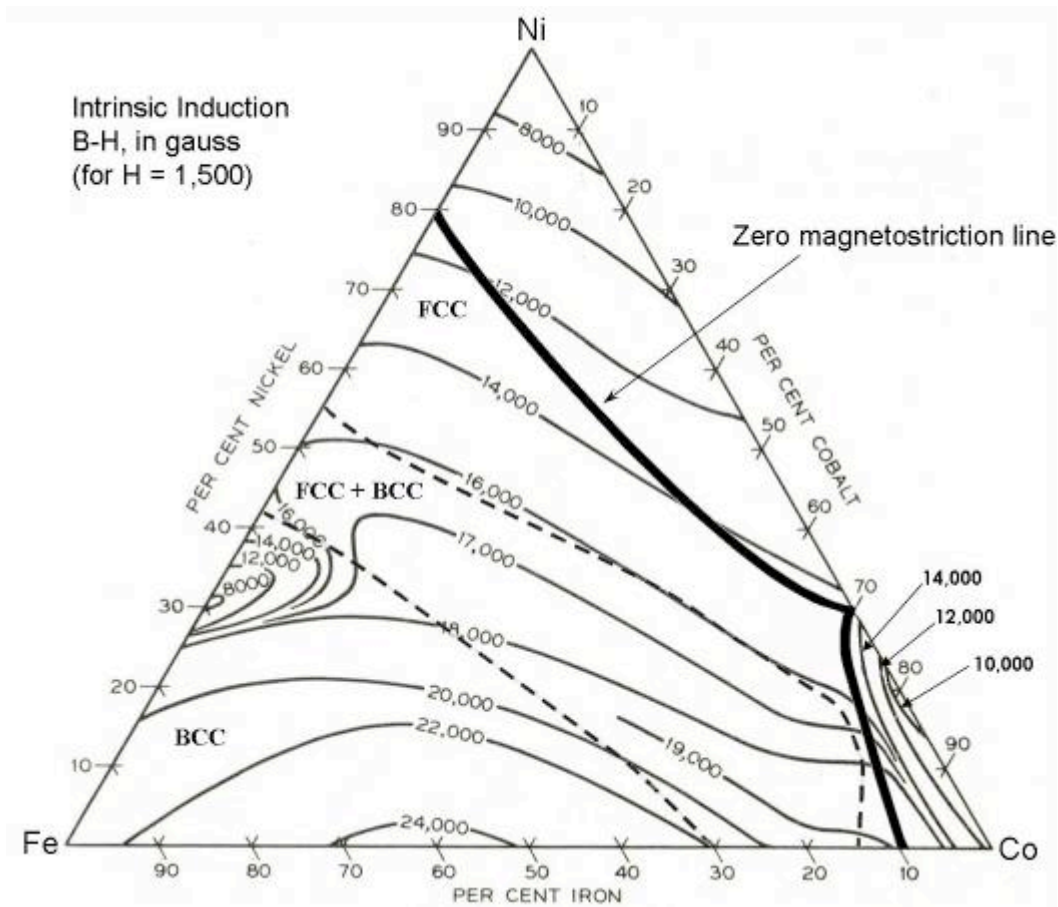
## 2.4 Soft-Magnetic Thin-Film

### 2.4.1 Electrodeposition of thin-films for write heads

In addition to electrochemical deposition, other thin-film techniques such as sputtering and vapour deposition have been studied as methods for the manufacturing of write heads. These so called “vacuum processes” have, however, several disadvantages when compared to electrochemical methods, and so have not been extensively used in thin-film write head fabrication. Electrodeposition allows for the possibility of quickly producing relatively thick metal deposits ( $>1\mu\text{m}$ ). It is also much less expensive than vacuum processes, involving a much lower capital investment in equipment, and can be easily scaled for industrial manufacturing. By electroplating through a nonconductive mask, electrodeposition also allows for tight control of dimensional parameters, which allows for the formation of small features such as pole tips. Vacuum processes are non-selective in their deposition and so require subtractive processes such as ion milling and etching to produce small features. These factors make electrodeposition the method of choice for write head fabrication.

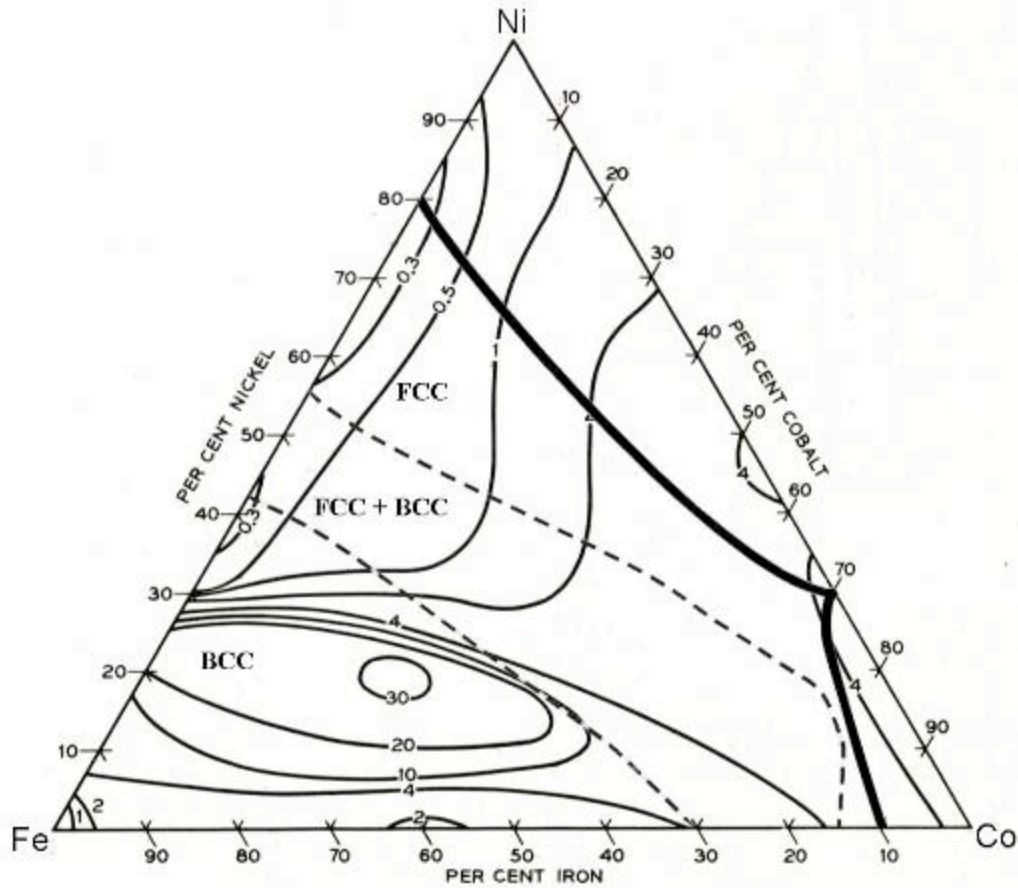
Since the physical separation of read and write heads in the 1990's made it possible to optimize the soft magnetic properties of write heads, researchers have examined the suitability of many different alloys as core materials [Cooper05]. The bulk of the research has involved examination of alloys containing the three ferromagnetic elements: iron, cobalt and nickel. Bulk properties of ferromagnetic materials are described in great detail by Richard M. Bozorth. His work, Figure 2-25, shows approximate saturation flux densities of bulk annealed alloys in the Fe-Ni-Co tertiary system [Bozorth51]. From the diagram it can be seen that the highest saturation flux densities for bulk alloys in the iron-cobalt-nickel system are iron-rich, iron-cobalt alloys which have a maximum value of  $\sim 2.4\text{T}$ . Coercivities for bulk alloys of the Fe-Ni-Co tertiary system are shown in Figure 2-26. This diagram shows that the lowest coercivities obtained for annealed bulk

alloy are in the iron-nickel system, and the iron-cobalt system conversely tends to have significantly higher coercivities. It should be stressed, however, that the values in these figures are for bulk annealed alloys. Electrodeposited thin-films may have values which differ significantly from these values due to morphological phenomena, stress and the inclusion of impurities. Coercivity in particular tends to be very sensitive to plating parameters.



**Figure 2-25:** Tertiary diagram showing the saturation flux densities of bulk, annealed CoFeNi alloys [Bozorth51]. Dotted lines separate the BCC, FCC and mixed phase regions [Cooper05]. Not shown is the HCP phase region.



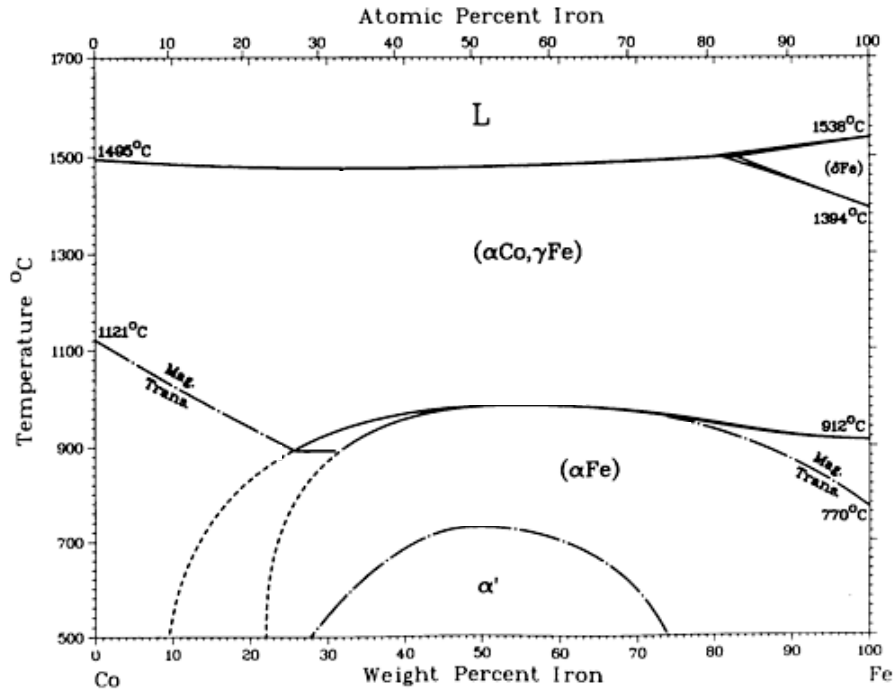


**Figure 2-26:** Tertiary diagram showing the coercivities of bulk, annealed CoFeNi alloys [Bozorth51]. Dotted lines separate the BCC, FCC and mixed phase regions [Cooper05]. Not shown is the HCP phase region.

#### 2.4.2 Iron-cobalt thin-films

Iron-cobalt alloys have been extensively studied by scientists due to their potential to produce the highest saturation flux densities of the iron-cobalt-nickel system ( $B_S \sim 2.4\text{T}$  at  $\sim 50\text{-}70\text{ wt}\%\text{Fe}$ ) [Bozorth51]. These alloys, however, also tend to suffer from higher bulk coercivities. This is not intrinsic of the alloys themselves and coercivity can be ameliorated through careful control of the stress and morphological features in the deposits. In particular, very small grain sizes have been shown to greatly improve the coercivities of magnetic thin films [Herzer89, Herzer90]. The binary iron-cobalt phase diagram is shown in Figure

2-27. The phases are described in Table 2-4.



**Figure 2-27:** Iron-cobalt binary phase diagram [Baker92].

**Table 2-4:** Equilibrium phases of iron-cobalt binary system [Betteridge82, Baker92, Crystal04].

Phase	Structure	Pearson Symbol	Space Group
$\alpha$ Fe	BCC	cI2	Im3m
$\alpha'$ Fe	CsCl	cP2	Pm3m
$\gamma$ Fe/ $\alpha$ Co	FCC	cF4	Fm3m
$\delta$ Fe	BCC	cI2	Im3m
$\epsilon$ Co	HCP	hP2	P63/mmc

The binary phase diagram in Figure 2-27 shows 4 stable phases in the iron-cobalt system between 500°C and 1700°C. The  $\alpha$  phase has a BCC structure and is the stable phase at low temperatures in iron-rich alloys. A miscibility gap in the  $\alpha$

phase region of the binary phase diagram separates the  $\alpha$  phase from the  $\alpha'$  phase which has an ordered CsCl structure. The  $\delta$  phase is a second BCC phase that becomes stable at high temperatures for iron-rich alloys. At high cobalt compositions, or high temperatures, the FCC phase  $\alpha$ Co (which is isomorphous to  $\gamma$ Fe) is the equilibrium phase. There is an additional equilibrium phase in cobalt-rich alloys at low temperatures known as the  $\epsilon$  phase. The  $\epsilon$  phase has an HCP structure, however, it does not appear in Figure 2-27, because it transforms into the  $\gamma$ Fe/ $\alpha$ Co phase at temperatures above 422°C [Betteridge82].

The binary phase diagram gives a good indication of the phases that might be expected in iron-cobalt thin-films at a particular composition. Electrodeposition, however, often produces films that are composed of phases that would not be expected to be stable based on the iron-cobalt phase diagram [Cavallotti05]. The  $\alpha'$  phase for instance is almost never observed in electrodeposited thin-films [Mattoso01]. Also the range in composition over which the FCC and BCC phases can be deposited often conflicts with the region shown in Figure 2-27 [Kakuno97, Mattoso01, Myung01]. Metastable phases are also often produced through electrodeposition [Cavallotti05]. These phases often arise due to kinetic effects during the electroplating process as well as to the incorporation of impurities in the deposits [Tochitskii96, Cavallotti05].

#### **2.4.2.1 Previous research on iron-cobalt thin-films**

Due to their potential as a write head material in HDDs, researchers have extensively studied iron-cobalt thin films. Chang et al. [Chang90] electrodeposited a  $\text{Co}_{88.5}\text{Fe}_{11.5}$  alloy, which is very close to the composition of zero magnetostriction ( $\text{Co}_{89.5}\text{Fe}_{10.5}$ ). The deposits had saturation flux densities of 2T and coercivities of  $\sim 3\text{Oe}$ . Analysis using x-ray diffraction (XRD) and transmission electron microscopy (TEM) results indicated that coercivity is closely related to the grain size of the deposits. Chang et al. found that smaller grains promote lower film coercivities. Their research suggests that grain size, and thus coercivity, can be minimized through the codeposition of BCC and FCC

phases, due to competitive grain growth. This relationship has been observed and corroborated by many other research groups [Liu00, Mattoso01, Zhang07].

The relationship between grain size and coercivity is consistent with the behaviour predicted by G. Herzer [Herzer89, Herzer90]. The traditional understanding of coercivity as it relates to the grain size predicts that coercivity should increase as grain size is reduced [Herzer90]. This is because larger grains have fewer grain boundaries, which impede the rotation of domains during magnetization. Herzer's model, however, predicts that at very small sizes, less than a few tens of nanometers, the exchange interactions between the grains becomes more important and prevents the alignment of domains along the crystal's easy axes of magnetization. This effectively averages out the anisotropy of individual grains over the material, which makes the material easier to magnetize in any direction. The model predicts that coercivity is related to grain size by a factor of  $1/D$  in larger grained materials and by a factor of  $D^6$  in very small-grained materials [Herzer90].

A sulphate-based plating solution buffered with boric acid was used by Bertazzoli et al. [Bertazzoli93] to evaluate the plating behaviour of iron-cobalt alloys. They showed that the composition of the alloy is strongly related to the relative ratio of cobalt- and iron-salts in the solution but not to the plating current density or temperature. Iron plated preferentially to cobalt despite cobalt's higher reduction potential, indicating anomalous deposition behaviour in the iron-cobalt system. This was attributed to an inhibiting effect of iron(II) on cobalt nucleation and growth. The presence of iron(II) did not, however, affect the steady state deposition of cobalt(II) on the cathode.

Osaka et al. [Osaka94] investigated the effects of additives on the deposition of high-cobalt iron-cobalt-boron films. An electroless deposition method was used to produce alloys with a composition of  $\text{Co}_{89}\text{Fe}_9\text{B}_2$ . It was found that the inclusion of phosphorous acid in the plating bath and plating in a magnetic field increased the permeability of the deposits and reduced their coercivities. The optimal dosage of phosphorous acid was found to be  $0.06 \text{ mol/dm}^3$ , which resulted in deposits with coercivities lower than 1Oe and

saturation flux densities of  $\sim 1.6\text{T}$ .

The morphological and structural characteristics of  $\text{Co}_x\text{Fe}_{1-x}$  alloys films electroplated from an additive-free sulphate-based plating solution were investigated by Kakuno et al. [Kakuno97]. They concluded that the relative metal-salt composition of the plating solution reflected the composition of the deposits and, therefore, that the deposit composition can be easily and predictably controlled by adjusting the solution chemistry. During their investigations they observed the deposition of the HCP phase at compositions  $>70$  at%Co, which conflicts with the phases expected based on the iron-cobalt phase diagram. Scanning electron microscopy (SEM) analysis of their deposits showed the formation of heterogeneous morphologies and that the deposits were prone to microcracking.

Liu et al. [Liu00] used an additive-free sulphate-based plating solution to evaluate the effects of current density on iron-cobalt deposition with compositions from  $\sim 18$ -60 at%Fe. Their research indicates that at low current densities ( $<20$   $\text{mA}/\text{cm}^2$ ) the iron content of the deposits is higher than would be expected based on the solution's metal-salt ratio. At higher current densities, however, the composition of the deposits more closely reflected the metal-salt composition of the plating solution. X-ray diffraction analysis showed that almost all of the films had a BCC structure regardless of composition; the exception being films with  $<20$  at%Fe, grown from a cobalt-rich plating solution using high current densities ( $20$ - $40$   $\text{mA}/\text{cm}^2$ ). These films were deposited as the FCC phase, which is in agreement with the iron-cobalt binary phase diagram [Baker92]. Magnetic measurements from the films showed a maximum saturation flux density of  $2.04\text{T}$  in the iron-rich  $\text{Co}_{40}\text{Fe}_{60}$  deposits. These results are significantly lower than would be expected for alloys with this composition. This discrepancy was attributed to the incorporation of a non-magnetic material, such as  $\text{Fe}(\text{OH})_2$ , in the films. The coercivities of the deposits were generally between  $20$  and  $30$  Oe, however, values as low as  $12$  Oe were observed in deposits plated from a cobalt-rich plating solution using a current density of  $15$   $\text{mA}/\text{cm}^2$ . This drop in coercivity coincides with the shift from deposition of the BCC phase to the FCC phase indicating that

the low coercivity may have been due to the codeposition of the two phases.

Mattoso et al. [Mattoso01] used x-ray diffraction (XRD) to show that electroplated iron-cobalt films had phase compositions which differed significantly from those expected based on the binary alloy phase diagram [Baker92]. Their work shows that the BCC phase is the only phase deposited at compositions up to 85 at%Co and that the BCC + FCC two phase region extends from 85 at%Co to 90 at%Co. In contrast, the bulk phase diagram indicates that the FCC phase should be codeposited along with the BCC phase from ~75 at%Co to ~88 at%Co. In addition, the XRD results did not show the presence of the ordered CsCl phase near the 50 at%Co composition. These results show that the binary phase diagram is not necessarily a reliable method of predicting the phase structures of electrodeposited thin-films.

The properties of various electrodeposited magnetic thin-films alloys were compared by Myung et al. [Myung01]. Their experiments failed to produce iron-cobalt deposits composed of both the BCC and FCC phases. They detected only the FCC phase deposited at compositions above ~16 wt%Fe and only the BCC phase below ~16 wt%Fe. Deposits composed of the FCC phase tended to have larger grain sizes (~250 nm). The grain sizes of BCC deposits were ~50nm near the ~16 wt%Fe phase boundary, however, the grain size increased as the iron content of the deposits was increased. At its highest value, the plated iron-cobalt layers showed corrosion resistances an order of magnitude lower than cobalt-nickel and iron-nickel alloys. The corrosion resistance could be greatly improved by the addition of nickel to the alloy. Only a slight improvement was detected through the addition of boron. All the iron-cobalt deposits produced by the group were highly stressed and had a tendency to form cracks.

Osaka et al. [Osaka03] theorized that previous attempts to produce films with high saturation flux densities were impeded by the incorporation of  $\text{Fe}(\text{OH})_3$  precipitates in the deposits. The low solubility of  $\text{Fe}(\text{OH})_3$  means that it is easily precipitated out in the slightly higher pH region next to the cathode. Since the iron ions were added to the plating solution as a iron(II) salt, the presence of  $\text{Fe}(\text{OH})_3$  indicates that the oxidation of iron(II) to iron(III) cations at the anode during the

electroplating process occurs. This was confirmed by assays for iron(II) and iron(III) performed by the group on the plating solution both before and after it was used. The assay showed that the iron(III)/(iron(II) + iron(III)) ratio increased from 0.5 to 3.11 after the solution was used. In an effort to prevent the formation of iron(III) cations, two methods were employed. The first method involved the addition of trimethylamineborane (TMAB) to the plating solution in order to suppress iron(III) formation. This method was found to substantially increase the saturation flux densities of the deposits from 2.0T to 2.3T; it, however, fell short of the 2.4T goal. The second method involved the physical separation of the anode from the plating solution by using a dual electroplating cell. In this configuration, the cathode was immersed in the plating solution and was electrically connected to the anode, which was immersed in a separate solution, via a salt bridge. Using this method the group was able to achieve the desired magnetic saturation flux density of 2.4T. These films were further processed by magnetic annealing, which showed that the coercivities of the deposits could be reduced from 15Oe to as low as 8Oe by annealing within the 350-400°C temperature range for 1 h using 500Oe of applied magnetic field. Further research allowed the group to reduce the coercivity of the deposits even further, to ~6Oe, using pulsed electrodeposition [Osaka07].

Shou et al. [Shao03] successfully plated high-quality, crack-free iron-cobalt deposits from a sulfamate-based plating solution. These deposits maintained their integrity even when plated up to 100µm thick. They found that addition of vanadium to the deposits significantly reduced cracking in the films, even though the element was present in amounts too small to detect (<0.1 at%) using wavelength dispersive spectroscopy (WDS). These deposits had an average grain size of ~200nm. The layers had magnetic properties comparable to those of the bulk alloy, although the permeability of the films was slightly reduced by the presence of vanadium.

Xu et al. [Xu01] investigated the effect of plating conditions on the deposition of iron-cobalt thin films with composition between 47-67 at%Fe from an additive-free sulphate-based plating solution. Initial experiments conducted at a

pH of 2.9 and using a current density of  $7 \text{ mA/cm}^2$  produced deposits that were dark in colour and developed cracks after annealing at  $240^\circ\text{C}$  for 2 hours. Additionally the surfaces of these deposits were rough with large nodules on their surfaces. The hard axis coercivities for these deposits varied between 2.6-5.8Oe and the highest  $B_s$  value that was obtained was 2.14T, which is significantly lower than the 2.4T value given for the bulk alloy. The poor morphological and magnetic properties of these films were attributed to the incorporation of oxygen into the films; this was verified using x-ray photoelectron spectroscopy (XPS) which showed that 10 at% oxygen was present in the films. The oxygen content of these films was lowered to 3.5 at% by decreasing the solution pH to 2.6 and increasing the current density to  $21 \text{ mA/cm}^2$ . These steps prevented the formation of nodules and increased the saturation flux density to 2.18T, but also led to the formation of pores on the deposits surface, likely due to hydrogen evolution. Porosity was reduced through the use of pulsed plating.

Building on the work previously described, Bonhôte et al. [Bonhôte02, Bonhôte04] added acetic acid to their plating solution as a means of complexing iron(II) ions and reducing the amount of oxygen incorporated into the deposits. An organic sulphur-bearing additive (SBA) was also added as a replacement for saccharine which was used by Xu et al. [Xu01]. By using these reagents the amount of incorporated oxygen was reduced to  $\sim 0.1$  at%. As a result, the deposits that were produced had saturation flux densities between 2.35-2.45T which is consistent with the bulk values expected from these alloys. The group found that the saturation magnetization and magnetostriction of the films were primarily a function of the deposit composition, and were largely unaffected by changes to the bath temperature. Increasing the bath temperature, however, did lead to increases in the deposits' coercivities and decreases to their internal stresses and electrical resistivities. These effects were attributed by the group to increases in deposit grain sizes as the temperature was increased. The coercivities of the deposits were found to improve as the cobalt content of the films increased. This again was attributed to an increase in grain size. Increasing the cobalt content, however, also led to increased stress in the deposits. Magnetically annealing the



deposits at 200°C was found by the group to improve film coercivity.

The effects of magnetic annealing on the stress and magnetic properties of 40at%Co iron-cobalt thin-films were studied by Sun et al. [Sun05]. Their work indicates that stress relief through magnetic annealing was dependent primarily on the temperature and secondarily on the annealing time. Annealing of the samples at 225°C led to an increase in film stress, however, increasing the temperature to 255 °C significantly reduced this stress. A decrease in resistivity was observed in the deposits annealed at high temperatures, which was attributed to the reduction of defect density in the deposits as well as to a possible increase in grain size. No significant changes in film stress were observed when the deposits were annealed for more than 5 hrs. Magnetic annealing along the easy axis was found to significantly improve the coercivities of the films along both the easy and hard axis. Annealing with a magnetic field applied along the hard axis, however, switched the direction of easy and hard axes. This effect could be reversed again by re-annealing the deposits along their new hard axis. Magnetic annealing also improved the saturation magnetization of the films by a small amount (2%).

Many iron-cobalt plating solutions suffer from very short useful plating lives due to their tendency to form iron-hydroxide precipitates. The stability of these plating solutions can be improved by lowering their pH (typically 2.0-3.0) through acid additions. This, however, tends to produce voids in the deposits due to hydrogen evolution and iron-cobalt electroplating solutions often still have long term stability issues [Liu03]. Additives are often introduced to plating solutions to prevent the formation of hydroxide precipitates. Zhang et al. [Zhang07] attempted to optimize the plating parameters of a tri-basic ammonium citrate stabilized plating solution. The incorporation of ammonium citrate was shown to prevent the formation of hydroxide precipitates and allowed the plating solution to be used at its natural pH. The group also found that the addition of ammonium citrate significantly reduced the coercivity of the deposits from 22 Oe to ~10 Oe when present in low concentrations (2-20 g/L). This was attributed to stress relief effects of the ammonium citrate. At higher concentrations (> 50g/L) ammonium citrate was found to be very detrimental to deposit coercivity. Increasing the

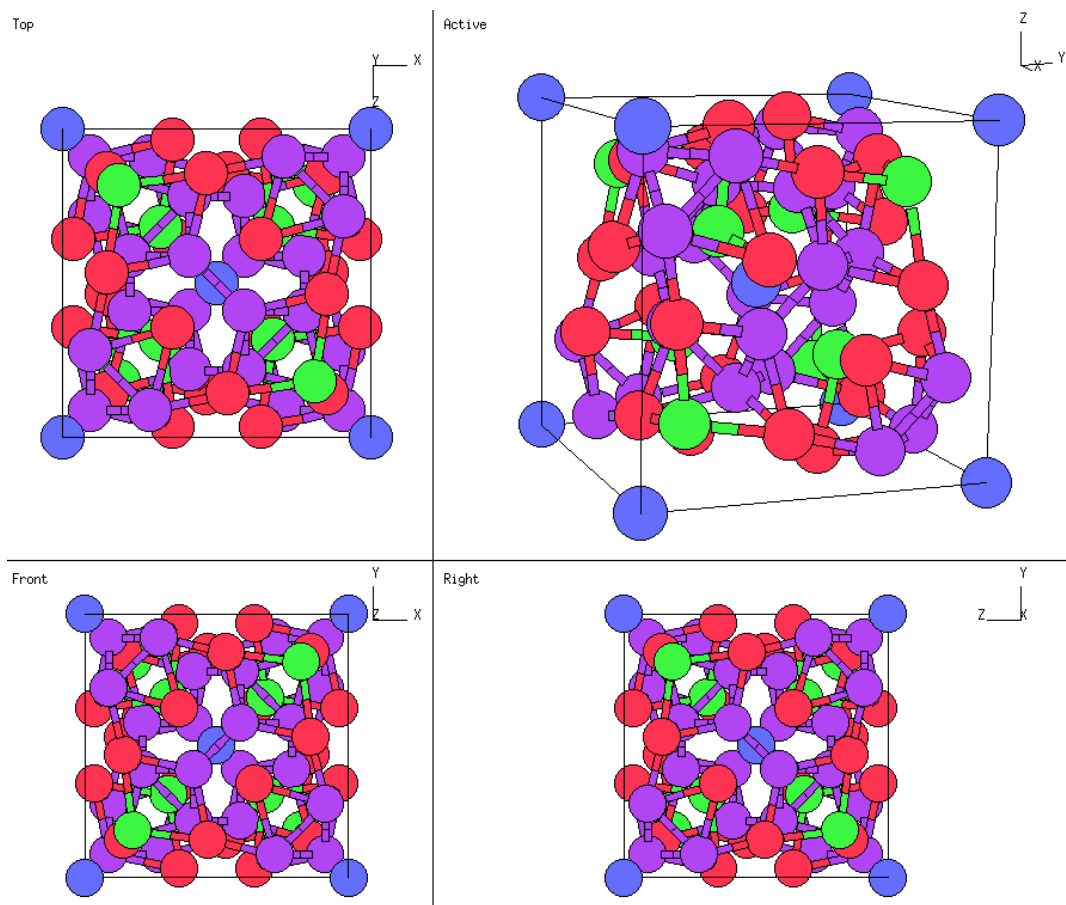
current density appears to greatly improve coercivities of deposits up to 15 mA/cm<sup>2</sup>. As current density is increased further the coercivity continues to improve but at a much slower rate. This effect was attributed to the tendency for small grains to be produced when high current densities are used. Plating temperature was found to have a linear relationship with coercivity, with higher temperatures leading to higher coercivities. X-ray diffraction analysis indicated that the FCC phase was formed at all compositions between 29 and 69 at%Fe. The BCC phase formed only in deposits with compositions between 50-69 at%Fe. These results disagree with the iron-cobalt phase diagram, which shows that the BCC structure should predominate and the FCC structure should only be stable at high Co compositions, indicating that the electroplated system strays far from equilibrium conditions. The lowest coercivities obtained were observed between 35-40 at%Fe, which coincides with the region where the FCC and BCC iron-cobalt phases were codeposited. Transmission electron microscopy (TEM) analysis showed that the grain size in this region is ~10-20nm.

Zhou et al. [Zhou09] examined the effects of plating temperature and solution composition on iron-cobalt deposits plated from a dibasic ammonium citrate stabilized plating solution. The group showed that the anomalous deposition of iron during the electrodeposition of iron-cobalt deposits decreased when higher plating temperatures and cobalt-rich plating solutions were used. When plated at room temperature, it was found that the BCC phase was the only phase plated up to 78 at%Co, at higher cobalt compositions the HCP phase dominated. Unlike Zhang, who found that FCC was deposited over most of the composition range [Zhang07], the FCC phase was only found in deposits of pure cobalt and even then was codeposited along with the equilibrium HCP phase. At elevated temperatures, a metastable phase isostructural to  $\alpha$ -Mn was deposited. The  $\alpha$ -Mn type phase has previously been formed in the iron-cobalt alloys through precipitation reactions [Pourroy96, Pourroy98, Pourroy99, Jay01, Pourroy02], vapour deposition [Jay01] and in iron-chromium and iron-nickel-chromium alloys through magnetron sputtering [Simmonds96, Specht04, Specht05]. The  $\alpha$ -Mn type phase had not previously been reported in electrodeposited films. The phase was

detected in films plated at 40°C at compositions from 68 to 78 at%Co, and from 36 to 85 at%Co when plated a 60°C.

The  $\alpha$ -Mn type phase is a metastable phase that was initially identified as a product of precipitation reactions involving the addition of iron and cobalt chloride salts to concentrated KOH solutions refluxed at temperatures between 120-140°C [Pourroy96, Pourroy98, Pourroy99, Jay01, Pourroy02]. The phase was subsequently also produced through vapour codeposition of iron and cobalt under ultra-high vacuum conditions [Jay01]. Iron-chromium and iron-chromium-nickel alloys have been deposited as similar phases through magnetron sputtering [Simmonds96, Specht04, Specht05]. The  $\alpha$ -Mn unit cell is shown in Figure 2-28.

The  $\alpha$ -Mn phase (space group:  $I\bar{4}3m$ ) has a very complicated cubic unit cell composed of 58 atoms. The lattice parameter for the  $\text{Co}_{78}\text{Fe}_{22}$  alloy, which was produced by Jay et al. through precipitation reactions, was estimated by the group to be  $\sim 0.8738\text{nm}$  [Jay01]. Annealing experiments have shown that the  $\alpha$ -Mn type phase will transform to the stable BCC phase when annealed at temperatures above 160°C [Jay01]. In iron-nickel-chromium alloys with a similar structure the  $\alpha$ -Mn type phase is associated with a small grain size and is thought to be stabilized by the incorporation of large impurities and residual stresses in the deposits [Simmonds96, Specht05].



**Figure 2-28:**  $\alpha$ -Mn unit cell with equivalent lattice positions identified by colour [Crystal04].

In her thesis work Zhou [Zhou09-2] subsequently found that the use of tribasic ammonium citrate (natural pH = 4.7) as a stabilizing agent promoted the formation of metastable phases, the  $\alpha$ -Mn type phase included, at lower temperatures. Room temperature plating, using the tribasic ammonium citrate stabilized plating solutions, produced deposits composed of both the BCC and  $\alpha$ -Mn type phases at compositions between 65 at%Co and 76 at%Co, and only the  $\alpha$ -Mn type phase at higher temperatures. Deposits plated at 40°C had exclusively  $\alpha$ -Mn type phase structures at compositions greater than 67 at%Co. At lower cobalt compositions, a second metastable HCP phase was codeposited with the BCC phase at 39 at%Co, and with the BCC and  $\alpha$ -Mn type phase at 53 at%Co. In deposits plated at 60°C, a phase that Zhou [Zhou09-2] identified as a dHCP (double HCP, space group: P6/mmm) phase was codeposited along with other

phases at compositions between 37 at%Co and 81 at%Co. It was codeposited along with the BCC phase between 37 at%Co and 56 at%Co, and the  $\alpha$ -Mn type phase at compositions between 56 at%Co and 81 at%Co. At higher cobalt compositions the  $\alpha$ -Mn type phase was the only phase deposited. The dHCP phase had previously only been identified as a product of an allotropic transformation of pure iron at high temperatures and pressures [Saxena95].

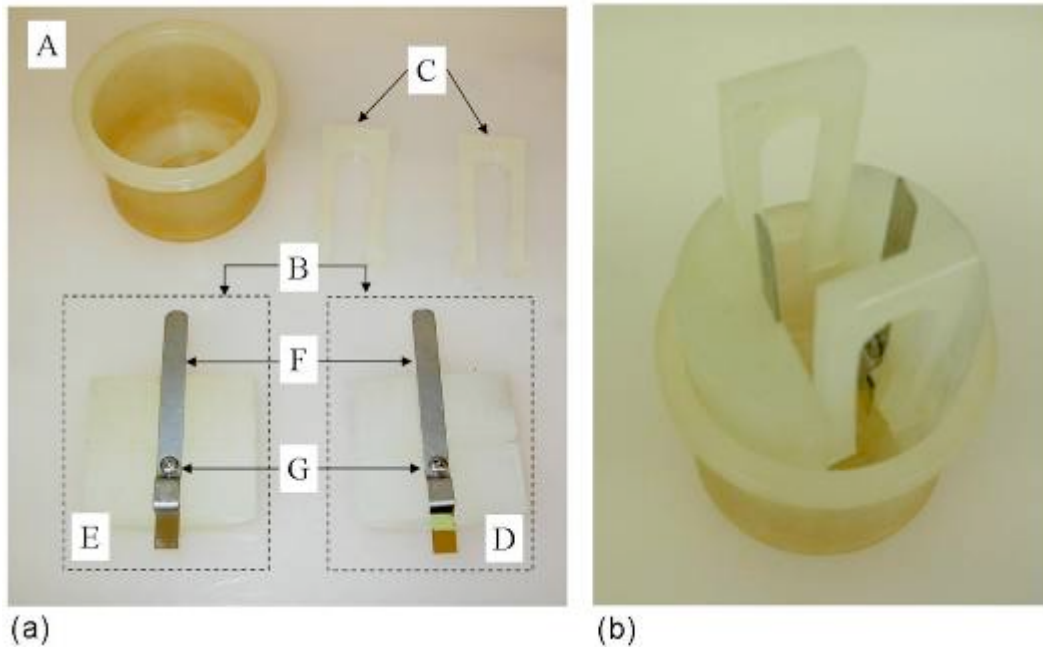
## **2.5 Objectives of the research work**

The intended purpose of this thesis research is to characterize iron-cobalt deposits, in terms of their morphological, compositional and magnetic properties, obtained using a dibasic ammonium citrate stabilized plating solution. The effects of plating parameters such as plating temperature, current density and pH are analysed and the suitability of the deposits as potential write head materials is evaluated. The stability of the plating solution itself is also analysed to judge its suitability for electrodeposition after extended periods of storage and to identify parameters that affect the solution stability.

## Chapter 3 Experimental Procedure

### 3.1 Electroplating cell

Electrodeposition was carried out in a simple polypropylene electroplating cell. The electroplating cell is shown in Figure 3-1.



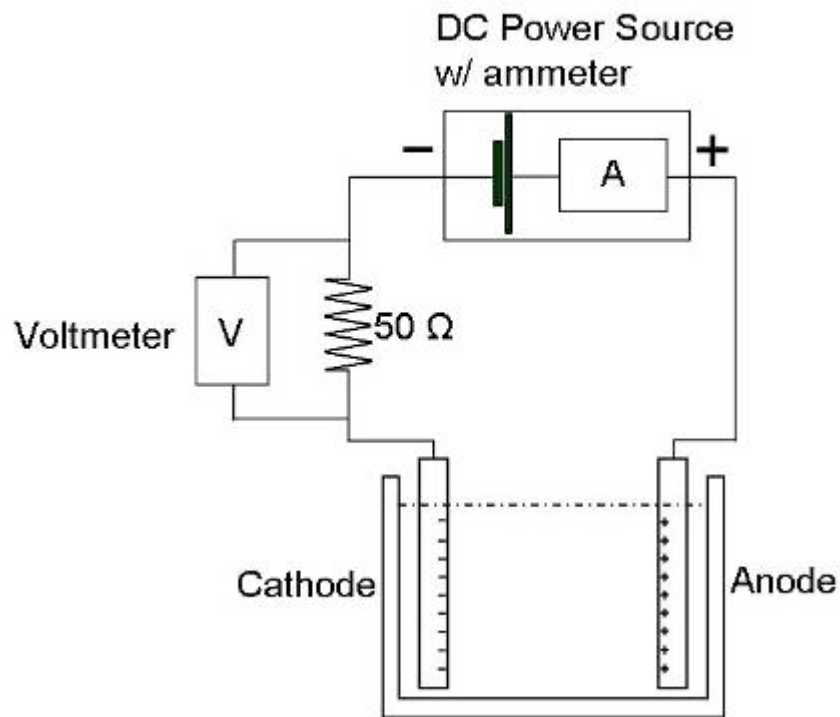
**Figure 3-1:** Photograph of polypropylene electroplating cell: (a) Labeled sections of cell showing: the cylindrical vessel (A), the sample holders (B), the spacers (C), the cathode (D), the anode (E), the sample clasps (F) and the tightening screws (G). (b) The assembled electroplating cell.

The cell consisted of a 150 mL cylindrical vessel (A), which contained the electroplating solution, and two sample holders (B) that were held flush with the container's walls using spacers (C). The anode and cathode were mounted vertically in the electroplating cell at a fixed distance of 2.5 cm apart. The cathode (D) consisted of a diced section of a titanium (100nm)/gold (500nm) metallized silicon wafer. Photoresist was applied to the cathode's surface to restrict the plating area to a rectangular region approximately 0.64-0.8 cm<sup>2</sup>. A diced section

of a titanium (75nm)/platinum (200nm) metallized silicon wafer was used as the anode (E). The metals were sputter deposited onto the silicon substrates; the titanium acting as the adhesion layer upon which the gold or platinum was deposited. The wafers were diced using a Disco dicing saw (Model DAD 321). Prior to dicing, the surfaces of the gold metalized wafers were first protected using photoresist. The photoresist was removed by rinsing with acetone followed by ethanol prior to being used. No photoresist was applied to the surfaces of the platinum wafers prior to dicing. The electrodes were fastened to the sample holders using electrically conductive metal clasps (F) that could be tightened or loosened using the screws (G) which held the clasps to the sample holders.

Electrical wire leads were used to connect the sample clasps to the power supply. A 50  $\Omega$  standard resistor was placed in series with the plating bath across which a Tektronic oscilloscope (Model TDS 1002) was connected and used to monitor the waveform in the circuit and to corroborate the current output of the power supply. Current was supplied using a Dynatronix, Inc. (Model DuPR10-1-.3) power supply. A schematic of the electroplating circuit is shown in Figure 3-2. When heating of the solution was required, the electroplating cell was placed in a Fisher Scientific International Inc. (Model Isotemp 202) water bath. An alcohol thermometer was used to measure the solution temperature.





**Figure 3-2:** Schematic representation of the electroplating circuit.

### 3.1.1 Standard electroplating solution and conditions

The composition of the standard electroplating solution that was used is shown in Table 3-1. For each deposit, 40 mL of fresh solution was used, and the pH of the solution was not adjusted from its natural value of  $\sim 3.5$ . The average current density for all experiments was  $15 \text{ mA/cm}^2$ . The current was pulsed with a duty cycle of 6 ms on-time followed by 4 ms off-time. All samples were plated for 9 minutes under these conditions and then immediately removed from the plating solution; this resulted in deposits  $\sim 1.7 \text{ }\mu\text{m}$  thick at their centres. The parameters were chosen based on previous work where the same parameters gave optimal soft magnetic properties for a similar solution [Zhang05]. When heating was required, the solution was added to the plating cell which was then placed in the hot water

bath. The power supply was not activated until the plating solution had reached the desired temperature. Unless otherwise specified, the results obtained in this work were obtained using the plating solution and parameters described above.

**Table 3-1:** Composition of standard electroplating solution.

<b>Reagent</b>	<b>Concentration (mol/L)</b>
CoSO <sub>4</sub> • 7H <sub>2</sub> O	0.12
FeSO <sub>4</sub> • 7H <sub>2</sub> O	0.048
H <sub>3</sub> BO <sub>4</sub>	0.4
Sodium Lauryl Sulphate	0.01 g/L
Dibasic Ammonium Citrate	4.65 g/L

### 3.1.1.1 Variations on plating solution and parameters

Variations on the standard electroplating solution were used in several experiments. To determine the effects of dibasic ammonium citrate on deposit structure, it was omitted from the plating solution for some experiments (Section 4.2.1.3.1). Also, solutions not containing either the CoSO<sub>4</sub> • 7H<sub>2</sub>O or the FeSO<sub>4</sub> • 7H<sub>2</sub>O were used in evaluating the stability of the standard plating solution (Section 4.1). In Section 4.1.1.1, FeSO<sub>4</sub> • 7H<sub>2</sub>O was replaced by an equal molar amount of FeNH<sub>4</sub>(SO<sub>2</sub>)<sub>2</sub>•12H<sub>2</sub>O. The average current density was also adjusted for some experiments (Section 4.2.2).

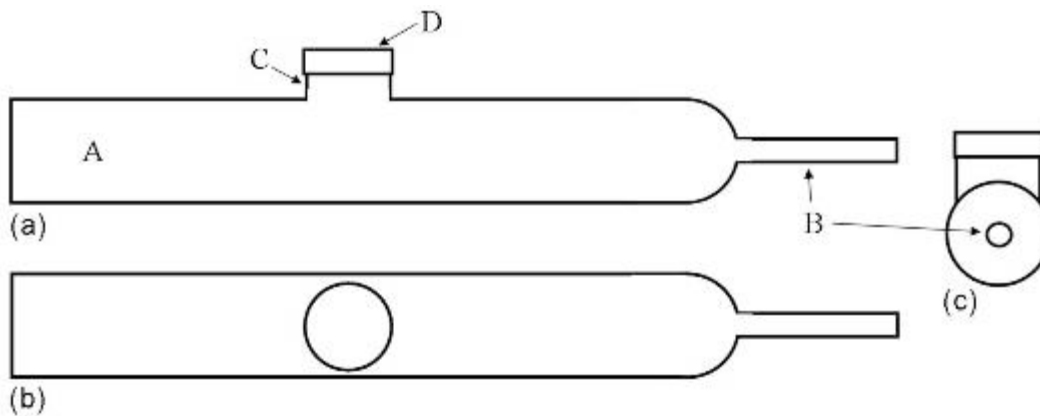
Some experiments required the adjustment of the solution pH. When adjustments to pH were required, they were done by making small additions of a dilute H<sub>2</sub>SO<sub>4</sub> solution. The pH values of the solutions were measured using an Accumet Basic pH meter (Model AB15).

## 3.2 Magnetic Annealing

### 3.2.1 Annealing furnace and sample holder

Magnetic annealing was done in a custom designed quartz tube furnace. The tube furnace was composed of two fundamental components: the tube portion of the furnace, which contained the gas and retained the heat during annealing, and the heating platform, which supported and heated the sample.

A schematic of the tube section of the furnace is shown in Figure 3-3.

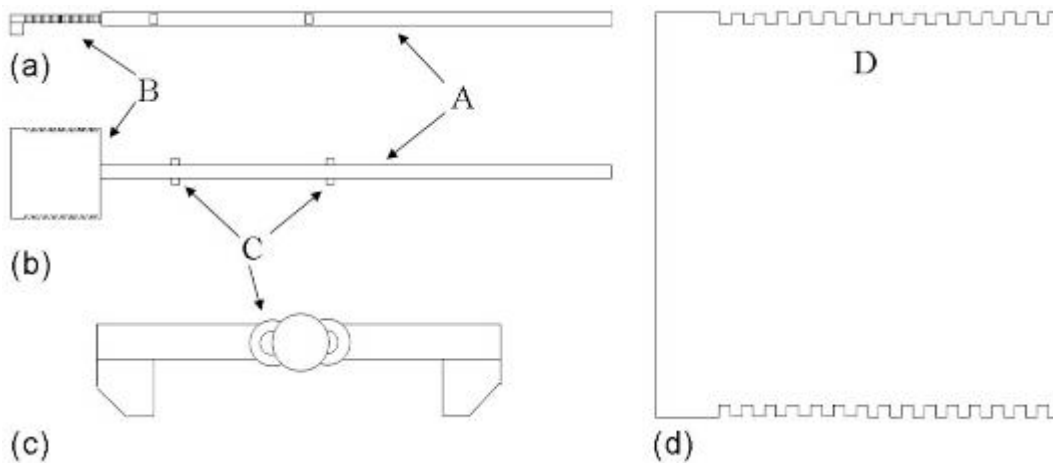


**Figure 3-3:** Schematic representation of the tube section of the tube furnace: a) side view, (b) top view, (c) view along centre axis. Labels in the figure represent: the quartz tube (A), the fluted outlet (B), the top center opening (C), and the top center opening lid (D).

The tube portion of the furnace had an outer diameter of 4.5cm and was 29.5 cm long (not including the fluted outlet). It had three openings: an inlet through which the sample and heating platform were introduced to the tube (A), a fluted outlet (B) and a small opening in the centre of the top of the tube (C). During operation, the inlet of the tube furnace was fitted with a rubber stopper through which electrical leads, a thermocouple, a tube to introduce gas to the furnace, and the long stem of the heating platform were passed. A Gilmont shielded industrial flow meter was used to measure and control the flow of gas to the furnace. Gas was removed from the furnace through the fluted outlet and was bubbled through

water held in an Erlenmeyer flask to ensure that the furnace was held at positive pressure relative to the atmosphere. After passing through the flask, the gas was expelled in a nearby fume hood. The short branching opening on the top of the tube furnace allowed for adjustments to the orientation of the sample to be made once it was placed in the furnace. The opening was sealed during operation using a quartz lid (D). To ensure that no gas escaped around the lid, vacuum grease was applied around the edge of the lid.

Heating of the sample was done inside the quartz tube using a quartz platform that was wrapped in nickel/chromium heating wire. The sample was placed on the platform in a copper sample holder and current was passed through the heating wire to heat the sample. This was necessary to allow the tube furnace to fit within the gap of the magnetic separator, traditionally used for the separation of magnetic minerals from slurries, that was used to generate the magnetic fields used for magnetic annealing. A schematic of the quartz heating platform is shown in Figure 3-4.

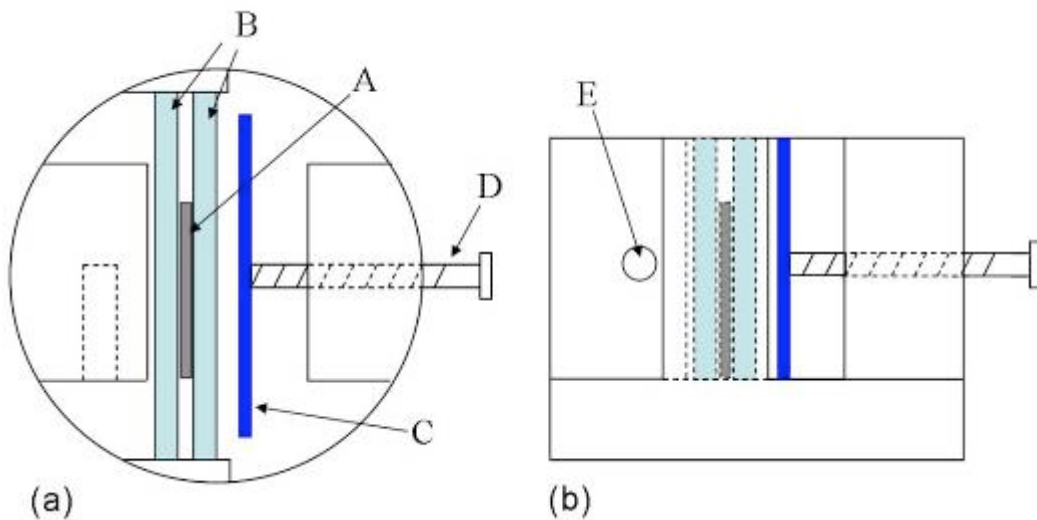


**Figure 3-4:** Schematic representation of quartz heating platform: a) side view of sample platform, (b) top view of sample platform, (c) magnified view along the stem towards the sample platform, (d) magnified view of sample platform. Labels in the figure represent: the heating platform stem (A), the sample platform (B), heating wire rings (C), and heating wire ridges (D).

The stem (A) of the sample platform (B) was passed through the stoppered inlet of the furnace tube, which provided support to the platform and ensured that the

sample holder was held level in the furnace. Small rings (C) on the sides of the platform stem helped separate the electrical wires leading to the platform during operation, preventing the wire from creating a short circuit. Small ridges (D) along the sides of the sample platform held the heating wire in place as it was wound around the sample platform and prevented the wires from touching during operation.

A copper sample holder was used to hold the electroplated samples perpendicular to the applied magnetic field. A schematic representation of the sample holder is shown in Figure 3-5.



**Figure 3-5:** Schematic representation of copper sample holder: a) top view and, (b) side view. Labels in the figure represent: the sample (A), aluminum nitride wafers (B), the copper plate (C), brass tightening screw (D), and the hole for the thermocouple (E).

The samples (A) were placed vertically in the sample holder's interior slit. Cut sections of thin aluminum nitride ceramic wafers (B) were placed on either side of the samples to prevent diffusion couples from forming between the sample holder and the deposits. The samples and aluminum nitrite wafer sections were then held vertically against the interior wall of the sample holder by pressing them with a thin copper plate (C) which was tightened using a brass screw (D). A non-magnetic type-E thermocouple was placed in a hole extending into the sample

holder (E), near the interior wall where the samples were held, to measure the annealing temperature. The thermocouple measurements were displayed using a Fluke digital thermometer (Model 54II). To prevent the copper sample holder from creating a short circuit in the heating wires below it, an aluminum nitride ceramic wafer was used to separate the sample holder from the sample platform.

Annealing temperature was controlled by adjusting the voltage through the heating wire using a Staco Energy (Type 3PN1010) autotransformer. The voltage was controlled manually using the autotransformer dial. Time and temperature were checked and recorded periodically throughout annealing. The magnetic field was applied using an Outokumpo wet magnetic separator (Model WHIMS 3x4L). When a magnetic field was required, the tube furnace was placed between the magnetic plates of the separator with the sample in its centre. The applied field was calibrated using an Alphalab D.C. gaussmeter.

### **3.2.2 Magnetic annealing parameters**

Prior to annealing, the edges of the deposits were cleaved off using a diamond scribe. This was done to exclude edge effects from the deposits. Annealing of the deposits was conducted under a reducing atmosphere of 5% H<sub>2</sub> with the balance N<sub>2</sub>. The reducing atmosphere helped to prevent the formation of oxides in the samples and the sample holder itself when annealing at high temperatures. The gas was passed through the furnace at a flow rate of ~10 cm<sup>3</sup>/s. The annealing temperatures were ~170°C, 225°C, and 390°C. The first two lower temperatures were chosen to show the effects of partial and full transformation of the  $\alpha$ -Mn type phase, which has a transformation temperature of ~160°C [Jay01]. The highest temperature was chosen because it is within that temperature range that has been shown to produce superior soft magnetic properties during annealing [Osaka03]. The deposits were heated to the desired temperature, over a 20 minute time interval, and held at temperature for 4 hours before furnace cooling to room temperature. This allowed enough time for substantial phase transformation to

occur in the deposits at lower temperatures. Also, longer annealing times were not shown to significantly affect magnetic properties [Sun05].

Three different applied magnetic field intensities were used during annealing: 0 Oe, 500 Oe and 2500 Oe. During magnetic annealing, the magnetic field was applied perpendicular to the deposit surface once the sample was brought to the desired temperature. The magnetic field was then maintained throughout the annealing times and after the furnace was turned off until the sample had cooled to less than 40°C.

### 3.3 Characterization and analysis

The stability of the iron-cobalt plating solutions was determined by measuring the solution pH and the light absorbance spectra of the solutions. The pH was measured using an Accumet Basic pH meter (Model AB15). The absorbance spectrum for the solutions was measured using a Jenway 6405 UV/Vis spectrophotometer. The absorbance spectrum for the solutions was measured for wavelengths of light between 300 nm and 600 nm with a step size of 1nm. The absorption baseline was initially calibrated using an optically transparent quartz cell containing deionized water. The cell was rinsed several times with deionized water between samples.

The phase structure of the deposits was determined using x-ray diffraction (XRD) and electron diffraction. XRD was done using a Rigaku Rotaflex thin film XRD system, with a rotating anode. An incident beam angle of  $2^\circ$  was used with a scanning rate of  $2^\circ$  per minute. Due to equipment problems, some experiments were conducted using a cobalt anode and others using a copper anode. For the cobalt anode, a voltage of 40 mV and 160 mA of current were used to produce the incident x-ray beam. For the copper anode, a voltage of 40mV and a current of 100mA were used. The identity of the anode was indicated in the pattern's top right corner. The XRD patterns were analysed using the Jade 5.0 XRD software. Electron diffraction patterns were obtained using a transmission electron microscope (TEM) as described below.

A Leica DM2500M optical microscope equipped with an Infinity 1 digital camera was used to obtain micrographs showing large scale morphological features on the deposits' surfaces, such as cracks. Higher magnification micrographs were taken in plan view and cross section orientations using a Hitachi S-2700 scanning electron microscope (SEM) equipped with a PGT (Princeton Gamma-Tech) IMIX digital imaging system, which was used for secondary electron (SE) imaging. Back-scattered (BSE) images were taken using a GW Electronics System 47 four quadrant solid state BSE detector. A PGT



PRISM IG (intrinsic germanium) detector allowed the SEM to be used to obtain energy dispersive x-ray (EDX) results. A JEOL 2010 transmission electron microscope (TEM) was used to obtain higher resolution cross-section images and electron diffraction patterns of the deposits. An accelerating voltage of 200kV and a calibrated camera length of 123 cm were used. Dark field (DF) images were taken using part of the most intense electron diffraction rings.

Thickness measurements were obtained using a Tencor AS-200 profilometer. Measurements were taken at 5 different, evenly spaced points across the deposit surface using the substrate as the reference point. The extreme edges of the deposits were excluded from average thickness calculations, because they showed excessive edge effects (severe cracking and very thick) and were cleaved off prior to annealing experiments.

Compositional analysis of the metallic elements in the deposits was done using EDX microanalysis. Due to the poor sensitivity of EDX system for light elements, the oxygen content of the deposits was determined using x-ray photoelectron spectroscopy (XPS). XPS measurements were taken using a Kratos Axis 165 XPS system. An aluminum x-ray source was used operating at 15 mA of current and an accelerating voltage of 14 kV. Prior to measurement, the surface of the deposits were sputtered with argon for 40 minutes using an accelerating voltage of 4 kV to remove any surface oxide films. XPS was also used for phase identification of oxide precipitates.

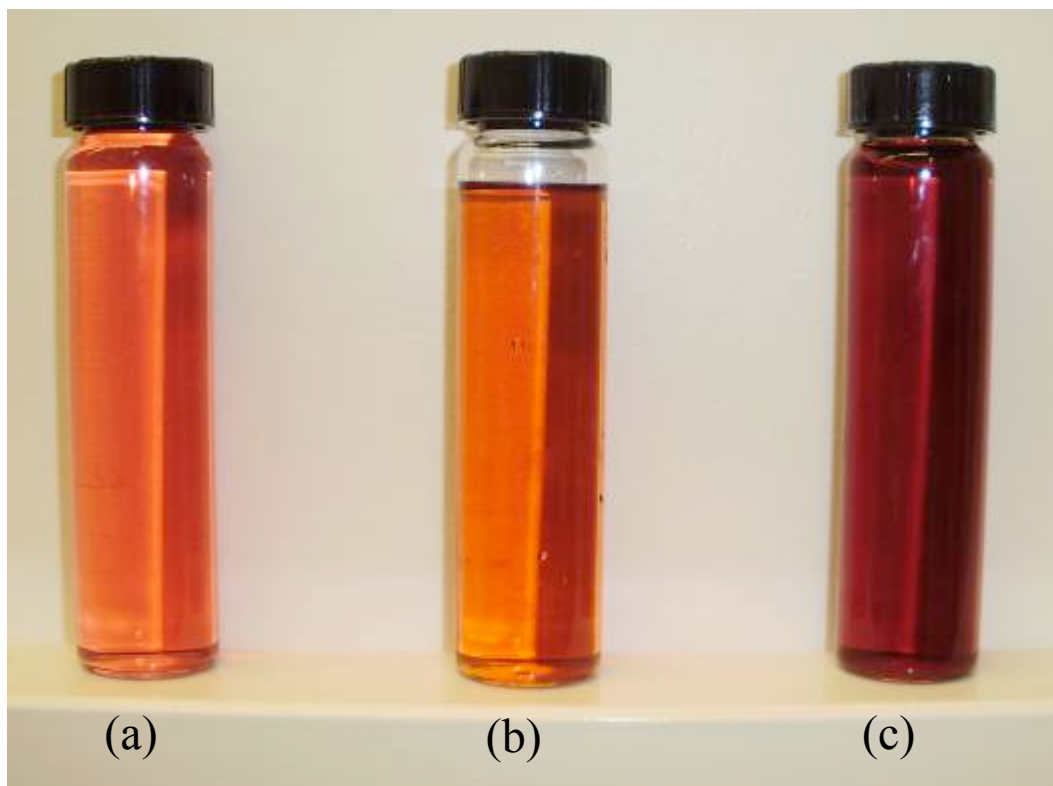
Magnetic measurements were obtained using a super quantum interference device (SQUID) magnetometer (Model MPMS XL-7). Measurements were taken at 300K. In order to determine the saturation magnetization flux densities of the deposits, accurate measurements of sample volume was required. The areas of the samples were obtained by taking low magnification images of the sample surfaces using a Zeiss MC63A photomicrograph camera. The surface area of the samples was then defined and integrated using the Adobe Photoshop 4.0 software. The thickness of the samples was determined using the Tencor AS-200 profileometer.

## **Chapter 4 Results and Discussion**

### **4.1 Stability of dibasic ammonium citrate plating solutions**

#### **4.1.1 Long term stability of dibasic ammonium citrate stabilized solutions**

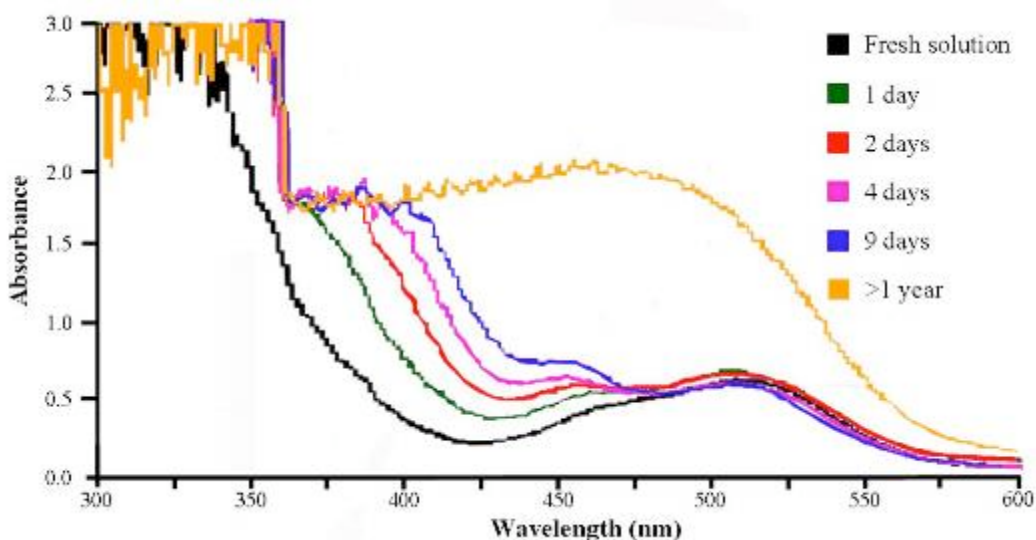
The addition of ammonium citrate was reported to greatly increase the stability of iron-cobalt plating solutions by complexing metal cations, particularly iron(II), and prevent them from forming hydroxide precipitates [Zhang04, Zhang07]. Experiments using the standard plating solution (Table 3-1) showed that the presence of ammonium citrate does indeed prevent the immediate formation of precipitates from the solution. Plating solutions, without ammonium citrate as a stabilizer, at their natural pH, however, formed visible precipitates after only 1 hour. Under careful observation, however, a detectable colour change from the original pink to an orange hue was observed when the dibasic ammonium citrate stabilized plating solutions were left unused and exposed to air for several days. Although faint at first, the colour change was detectable visually after only one day of storage and was first noticeable at the solution/atmosphere interface. This colour change progressed deeper into the solution as the aging time of the solution was extended. After several months, the solution turned to a deep red colour and became murky, indicating the formation of very fine, mostly suspended, precipitates. A photograph comparing the fresh standard plating solution to solutions which had been aged for various lengths of time is shown in Figure 4-1. UV-visible light absorbance spectroscopy verified the colour change as the solution was left for extended periods of time. Figure 4-2 shows the absorbance spectra for the iron-cobalt plating solution, with dibasic ammonium citrate, after various time intervals.



**Figure 4-1:** Standard iron-cobalt plating solutions, which were exposed to air, in both fresh and aged forms: (a) fresh solution, (b) aged 14 days and (c) aged for more than one year.

The absorption spectrum for the fresh solution shows that light is strongly absorbed at wavelengths from 300nm to ~340nm. At wavelengths higher than ~340nm, the solution absorbs increasingly less light and reaches a local minimum at ~425nm. There is a second range of increased absorbance between ~425nm and ~550nm, with a peak at ~515nm; above this value the absorbance by the solution is negligible. Moderate aging of the solution has the effect of increasing the lower wavelength range where the solution strongly absorbs light from ~300-340nm to ~300-360nm. This effect was observed after only 1 day of aging and did not progress as the solution was aged for longer times. In addition, instead of the solution gradually absorbing less light at wavelengths larger than the range for high absorbance, aged solutions showed a sharp decrease in absorbance at ~360nm but the absorbance leveled off at a value roughly 60% of the absorbance scale maximum before continuing to fall. The width of this second level of

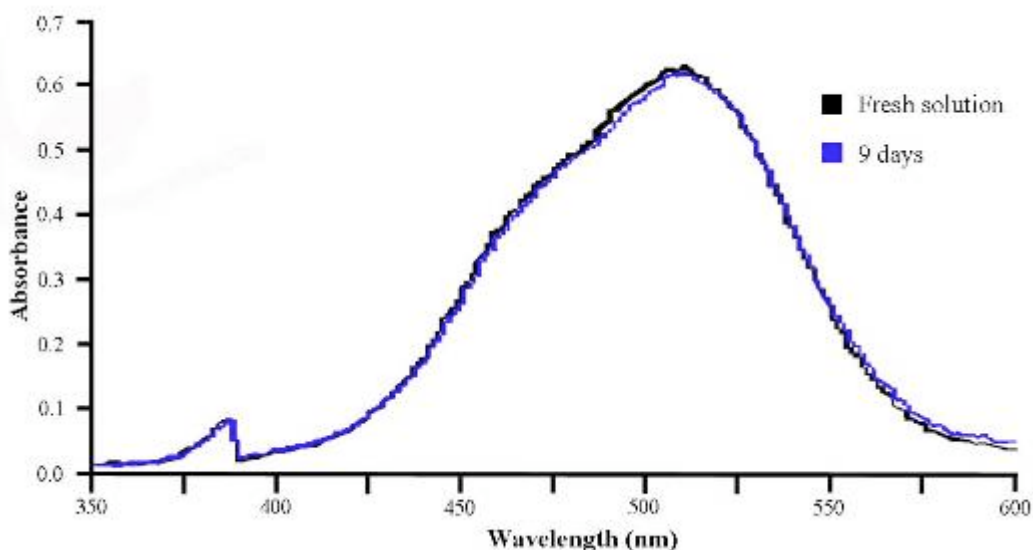
absorption range was related to the aging time of the solution, with older solutions absorbing a larger range of wavelengths at this level before continuing to drop. As the solution was aged a new peak at 450nm was produced, the height of which increased with aging time. The peak at ~515nm, which was observed in the fresh solution, did not change upon aging in solutions which were aged for up to 9 days. When aged for several months the level region, which started at ~360nm, was greatly extended to higher wavelengths. This effect was strongly associated with the appearance of precipitates in the solution.



**Figure 4-2:** UV-visible absorption spectra of iron-cobalt plating solution prepared with dibasic ammonium citrate: fresh solution and aged.

The influence of the individual cationic species, i.e., cobalt(II) and iron(II), on the absorption spectra of the iron-cobalt plating solution was evaluated by analyzing separate solutions containing only one of the two cationic species. The UV-visible light spectra from a solution containing only cobalt cations is shown in Figure 4-3. Unlike the iron-cobalt plating solution, the solution containing only cobalt cations showed very little absorption of low wavelength light. A small peak at ~390nm is observable but this is negligible in comparison to the absorption at this wavelength in the iron-cobalt plating solution. The only major peak over the tested range has a maximum at ~515nm which corresponds

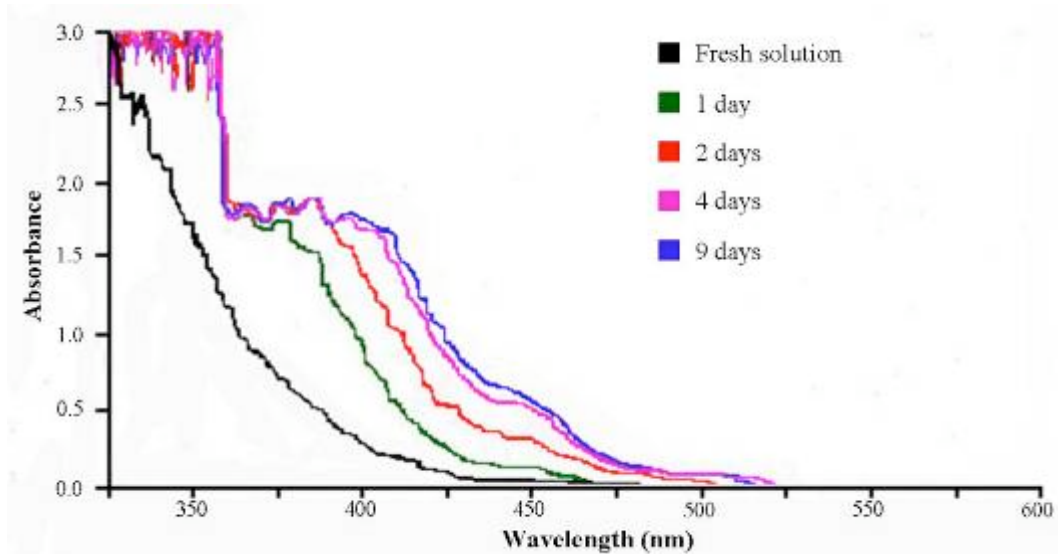
with the high wavelength peak observed in the iron-cobalt plating solution. There was no change in absorption spectra as the solution was aged. Visual examination of the solutions also showed no change in the solution's colour after aging.



**Figure 4-3:** UV-visible absorption spectra of solution containing only cobalt cations: fresh solution and aged for 9 days.

The absorption spectra for solutions containing only iron cations are shown in Figure 4-4. The absorption spectra for the iron solution show all the aging characteristics observed in the iron-cobalt plating solution. The fresh iron solution absorbs low wavelength light strongly, but at wavelengths greater than  $\sim 325\text{nm}$  the absorbance gradually decreases until almost no light is absorbed past  $\sim 450\text{nm}$ . After aging for 1 day or more, the lower range over which light is intensely absorbed extends to  $\sim 360\text{nm}$ . The spectrum also shows an abrupt drop in absorbance past  $\sim 360\text{nm}$  to  $\sim 60\%$  of the maximum absorption scale. The spectrum then levels off before continuing to fall with increasing wavelength. This level region extends to higher wavelengths as the solution is aged. A small peak at  $\sim 450\text{nm}$  also forms. All the aging effects are seen in the iron-cobalt solution upon aging. Visual inspection of the iron solution after aging corroborates the colour change, as the solution went from a pale yellow to a darker yellow/green. These results indicate that the colour change in the iron-

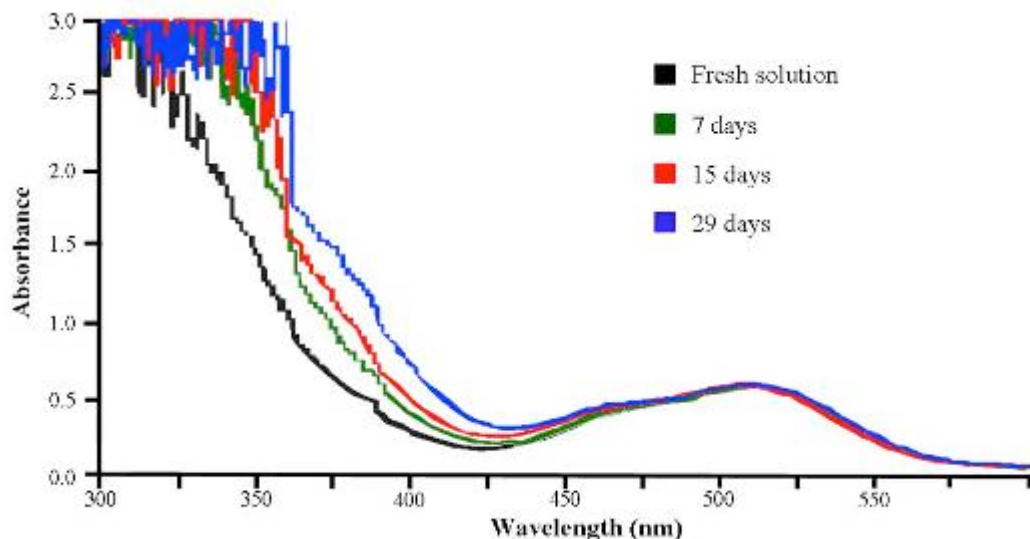
cobalt solution can be attributed to a change in iron species in solution over time.



**Figure 4-4:** UV-visible absorption spectra of solution containing only iron cations: fresh solution and aged for up to 9 days.

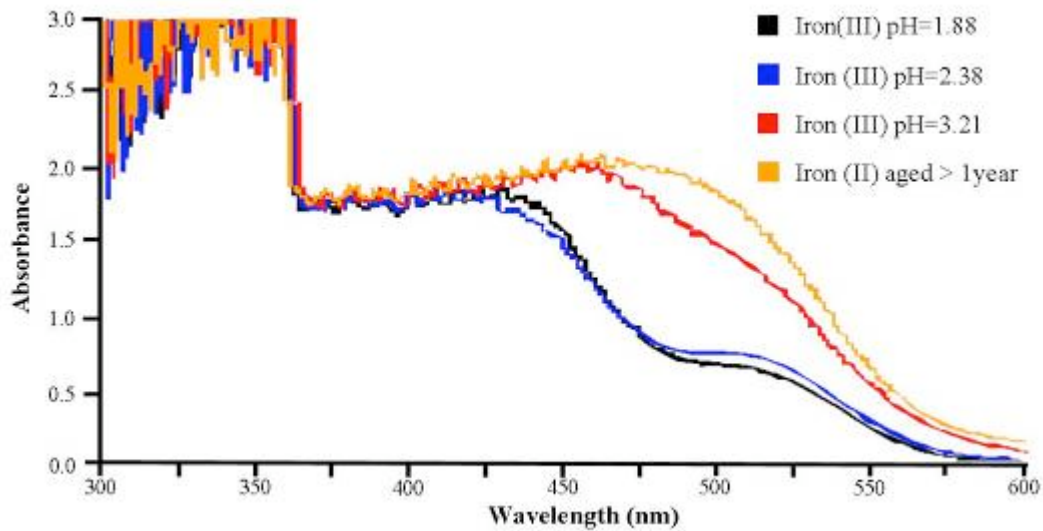
#### 4.1.1.1 Effects of dissolved oxygen on solution stability

Since the colour change appears to initiate at the solution-air interface, it seems likely that the reaction is an oxidation reaction caused by dissolved oxygen. UV-visible absorption spectra for iron-cobalt solutions, which were stored in full sealed containers and not exposed to air, are shown in Figure 4-5. It shows that the exclusion of contact between the iron-cobalt plating solution and air greatly limits both the extent and rate of reaction in the solution. After 29 days of storage, the solution only experienced a change comparable to a solution stored for 1 day when exposed to the atmosphere. The small change in the spectra in Figure 4-5 can likely be attributed to dissolved oxygen, which is incorporated into the solution prior to storage.



**Figure 4-5:** UV-visible absorption spectra of iron-cobalt solution sealed from atmosphere and aged for up to 29 days.

When an iron-cobalt solution containing iron(III) cations was produced by replacing  $\text{FeSO}_4 \cdot 7\text{H}_2\text{O}$  with  $\text{FeNH}_4(\text{SO}_2)_2 \cdot 12\text{H}_2\text{O}$ , the solution (natural pH = 1.88) displayed an orange hue very similar to the colour that the iron(II)-cobalt plating solution showed after moderate aging. The absorption spectra for a fresh iron(III)-cobalt solution at various adjusted pH values is shown in Figure 4-6. From Figure 4-6, it can be seen that the iron(III)-cobalt solution has absorption spectra characteristics very similar to that seen in the oxidized iron(II)-cobalt plating solution. When the pH was increased in order to better approximate the pH of the iron(II)-cobalt plating solution, the solution obtained a deep red colour and precipitates became apparent. The spectra in Figure 4-6 closely resemble the spectra for the iron(II)-cobalt plating solution after prolonged aging and the appearance of precipitates. These results indicate that the solution colour change is likely due to a valence change in the plating solution from iron(II) to iron(III) due to the presence of dissolved oxygen. The valence change is then followed by the slow formation of an iron-based precipitate.

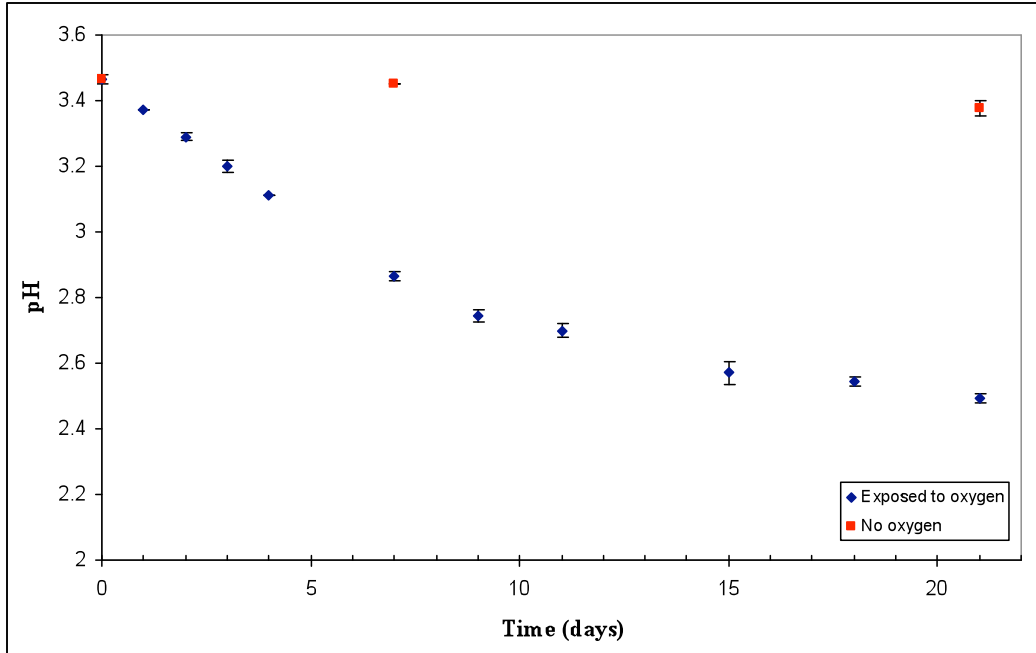


**Figure 4-6:** UV-visible absorption spectra of iron(III)-cobalt solution at various pH values compared with the spectrum of a heavily oxidized iron(II)-cobalt solution (aged for >1 year).

#### 4.1.1.2 Effects of aging on solution pH

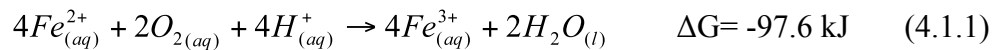
The pH of iron(II)-cobalt plating solutions exposed to and isolated from atmospheric oxygen, as a function of the age of the solution, is shown in Figure 4-7.



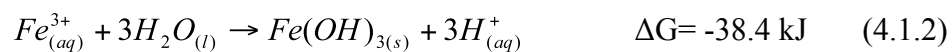


**Figure 4-7:** The pH change in iron-cobalt plating solutions over time.

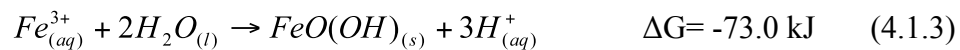
The gradual decrease in pH of the solutions exposed to atmospheric oxygen indicates that the formation of hydrogen ions is associated with the colour change of the solution. A likely mechanism for the reaction is as follows:



followed by:



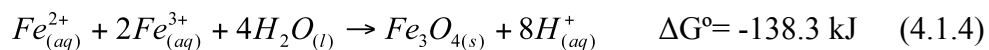
and/or



The Gibbs free energy calculations for these reactions are shown in Appendix A. Since the activities of iron(II) and iron(III) are not known, Appendix A assumes a pH of 3.5 and standard conditions for all species other than the hydrogen ions. These mechanisms are commonly observed in acidic iron(II) solutions when adequate oxygen is available [Bradford02, Lottermoser07]. In addition, reactions such as these have been documented in similar iron-cobalt plating solutions [Osaka03]. The Gibbs free energy calculations show that at a pH of 3.5 the

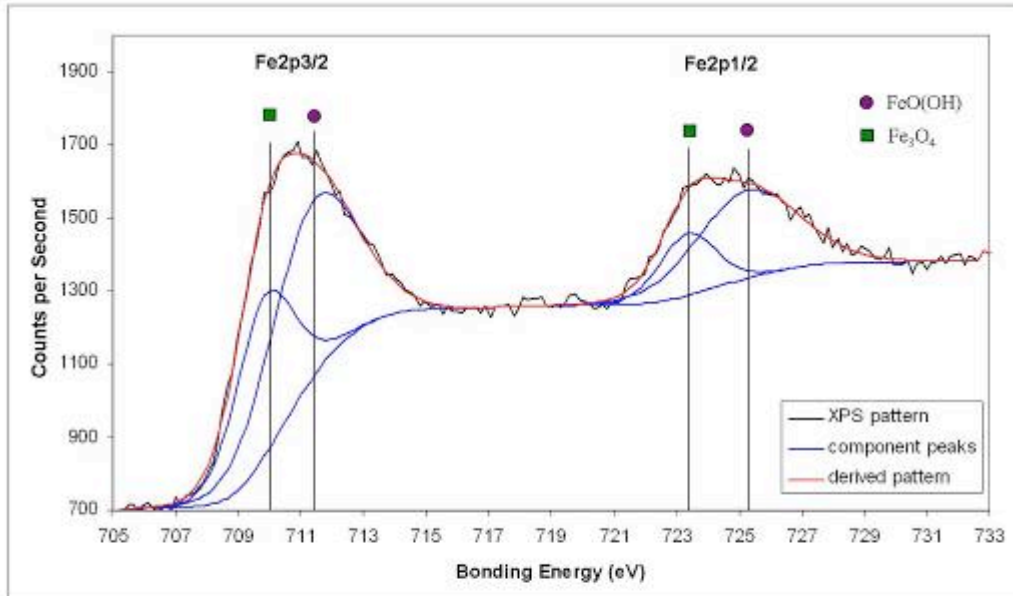
oxidation of iron(II) to iron(III) is energetically favourable as is the formation of  $\text{FeO}(\text{OH})_{(s)}$  and  $\text{Fe}(\text{OH})_{3(s)}$ . The slow kinetics of the reactions can be attributed to the partial stabilizing effect of the dibasic ammonium citrate. The above Gibbs free energy calculations do not incorporate the influence of citrate and the formation of metal-citrate complexes in the solution. These effects were omitted due to the difficulty of obtaining thermodynamic data for these complexes. If the effects of citrate were included in the above calculations, the Gibbs free energy changes would be expected to be more positive (less negative) due to the stabilizing effect on the metal ion reactants.

XPS was used to determine the identity of the precipitate. The results confirmed that the precipitate is an iron-based oxide/hydroxide. Select regions of an XPS pattern which correspond to the iron (2p<sub>3/2</sub> and 2p<sub>1/2</sub>) and oxygen (1s) bonding energies are shown in Figure 4-8. Based on the XPS spectrum, the precipitate appears to be composed of two phases:  $\beta\text{-FeO}(\text{OH})$  (akaganeite) [Oszkó99] and  $\text{Fe}_3\text{O}_4$  (magnetite) [Tan90]. The relative intensity of the peaks indicate that  $\text{FeO}(\text{OH})$  is the majority phase of the precipitate. The identification of the hydroxide phase is corroborated by the near equal intensities of the oxygen (1s) peaks in Figure 4-8 (b), which indicates a 1:1 ratio between hydroxide and oxide groups in this phase. The presence of  $\text{FeO}(\text{OH})$  confirms that the oxidation of iron(II) to iron(III) occurs in the solution (Eqn. 4.1.1) and indicates that this is followed by the reaction shown in Eqn. 4.1.3. There is no evidence for the formation of  $\text{Fe}(\text{OH})_3$  in the precipitate (Eqn. 4.1.2). The presence of  $\text{Fe}_3\text{O}_4$  [ $(\text{Fe}^{3+})_2(\text{Fe}^{2+})\text{O}_4$ ] indicates that not all the iron(II) is oxidized to iron(III) prior to precipitating out of solution. This phase is likely formed according to:

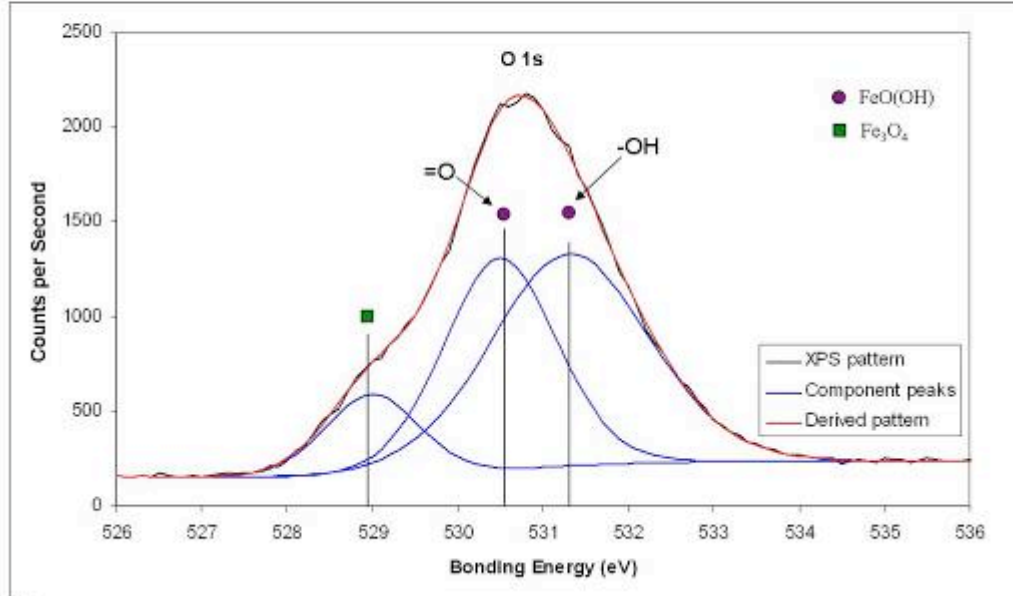


Other researchers have shown that the electrodeposition of the  $\text{Fe}_3\text{O}_4$  phase is typically favorable under high pH conditions and at elevated temperatures [Martinez07]. This agrees with the Gibbs free energy calculation which shows the reaction to be favourable at a pH of 3.5 (Appendix A). Previous studies have demonstrated that the formation of iron hydroxide/oxide precipitates is associated

with poor magnetic properties in iron-cobalt deposits [Liu00, Xu01, Bonhôte02, Tabakovic02, Osaka03, Bonhôte04, Osaka07]. Therefore, to limit these effects all subsequent electrodeposits were produced using fresh solutions.



a)

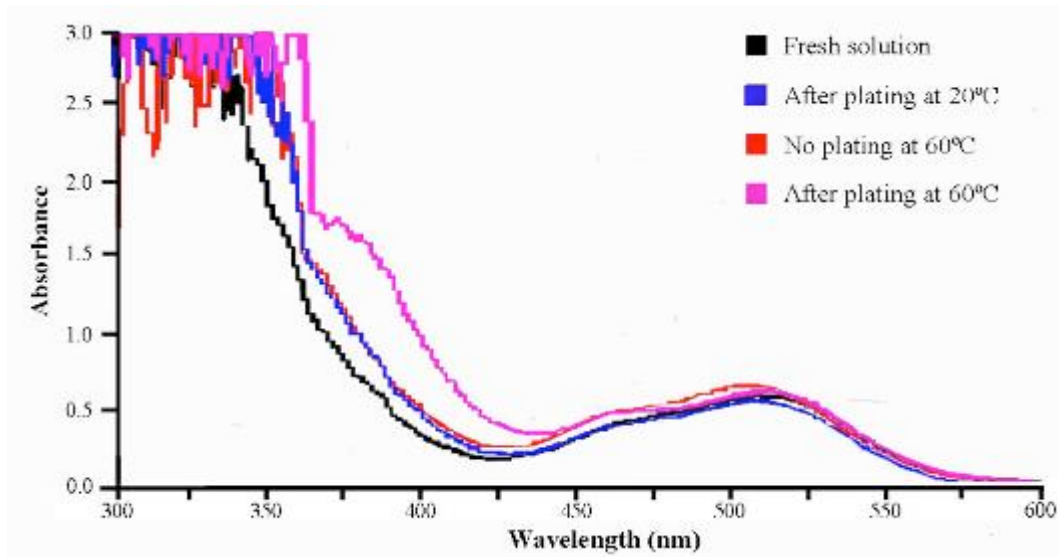


b)

**Figure 4-8:** Regions of an XPS spectrum obtained from an iron-cobalt solution precipitate which show: a) iron (2p<sub>3/2</sub> and 2p<sub>1/2</sub>) peaks and b) oxygen (1s) peaks.

#### 4.1.2 Stability of dibasic ammonium citrate stabilized solutions during use

UV-visible absorption spectra obtained from fresh plating solutions after heating and/or used for electroplating (Figure 4-9) show that both heating and the application of a potential across the plating cell accelerate the aging process. The decrease in solution stability at elevated temperatures is likely due to the influence of higher amounts of available ambient energy, which leads to increased rates of reaction. The potential applied across the solution during electroplating likely accelerates the aging process in two ways: 1) causes the oxidation of iron(II) to iron(III) at the anode and 2) causes the decomposition of water at the cathode to produce hydrogen gas and hydroxyl ions (Eqn. 2.3.2) [Osaka03]. The two effects appear to be cumulative, resulting in more severe aging in solutions used at elevated temperatures.



**Figure 4-9:** UV-visible absorption spectra of fresh electroplating solutions after heating and/or usage to deposit iron-cobalt thin-films.

The results show that even when fresh plating solutions are used, dibasic ammonium citrate is unable to prevent the change in valence and formation of precipitates in the solution. More precipitates likely form and can be incorporated into deposits when electroplating is done at elevated temperatures. This could

result in lower saturation magnetization values in these films.

## **4.2 Characterization of Iron-Cobalt Thin Films**

### **4.2.1 Effects of plating temperature on iron-cobalt thin films**

#### **4.2.1.1 Composition of iron-cobalt deposits**

The cobalt:iron ratio of the solution was 2.5:1 (cobalt:iron), which should result in deposits with compositions of ~71 at%Co assuming non-preferential plating by either species. EDX was used to determine the effects of plating temperature on the composition of electrodeposited iron-cobalt thin films. The EDX results are shown in Table 4-1. The EDX results show that at room temperature iron is preferentially deposited in the films at the expense of cobalt. As iron has a lower reduction potential than cobalt these results indicate slightly anomalous plating behaviour using the dibasic ammonium citrate stabilized plating solution at room temperature. This behaviour is well established in the literature [Liao87, Bertazzoli93, Liu00, Zhou09] and is thought to be the results of an inhibiting effect of iron(II) on the nucleation and growth of cobalt on the cathode surface [Bertazzoli93]. When the plating temperature was increased to 40°C the composition of the deposits closely reflects the composition that would be expected based on the metal-salt ratio in the plating solution. When the plating solution temperature is increased to 60°C the deposits become cobalt-rich. These results agree with the behaviour seen using similar plating solutions by other research groups [Park05, Zhou09]. EDX measurements taken using TEM indicate that the composition of the deposits is constant through their cross-sections.

**Table 4-1:** Composition of iron-cobalt thin films plated at various temperatures.

<b>Plating Temperature</b>	<b>Cobalt Composition (%)</b>	<b>Iron Composition (%)</b>	<b>2*Std. Error (%)</b>
<b>20°C</b>	68.3	31.7	1.2
<b>40°C</b>	71.6	28.4	1.1
<b>60°C</b>	75.7	24.3	0.9

The oxygen content of the deposits was determined using XPS, due to the low sensitivity of the SEM to light elements. The oxygen content of the iron-cobalt deposits are shown in Table 4-2.

**Table 4-2:** Oxygen composition of iron-cobalt deposits at various temperatures.

<b>Plating Temperature</b>	<b>Oxygen Composition (%)</b>	<b>2*Std. Error (%)</b>
<b>20°C</b>	4.0	1.8
<b>40°C</b>	3.3	0.4
<b>60°C</b>	4.5	0.8

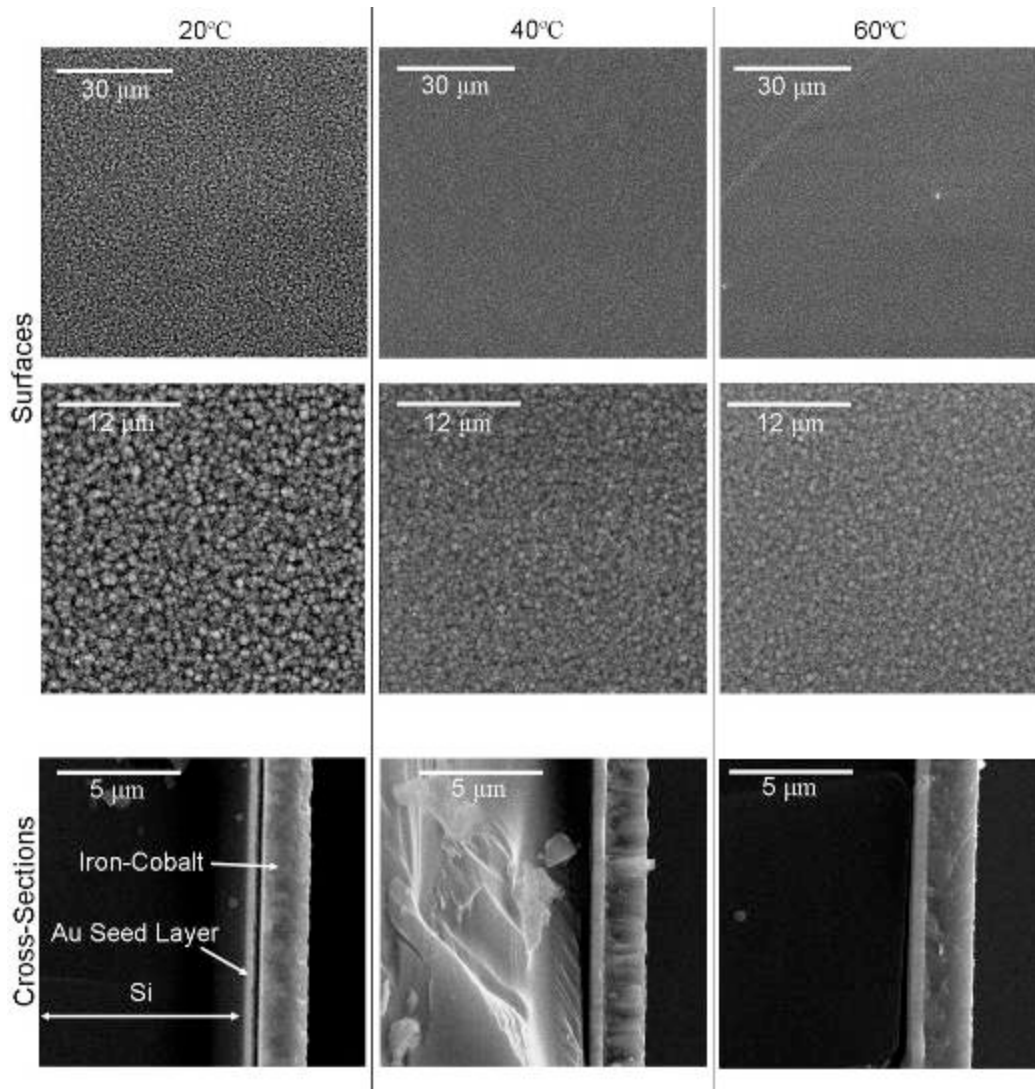
The results show that, including standard error considerations, the oxygen content of the films range from ~3-5 at%O. There appears to be slightly higher oxygen contents in films deposited at 60°C. Deposits plated at 20°C also tended to have higher oxygen contents; however, these deposits also exhibited larger standard errors making it difficult to make any conclusions regarding the influence of plating temperature on the oxygen content of the films. The ambiguity of the data is attributed to inaccuracies in the measurement of oxygen content using XPS analysis. The oxygen (1s) peak is partially covered by an iron Auger electron peak (LMM), which makes oxygen content difficult to measure. Regardless, the results in Table 4-2 show slightly higher oxygen contents for deposits plated at 60°C. Since it has previously been shown that electroplating at elevated temperatures

accelerates the formation of precipitates in the dibasic ammonium citrate stabilized plating solution (Section 4.1.2), the additional oxygen is likely due to the incorporation of these precipitates into the iron-cobalt deposits during electrodeposition. The XPS spectrum obtained from the precipitate (Section 4.1.1.2) indicates that the majority of the oxygen is most likely incorporated as  $\beta$ -FeO(OH) precipitates. As these precipitates are non-magnetic, their incorporation into the deposits should result in lower saturation magnetic flux density values. The incorporation of these precipitates may also affect other deposit properties such as resistivity, hardness and strength by imposing lattice strain in the deposits. Residual stresses as a result of these impurities, however, could compromise the integrity of the deposits.

#### **4.2.1.2 Morphology of iron-cobalt deposits**

SEM secondary electron (SE) micrographs of the surfaces and cross-sections of iron-cobalt films electrodeposited from the dibasic ammonium citrate stabilized plating solutions at various temperatures are shown in Figure 4-10. The surfaces of the deposits are typically quite smooth. The surfaces are characterized by small nodules which become finer as the plating temperature is increased. Although the nodules are similar to grains in appearance, TEM analysis indicates that the actual grain size of the deposits is actually on the order of tens of nanometers and, thus individual grains are not visible using SEM (see Section 4.2.3). The cross-sections of the deposits show that the deposits are very uniform and compact through their entire thickness. Some deposits appear to have a more columnar appearance than others, e.g., the deposit plated at 40°C in Figure 4-10. This, however, appears to vary from sample to sample and the trait does not appear with any consistency among deposits plated under similar conditions. It could be that the columnar appearance of certain deposits is due to the manner in which the sample was cleaved prior to SEM analysis.





**Figure 4-10:** SEM SE micrographs of iron-cobalt deposit surfaces when plated using the standard solution (Table 3-1) and conditions ( $15\text{mA}/\text{cm}^2$  for 9 minutes) at various temperatures.

Cracks were observed in many of the deposits and are typically more severe in deposits plated at lower temperatures. These deposits typically have lower cobalt contents. The presence of the cracks indicates a high amount of residual stress in the deposits. The relation between cracking and plating temperature was also noted by Zhang in his thesis work [Zhang05]. Based on the work of Zhou [Zhou09-2], the cracking is probably not a composition effect, i.e., due to a change in cobalt composition. Zhou's work concluded that increasing the cobalt content of the deposits actually leads to an increase in residual stress. The

cracking was less severe in cobalt-rich deposits, which implies that it must be a consequence of the plating temperature. The effect of temperature on stress reduction in electrodeposited alloys has often been attributed to a reduction in the overpotential for deposition of metallic species [Pangarov78]. A lowering of the overpotential allows the metal cations to migrate to the cathode surface more easily and allows the opportunity for ad-atoms to migrate to stable kink sites. In addition, a lower overpotential discourages the reduction of hydrogen at the cathode, which has also been shown to increase the residual stresses in electroplated films [Raub67].

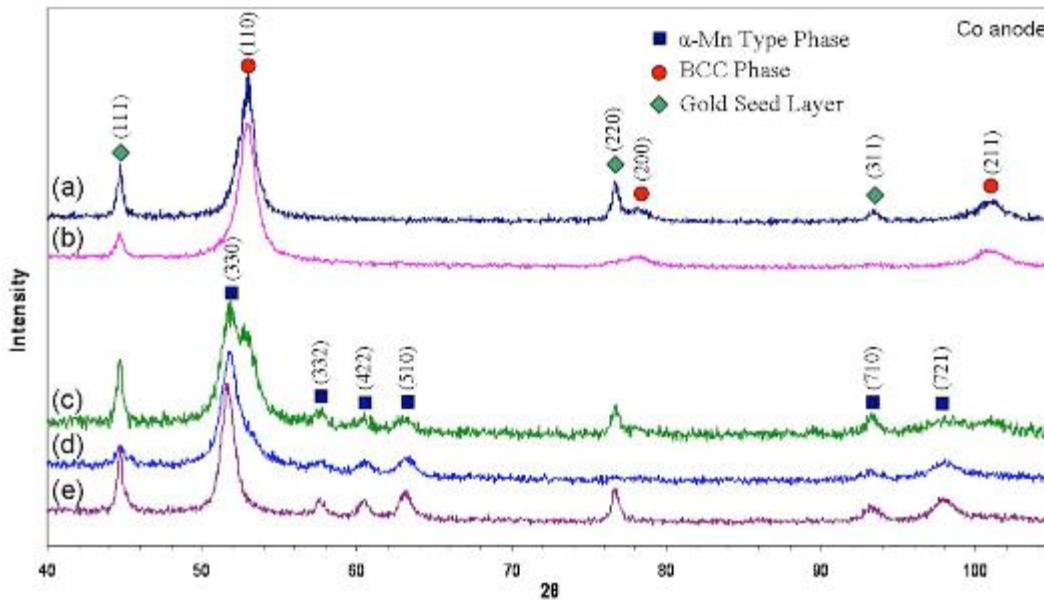
Profilometer measurements show that the thickness of the deposits varies over their surfaces. After 9 minutes of plating, using an average current density of 15 mA/cm<sup>2</sup>, the edges of the deposits can be as thick as 2.3µm while the interiors are typically 0.5-0.8µm thinner. Excluding the extreme edges of the samples, the average thicknesses of the deposits at various temperatures are shown in Table 4-3. Thickness measurements show that the deposit thickness on average increases with temperature. The increase in deposit thickness is attributable to the improved mass transport of metal cations from the bulk solution to the cathode surface at higher temperatures [Paunovic06]. The large standard errors of the measurements, however, show that the average thickness of the deposits can vary considerably regardless of temperature. This is thought to be the result of inaccuracies in estimating the plating areas on the silicon wafers prior to electroplating. These inaccuracies would translate to slight variation in the applied current density.

**Table 4-3:** Average thickness of iron-cobalt deposits at various temperatures.

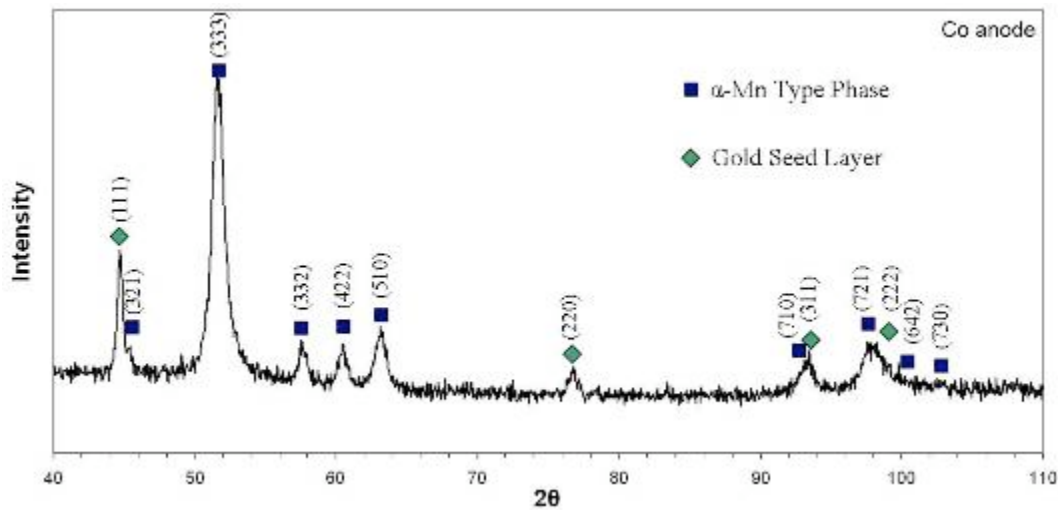
<b>Plating Temperature</b>	<b>Average Deposit Thickness (µm)</b>	<b>2*Std. Error (µm)</b>
<b>20°C</b>	1.67	0.08
<b>40°C</b>	1.70	0.07
<b>60°C</b>	1.73	0.08

### 4.2.1.3 Phases in iron-cobalt deposits

The effect of temperature on the deposited phases in iron-cobalt thin films was analyzed using XRD; the results are shown in Figure 4-11. The iron-cobalt BCC phase is deposited at room temperature. This is characteristic of the alloy at this temperature and composition, based on its equilibrium phase diagram [Baker92], and is consistent with the phase structure observed by other researchers in electrodeposited iron-cobalt thin-films [Liu00, Mattoso01, Myung01]. It should be noted that the FCC phase, which has been reported by Zhang et al. [Zhang07] using a tribasic ammonium citrate stabilized plating solution, was not detected. As the plating temperature is increased in the region between 30°C and 40°C, the equilibrium BCC phase begins to be codeposited along with a metastable phase which is isostructural to  $\alpha$ -Mn. When the temperature is increased further, the proportion of the film which is deposited as the  $\alpha$ -Mn type phase gradually increases until it eventually replaces the BCC phase at some temperature between 50°C and 60°C. The XRD pattern of the  $\alpha$ -Mn type phase for a deposit plated at 60°C can be seen in greater detail in Figure 4-12.



**Figure 4-11:** X-ray diffraction pattern for iron-cobalt thin films deposited using the standard plating solution and standard conditions at various temperatures: a) 20°C, b) 30°C, c) 40°C, d) 50°C, e) 60°C.



**Figure 4-12:** X-ray diffraction pattern of iron-cobalt film plated at 60°C using the standard plating solution and conditions, which shows additional peaks not observable in Figure 4-11.

Based on the peak positions for the phases in the XRD patterns the lattice parameters of the deposits were calculated and are tabulated in Table 4-4. Increasing the cobalt composition of the deposit leads to a small increase in the lattice parameter of the  $\alpha$ -Mn type phase. This is to be expected due to the slightly larger atomic radius of the cobalt atoms [Callister03]. The lattice parameter of the BCC phase, however, slightly decreases when the cobalt composition of the deposit is increased. This may indicate a slight enrichment of cobalt in the  $\alpha$ -Mn type phase relative to the BCC phase when the two phases are codeposited. This would cause the BCC phase to be slightly iron-rich in comparison to the overall deposit composition and would result in a reduction in its lattice parameter. The effect however is very small and the extremely fine grained and dispersed nature of the phases in these deposits makes the enrichment of cobalt in the  $\alpha$ -Mn type phase difficult to corroborate.

**Table 4-4:** Approximate lattice parameters of electrodeposited phases.

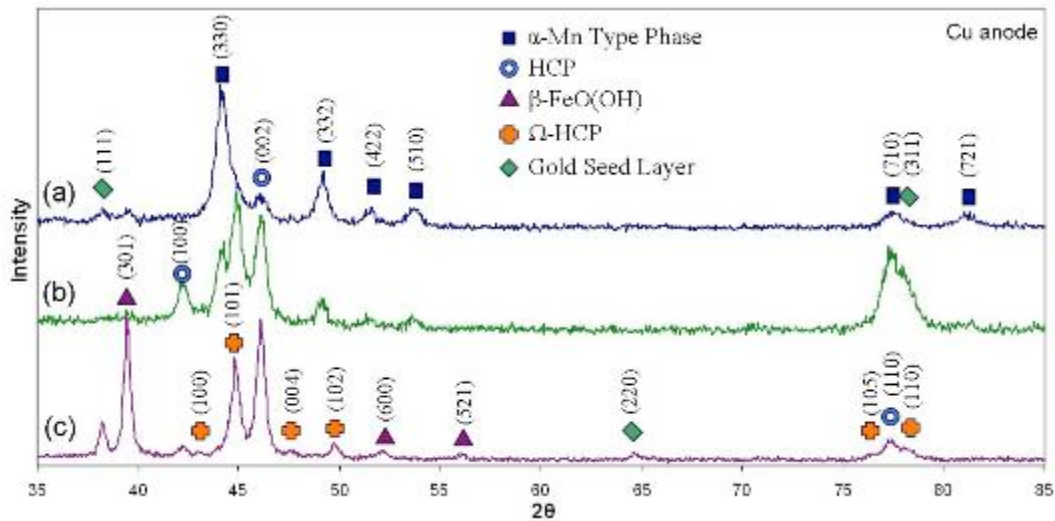
Plating Temperature	Average Cobalt Composition (%)	Average Iron Composition (%)	$\alpha$ -Mn Lattice Parameter (nm)	2*Std. Error (nm)	BCC Lattice Parameter (nm)	2*Std. Error (nm)
20°C	68.3	31.7	-	-	0.2842	0.0001
40°C	71.6	28.4	0.8697	0.0007	0.2837	0.0005
60°C	75.7	24.3	0.8708	0.0007	-	-

As was previously established in Section 4.2.1.1, elevated plating bath temperatures result in elevated cobalt contents in the deposits. It is not clear whether the appearance of the  $\alpha$ -Mn type phase is the result of higher cobalt compositions in the deposits or the increase in plating temperature. This question is resolved by referring to the work of Zhou et al. [Zhou09]. Zhou et al. were able to deposit the  $\alpha$ -Mn type phase in deposits with cobalt compositions ranging from 68-81 at%Co when plating at 40°C and from 60-85 at%Co at 60°C. Since the deposits in Figure 4-11 have compositions which range from ~68-76 at%Co, and the  $\alpha$ -Mn type phase can exist at any of these compositions, the formation of the  $\alpha$ -Mn type phase from this solution must result from the increase in plating bath temperature.

#### 4.2.1.3.1 Phases in iron-cobalt deposits from un-stabilized plating solutions

In order to determine if the dibasic ammonium citrate is responsible for the deposition of the  $\alpha$ -Mn type phase, deposits were prepared from a solution in which the reagent was omitted. The pH of the solution was adjusted to ~3.5 which is consistent with the natural pH of the dibasic ammonium citrate stabilized solution. XRD patterns from deposits produced at various temperatures from the un-stabilized plating solution are shown in Figure 4-13. At room temperature the  $\alpha$ -Mn type phase is the dominant phase, and the BCC phase is completely absent from the pattern. In addition to the  $\alpha$ -Mn type phase, two non-equilibrium

hexagonal iron-cobalt phases were also detected: a HCP phase (space group: P63/mmc) and a  $\Omega$ -HCP phase (space group: P6/mmm). The  $\beta$ -FeO(OH) phase (also known as akaganéite) was also identified in the iron-cobalt deposits. As the plating temperature is increased above room temperature, the  $\alpha$ -Mn type phase is replaced by the other phases until only residual amounts remain in deposits plated at 60°C.



**Figure 4-13:** XRD patterns from iron-cobalt deposits obtained using an unstabilized plating solution under standard plating conditions at various temperatures: a) 20°C, (b) 40°C and (c) 60°C.

The two hexagonal phases were also identified in electroplated iron-cobalt deposits by X.S. Zhou [Zhou09-2] when tribasic ammonium citrate stabilized plating solutions were used at elevated temperatures at their natural pH of 4.8. Although both hexagonal phases were never deposited together, they both tended to be deposited at elevated temperatures. Zhou also found that decreasing the pH of the tribasic ammonium citrate stabilized plating solution to 3.2 promoted the deposition of the equilibrium BCC phase. This points to a strong pH effect on the structure of deposited phases using iron-cobalt plating solutions.

The presence of the  $\beta$ -FeO(OH) phase suggests that precipitates are forming and are incorporated into the deposits, particularly at elevated temperatures. The XRD results help to corroborate the XPS results in Section

4.1.1.2 which identified precipitates obtained from aged plating solutions as being composed of mostly the  $\beta$ -FeO(OH) phase. The oxygen contents of deposits obtained using XPS analysis from the unstabilized iron-cobalt plating solutions are shown in Table 4-5. As with deposits plated from the dibasic ammonium citrate stabilized plating solution, plating at 60°C appears to promote the incorporation of oxygen into the deposits. The high  $\beta$ -FeO(OH) peaks observed in the XRD pattern at this temperature appears to support this conclusion. The effect of temperature on the oxygen content of deposits plated at lower temperatures is more ambiguous as the XPS results show similar oxygen contents between the deposits plated at 20°C and 40°C. The results also indicate that oxygen incorporation is slightly higher for deposits plated using the unstabilized plating solution in comparison with plated from the dibasic ammonium citrate stabilized solution (Table 4-2). The oxygen content of the deposits plated at 20°C and 40°C are close to the oxygen content of deposits plated from the dibasic ammonium citrate stabilized plating solution when it was used at 60°C. This suggests that the deposition of the  $\alpha$ -Mn type phase and other non-equilibrium hexagonal phases are related to the overall oxygen content of the deposits. Increasing oxygen levels in the deposits first leads to the formation of the  $\alpha$ -Mn type phase, and at higher concentrations, the hexagonal phases. Since only single measurements were taken from deposits plated using the unstabilized plating solution, error values are not shown in Table 4-5. This is because, as shown in Section 4.2.1.1, the error associated with XPS measurements tend to be large in general and even larger when using an unstabilized plating solution for which precipitate is far more time sensitive than a stabilized solution. For this reason it was not deemed useful to perform additional XPS measurements on deposits obtained from the unstabilized solution.

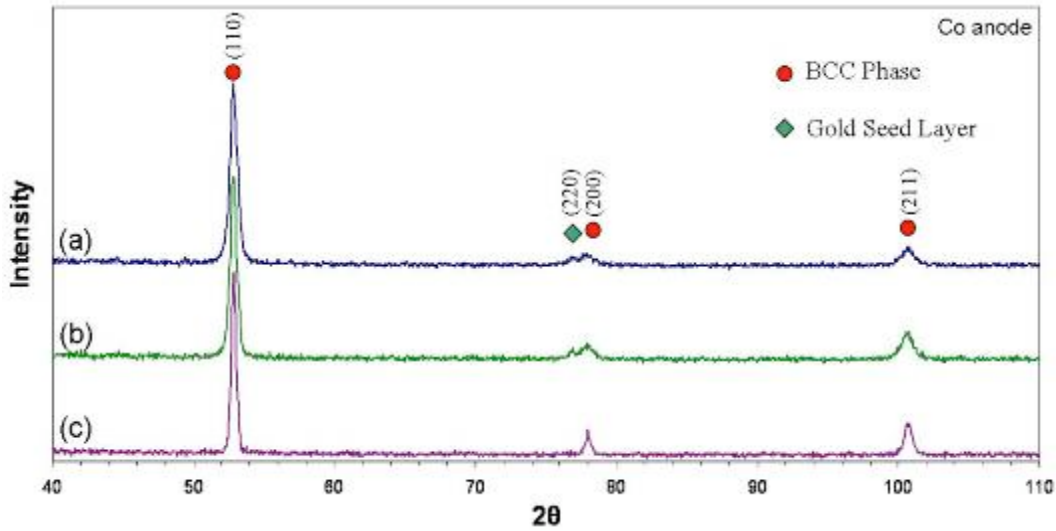
**Table 4-5:** Oxygen contents of iron-cobalt deposits plated from un-stabilized plating solutions using XPS.

<b>Plating Temperature</b>	<b>Oxygen Composition (%)</b>
<b>20°C</b>	4.8
<b>40°C</b>	4.8
<b>60°C</b>	5.6

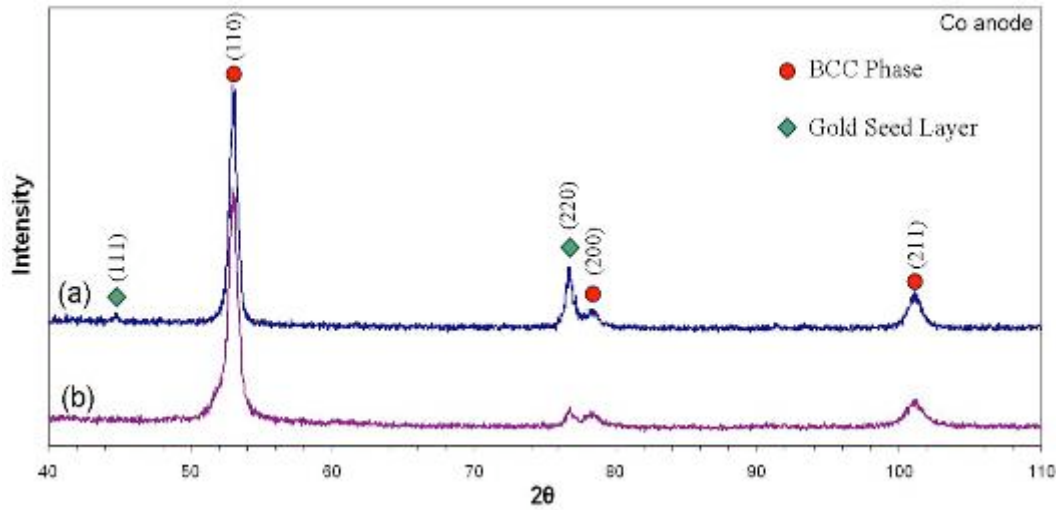
#### **4.2.1.3.2 Effects of pH on phases in iron-cobalt deposits**

When the pH of the dibasic ammonium citrate stabilized solution and the unstabilized solutions are reduced to 2.3 (the pH suggested by Osaka et. al. [Osaka03] to avoid the formation of precipitates in their solution), the equilibrium BCC phase is the only phase deposited, as shown in Figure 4-15 and Figure 4-15. The XRD patterns in Figure 4-14 and Figure 4-15 show that at a pH of 2.3 the equilibrium BCC phase is the only phase deposited between 20°C and 60°C using both the dibasic ammonium citrate stabilized and unstabilized plating solutions. The lack of  $\alpha$ -Mn type phase even at elevated temperatures in either of the solutions indicates that deposition of the phase is strongly pH dependent.





**Figure 4-14:** XRD patterns of iron-cobalt deposits plated from the standard dibasic ammonium citrate plating solution under standard plating conditions with the pH adjusted to 2.3: a) 20°C, b) 40°C, c) 60°C.



**Figure 4-15:** XRD patterns of iron-cobalt deposits plated from the standard plating solution without dibasic ammonium citrate under standard plating conditions with the pH adjusted to 2.3: a) 20°C, b) 60°C.

#### 4.2.1.3.3 Interpretation of phase formation in iron-cobalt deposits

The results in Section 4.2.1.3.1 show that dibasic ammonium citrate in the plating solution is not necessary for the  $\alpha$ -Mn type phase to be deposited. On the contrary, dibasic ammonium citrate instead appears to prevent the deposition of

the  $\alpha$ -Mn type phase at low temperatures in favor of the BCC phase. Increasing the plating temperature, however, promotes the deposition of the  $\alpha$ -Mn type phase in the dibasic ammonium citrate stabilized plating solution and the deposition of the hexagonal phases, as well as  $\beta$ -FeO(OH), in the unstabilized solution. It was established in Section 4.1.2 that electroplating at elevated temperatures accelerates the formation of precipitates in the dibasic ammonium citrate stabilized plating solution, which correlates with higher oxygen contents in the deposits. This may indicate that the formation of the  $\alpha$ -Mn type phase and other non-equilibrium phases are possibly the result of the incorporation of impurities, in the form of iron-oxide precipitates, into the deposits.

The formation the  $\alpha$ -Mn type phase structure in alloy systems has previously been attributed to the incorporation of large impurities in thin film deposits [Simmonds96]. This case is not unique; the presence of dispersed impurities has been shown to lead to the formation of metastable phases in many thin-film systems [Chopra69, Povetkin96, Tochitskii96]. It is theorized that the formation of these metastable phases is caused by localized distortions in the crystal lattice, which result from the incorporated impurities. The distortions interfere with the electrocrystallisation process and in doing so prevent the formation of equilibrium phases [Tochitskii96]. That the dibasic ammonium citrate both stabilizes the solution and prevents the formation of the metastable  $\alpha$ -Mn type phase at room temperature indicates that under these conditions it is able to successfully complex the metal cations and prevent the incorporation of impurities. As the bath temperature is increased, however, the dibasic ammonium citrate may no longer be able to prevent the formation and resultant incorporation of precipitates into the deposits, which results in the  $\alpha$ -Mn type phase being deposited. Since the unstabilized plating solution had no complexing agents, the  $\alpha$ -Mn type phase was deposited even at room temperature. As the temperature increased so too did the amount of incorporated precipitates, which is indicated by the presence of the  $\beta$ -FeO(OH) in the XRD patterns and the increased oxygen content in the deposits determined through XPS. The additional precipitates may have led to the formation of the non-equilibrium hexagonal phases. The hexagonal

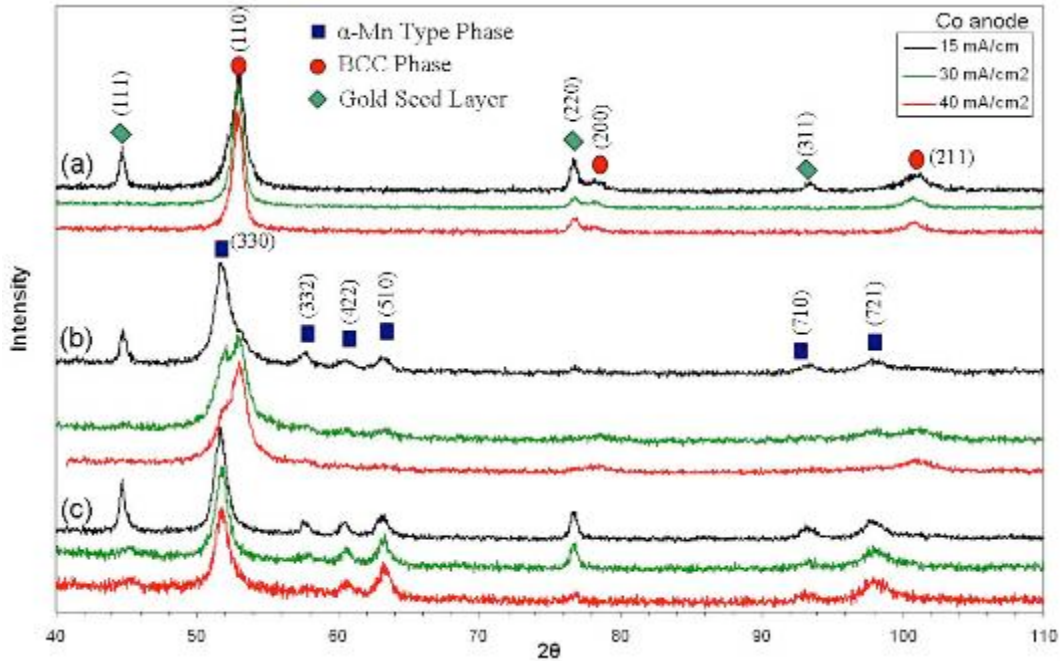
phases were also observed by Zhou [Zhou09-2] in deposits plated using a tribasic ammonium citrate stabilized plating solution. That these phases were observed in both the tribasic ammonium citrate stabilized solution and the unstabilized solution indicates that, at its natural pH the tribasic ammonium citrate has little or no stabilizing effect on the solution during electroplating. This conclusion is supported by thermodynamic calculations performed by Zhou, which demonstrated that the concentration of tribasic ammonium citrate that was used was insufficient to adequately complex all the iron in the plating solution [Zhou09-2].

The importance of pH on the deposition of metastable phases is shown by the inability to form any phase other than the equilibrium BCC phase, regardless of temperature, when the pH of both the dibasic ammonium citrate stabilized and unstabilized plating solutions was adjusted to 2.3. This relation is echoed in the work of Zhou [Zhou09-2] who showed that while the tribasic ammonium citrate stabilized plating solution behaved like an unstabilized solution when used at its natural pH of 4.8 when the pH of the solution was reduced to 3.2 it was possible to deposit only the equilibrium BCC phase at room temperature. The effect of pH on phase formation is likely due to the reduced availability of hydroxyl ions in solution at low pH values, which prevents the formation of iron hydroxide based precipitates.

#### **4.2.2 Effects of current density on iron-cobalt thin-films**

XRD patterns obtained from iron-cobalt deposits plated at various temperatures and current densities are shown in Figure 4-16. The current density does not affect the phase compositions of the deposits plated at 20°C and 60°C. These temperatures are well within established single phase temperature regions and are, therefore, less susceptible to the influences of current density on phase deposition. Based on the relative peak heights between the phases in deposits plated at 40°C, however, there is a noticeable tendency to form more BCC phase,

rather than the  $\alpha$ -Mn type phase, as the plating current density is increased. High current densities are usually favorable to the formation of metastable phases as the correspondingly higher overpotential provides additional energy for the formation of phases which would normally be unstable [Paunovic06, Cohen-Hyams04]. High current densities also lead to the formation of smaller grains and to hydrogen evolution, both of which have been shown to cause the formation of metastable phases [Chopra69]. Since the increase in current density in this system appears to promote the formation of the equilibrium BCC phase, the formation of the  $\alpha$ -Mn type phase must be due to an effect other than the high overpotential, small grain size or hydrogen evolution. Previous results indicate that the formation of the  $\alpha$ -Mn type phase is associated with the formation and incorporation of precipitate particles into the deposit. It is unclear, however, how higher current densities would prevent the formation or integration of precipitates into the deposit or if the precipitate content of films deposited at higher current densities are any lower than those deposited at low current densities. Further work would need to be conducted in order to determine the reason that high current densities favour the deposition of the BCC phase.

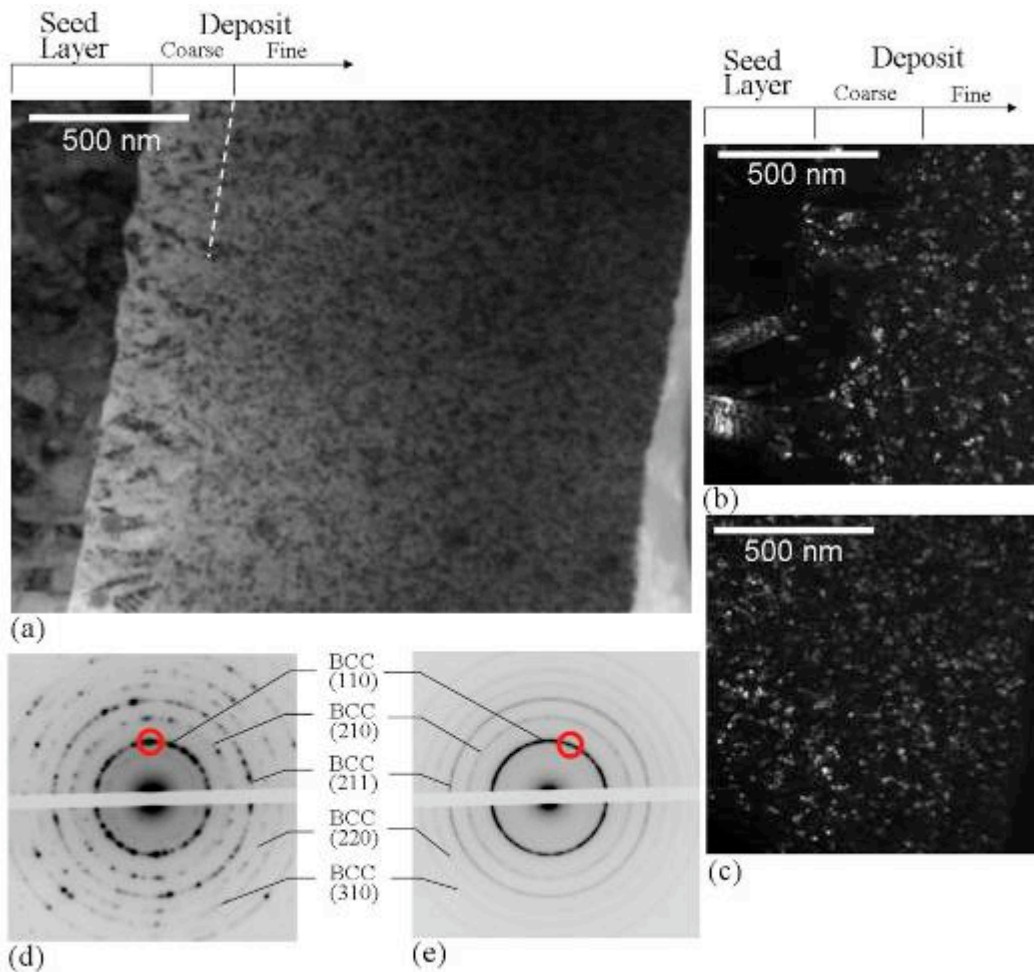


**Figure 4-16:** XRD patterns showing the effects of current density on phase deposition using the standard plating solution and plating for 9 minutes at various temperatures: a) 20°C, (b) 40°C and (c) 60°C.

### 4.2.3 Transmission electron microscopy

Cross-section samples of iron-cobalt deposits were characterized using TEM. Micrographs and electron diffraction patterns taken from the cross-section of an iron-cobalt deposit plated at 20°C are shown in Figure 4-17. From the bright field micrograph (Figure 4-17 (a)) it is apparent that the deposit is made up of two morphologically different regions: the deposit immediately adjacent to the seed layer and the bulk of the deposit. Dark field images taken from the two regions (Figure 4-17 (b and c)) show that immediately adjacent to the seed layer the grain structure of the deposit tended to be coarser than the bulk of the deposit. The bulk of the deposit has grains which are ~5-20nm in diameter. The deposit adjacent to the seed layer has grains which are ~10-40nm in diameter. The grains appear to be randomly orientated throughout the thickness of the deposit. From the electron diffraction patterns the difference in grain size through the deposit's cross-section

is evident. The electron diffraction pattern obtained from the deposit near the seed layer (Figure 4-17 (d)) is made up of a concentric but spotty ring pattern, which indicates a coarser grain structure than the deposit bulk which has a much more continuous ring pattern (Figure 4-17 (e)). The electron diffraction patterns confirm the phase identification that was done through XRD and show that the deposit is made up of the BCC phase, which extends through the entirety of the deposit's thickness. In addition to the BCC phase several faint rings were also observed in the deposit near the seed layer (Figure 4-17 (d)). Identification of the phase from these faint rings is difficult, however, based upon a much clearer ring pattern observed in an annealed deposit (Figure 4-29) the phase is likely  $\text{Fe}_3\text{O}_4$  (space group:  $Fd\bar{3}m$ ). The faintness of the ring pattern indicates that the oxide is present in only trace amounts and is therefore unlikely to be detected using XRD analysis. The presence of this phase confirms the presence of oxides which were likely incorporated into the deposit during the electroplating process.

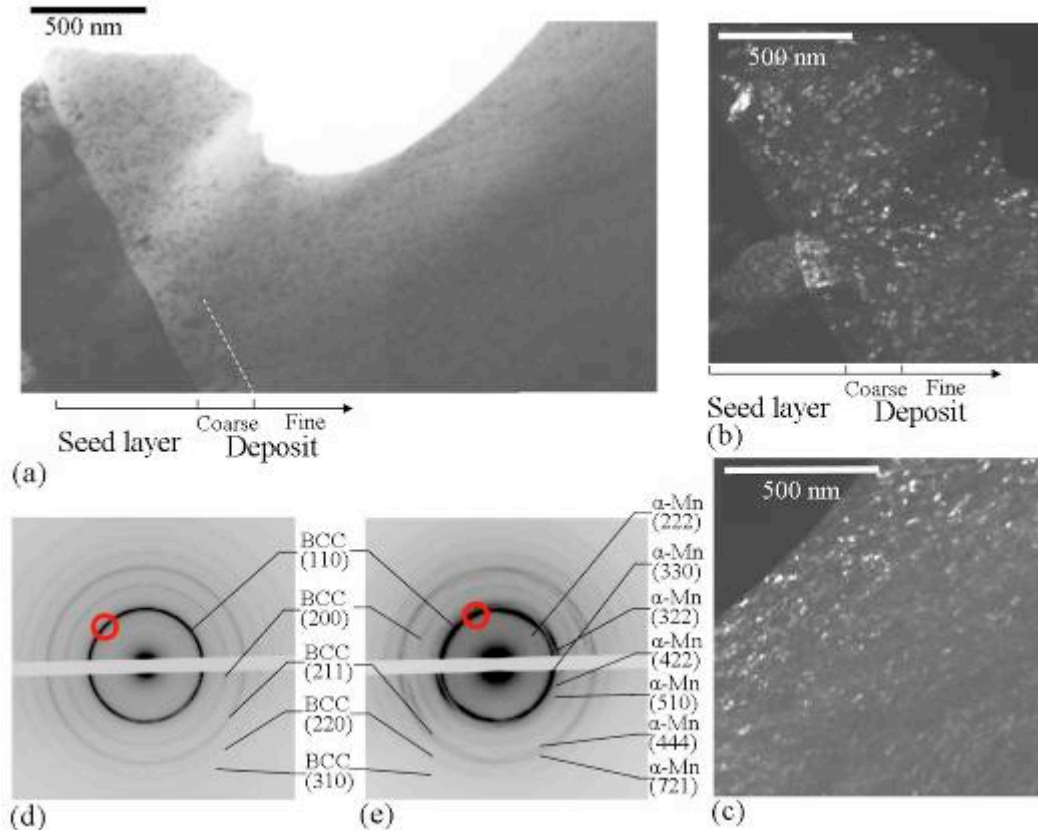


**Figure 4-17:** TEM micrographs and electron diffraction patterns from the cross-section of a deposit plated at 20°C: (a) bright field image, (b-c) dark field images from adjacent to the seed layer and the bulk deposit, respectively and (d-e) electron diffraction patterns from adjacent to the seed layer and the bulk deposit, respectively. Dark field images were taken using the portions of the electron diffraction rings denoted with red circles.

TEM micrographs and electron diffraction patterns showing the cross-section of a deposit plated at 40°C are shown in Figure 4-18. This deposit can also be characterized as having two distinct morphological regions: the region next to the seed layer and the bulk of the sample. Dark field micrographs indicate that near the seed layer (Figure 4-18 (b)) the deposit is made up of small grains (~5-20nm), which are randomly orientated. The bulk deposit (Figure 4-18 (c)) is characterized by equally fine grains, however, the grains appear to have some degree of preferred orientation. The electron diffraction patterns (Figure 4-18 (d

and e)) confirm the presence of both the BCC and the  $\alpha$ -Mn type phase, however, the two are not codeposited through the entire deposit thickness. The electron diffractions patterns reveal that near the seed layer the deposit is made up of only the BCC phase. It is only further into the bulk of the deposit that the  $\alpha$ -Mn type phase is observed. The  $\alpha$ -Mn type phase in the bulk deposit also shows evidence of being textured, as indicated by the incomplete rings, which correspond to the  $\alpha$ -Mn type phase, in Figure 4-18 (e). The proximity of the BCC and  $\alpha$ -Mn type phase rings in the electron diffraction pattern makes it impossible to image the separate grains from the two phases using dark field microscopy. Since the  $\alpha$ -Mn type phase is deposited only further into the deposit, the equilibrium BCC phase must be deposited first with the  $\alpha$ -Mn type phase forming later. The lag between the start of electroplating and the formation of the  $\alpha$ -Mn type phase may indicate that the phase may result from a localized increase in pH, which has been shown to occur near the cathode surface during electroplating [Cooper05]. Unlike the deposit plated at 20°C there is no definitive evidence for any oxides in the deposit plated at 40°C from the electron diffraction patterns. The possibility for their presence in the bulk deposit, however, still remains as the strongest diffracting ring for the  $\text{Fe}_3\text{O}_4$  phase, (331), lies very close to the  $\alpha$ -Mn type phase (222) ring and could therefore be present but not discernable from the electron diffraction pattern.

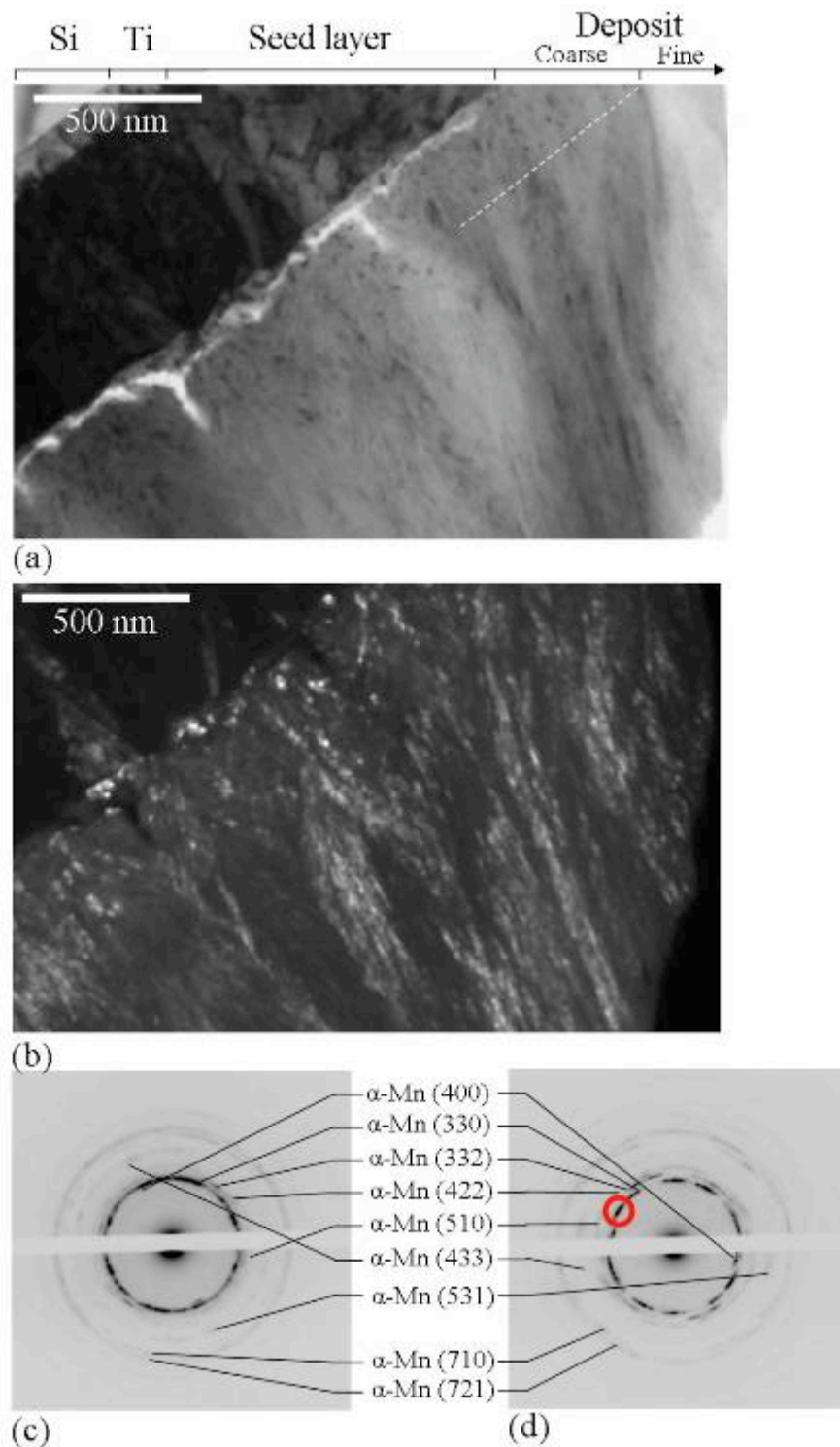




**Figure 4-18:** TEM micrographs and electron diffraction patterns from the cross-section of a deposit plated at 40°C: (a) bright field image, (b-c) dark field images from adjacent to the seed layer and the bulk deposit, respectively and (d-e) electron diffraction patterns from adjacent to the seed layer and the bulk deposit respectively. Dark field images were taken using the electron diffraction areas denoted with red circles.

TEM micrographs taken from a deposit plated at 60°C are shown in Figure 4-19. This deposit also has a region immediately adjacent to the seed layer that is morphologically distinct from the bulk of the sample. From the dark field micrograph (Figure 4-19 (b)), like the sample plated at 40°C, the region adjacent to the seed layer is made up of small randomly oriented grains (~10-20nm). The bulk of the deposit, however, appears considerably different from the previous samples; it is composed of long fibrous regions, which are made of small similarly oriented grains, extending perpendicularly from the seed layer. This morphological feature was also observed in the deposit plated at 40°C, but it was much less extensive. The electron diffraction patterns (Figure 4-19 (c-d)) show

that the deposit is composed of the  $\alpha$ -Mn type phase through the entire thickness. Like the deposit plated at 40°C, there is no definitive evidence of any oxides in the deposit based on the electron diffraction patterns. The incomplete rings in the electron diffraction pattern taken from the deposit's bulk confirm the preferred orientation observed in the dark field image. It is unclear as to why this microstructure forms. This morphological feature could indicate that the small grains, which comprise the bulk of the deposit, were once part of single grains that had recrystallised at some point after being deposited. This could explain the similar orientation of the grains and their orientation relative to the seed layer. Recrystallisation is often the result of either temperature or strain effects, which provide the driving force for the formation of new grain boundaries [Gross99, Callister03]. Since the deposition was done at the relatively low temperature of 60°C, recrystallisation would likely be driven by residual stresses imposed on the deposit during deposition either through defects or through the incorporation of impurities. Although cracking of the deposit, and thus residual stress, appeared to be more severe in deposits plated at lower temperatures the stress may have been accommodated by recrystallization rather than cracking in high temperature deposits. Further study, however, would be necessary to determine the exact mechanism for the formation of this morphology in the deposit.



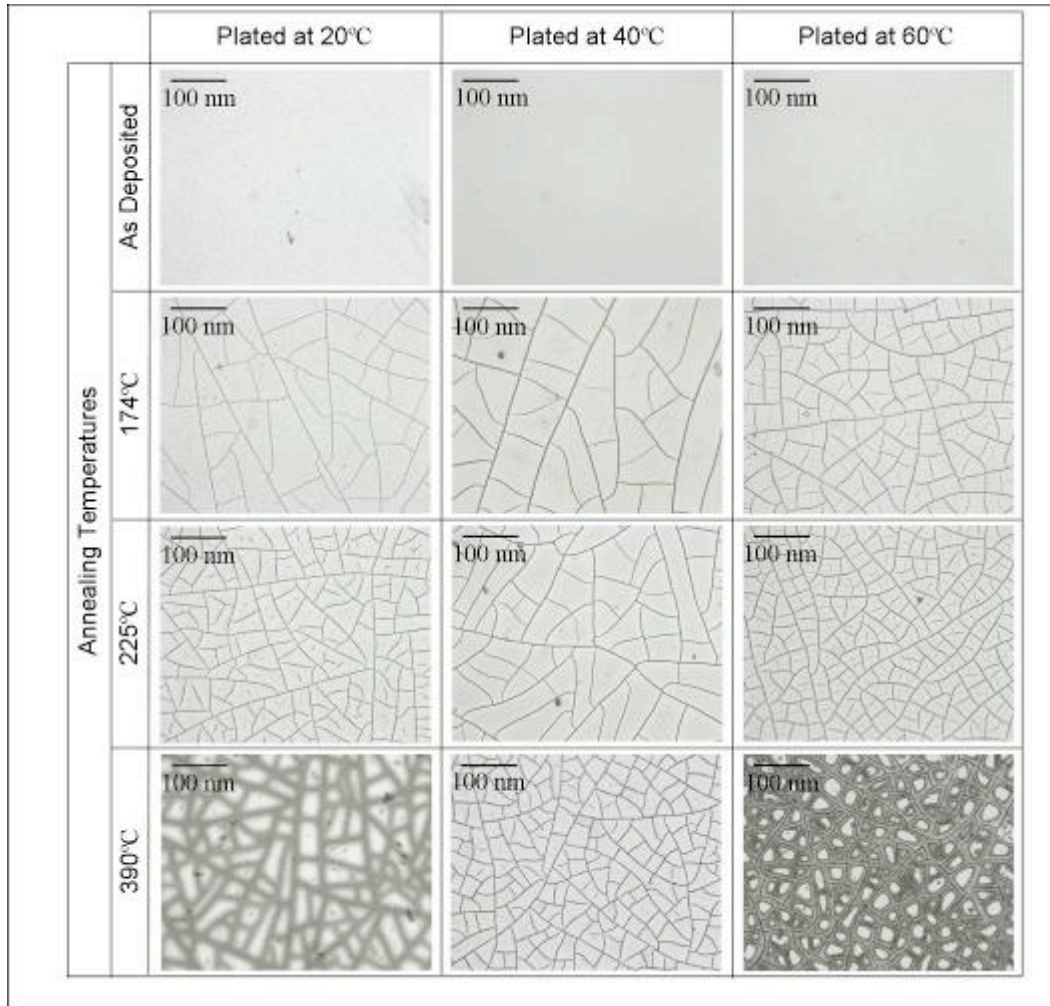
**Figure 4-19:** TEM micrographs and electron diffraction patterns from the cross-section of a deposit plated at 60°C: (a) bright field image, (b) dark field image and (c-d) electron diffraction patterns from adjacent to the seed layer and the bulk deposit respectively. The dark field image was taken using the electron diffraction area denoted with the red circle.

## **4.3 Annealing of iron-cobalt deposits**

### **4.3.1 Deposit morphology**

Prior to annealing, the surfaces of the iron-cobalt deposits are typically flat and smooth (see Section 4.2.1.2). After annealing, however, the deposits exhibit substantial cracking. Optical micrographs from iron-cobalt deposits after annealing at various temperatures are shown in Figure 4-20. The cracks become prominent features on the deposits surfaces after annealing at 174°C for deposits plated at all temperatures. As the annealing temperature is increased the amount of cracking becomes more severe until at 390°C the surface is not only covered in cracks but has also lost large areas of material surrounding the cracks. The cracking is particularly severe for the deposits plated at 20°C and 60°C. Deposits plated at 40°C showed less cracking than deposits plated at other temperatures although significant cracking was still observed. When the deposits are annealed, the thermal stresses due to the differential expansion of the deposits and substrates may lead to the substantial cracking on these deposits surfaces. The coefficients of thermal expansion of gold, silicon and a bulk iron-cobalt alloy of similar composition to the ones deposited are shown in

Table 4-6. The coefficients of thermal expansion of the materials show that gold will expand much more than both silicon and the iron-cobalt alloy upon heating. As the gold layer is bonded to both the iron-cobalt deposit and the silicon substrate, via a thin titanium adhesion layer, thermal expansion as a source of the cracking seen in the deposits seems plausible.



**Figure 4-20:** Optical micrographs of the surfaces of iron-cobalt deposits after annealing at various temperatures.

**Table 4-6:** The coefficients of thermal expansion of materials present in the iron-cobalt deposits at 20°C [Bonnenberg80<sup>a</sup>, Bauccio93<sup>b</sup>].

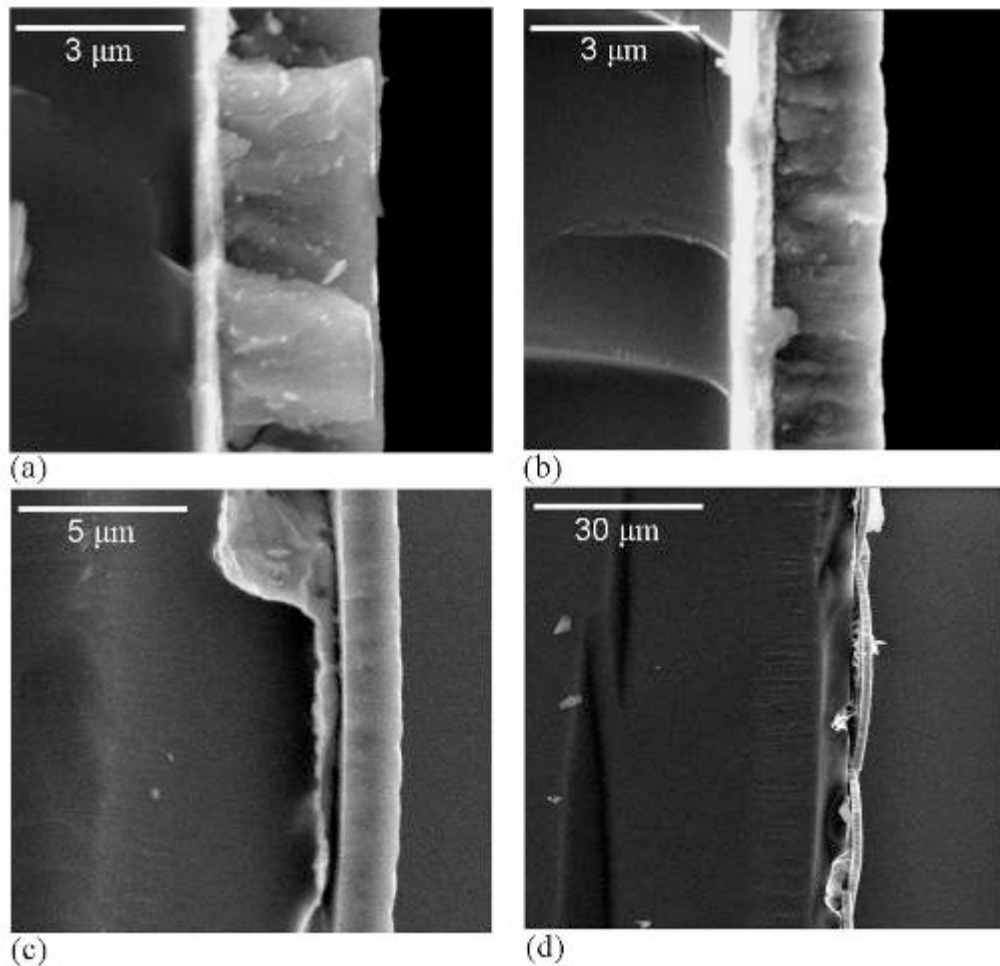
<b>Material</b>	<b>Coefficient of Thermal Expansion (<math>\mu\text{m}/(\text{m}\cdot^{\circ}\text{C})</math>)</b>
<b>Co<sub>7</sub>Fe<sub>3</sub></b>	8.1 [a]
<b>Au</b>	14.2 [b]
<b>Si</b>	5.0 [b]

The samples plated at 20°C already showed signs of residual stress in the

form of cracking and minor delamination even before annealing. The severity of the cracking in these deposits after annealing, in comparison to the deposits plated at 40°C, could be due to stress relief during the annealing process. The samples plated at 60°C also showed extensive cracking; these deposits, however, did not exhibit any cracking or bonding problems after deposition and before annealing. The literature indicates that the  $\alpha$ -Mn type phase can transform at temperatures as low as 160°C [Jay01], meaning that any of the annealing temperatures tested would result in the phase transformation. Based on the XRD peak position for deposits before and after the phase transformation the atomic density of the deposits can be estimated. Atomic density calculations for deposits plated at 60°C indicate that the atomic densities of the BCC and  $\alpha$ -Mn type phase are  $\sim 87.3 \pm 0.5$  atoms/nm<sup>3</sup> and  $\sim 87.8 \pm 0.5$  atoms/nm<sup>3</sup>, respectively. The difference in atomic density between the two phases is, therefore, approximated to be less than 0.5 atoms/nm<sup>3</sup>, with the  $\alpha$ -Mn type phase having a slightly higher atomic density than the BCC phase. Such a small change in density makes it unlikely that the cracking exhibited in these deposits is the result of a volume change that occurs when the metastable  $\alpha$ -Mn type phase transforms into the BCC phase during the annealing process. The cracking in these deposits must, therefore, also be attributed to residual stresses within the deposits which are relieved through cracking during the annealing process. These stresses may be due to incorporated precipitates, which are incorporated in the deposits when deposited at elevated temperatures (Section 4.2.1.1). The deposits plated at 40°C showed the least cracking. This is most likely due to a lower residual stress in the films due to lower amounts of incorporated precipitates coupled with better bonding between the deposit and the substrate (relative to the 20°C deposits).

Cross-sectional SEM micrographs of annealed deposits are shown in Figure 4-21. The cross-sectional micrographs show that, regardless of annealing temperature, the iron-cobalt films retain their dense uniform structure through their thickness. This was found for all deposits for all plating temperatures. Most deposits remained well adhered to the substrate when annealed at temperatures up to 225°C (Figure 4-21 (a-b)). When annealed at  $\sim 390^\circ\text{C}$ , however, the deposits

tended to bow and delaminate from the substrate (Figure 4-21 (c-d)). In addition, there appears to be a reaction between the seed layers and the silicon substrate in the deposits plated at  $\sim 390^{\circ}\text{C}$ . The result of this reaction leads to the formation of voids and cracks under the deposit, which undoubtedly contributes to the poor adhesion of the deposits. Further analysis of the reacted layer is covered in Section 4.3.3. Inconsistencies in the appearance of the seed layers of the deposits annealed at  $\sim 174^{\circ}\text{C}$  and  $\sim 245^{\circ}\text{C}$  in Figure 4-21 may indicate that reactions have occurred between the seed layers and deposits at these temperatures. EDX analysis, however, indicates that no reaction has taken place.

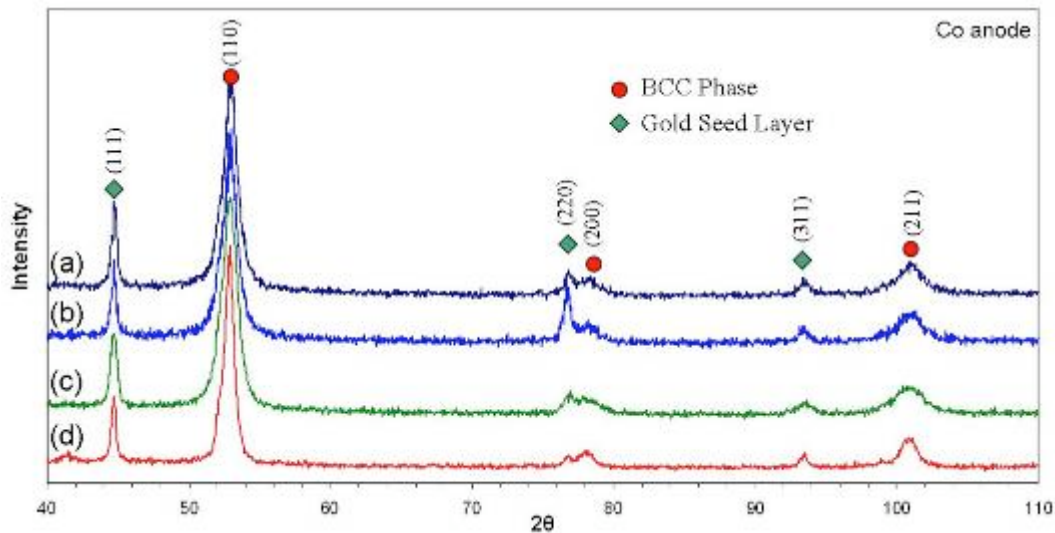


**Figure 4-21:** SEM BSE cross-sectional micrographs of iron-cobalt thin films deposited at  $40^{\circ}\text{C}$  and annealed at: (a)  $174^{\circ}\text{C}$ , (b)  $225^{\circ}\text{C}$  and (c-d)  $390^{\circ}\text{C}$ .

## 4.3.2 Phase composition

### 4.3.2.1 Effects of annealing temperature

The effects of annealing temperature on the phase structure of deposits plated at 20°C are shown in Figure 4-22. It can be seen that annealing samples plated at 20°C has no effect on the phases present in the deposits. There is a noticeable thinning of the peaks as the annealing temperature is increased, which would correspond to a coarsening of the grain structure in the deposits. This indicates that when annealing at temperatures above 390°C for 4 hours the grains have undergone stress relief and grain growth. Larger grains are known to have poorer coercivities and therefore it might be expected that the deposits annealed at high temperatures should have poorer magnetic properties.

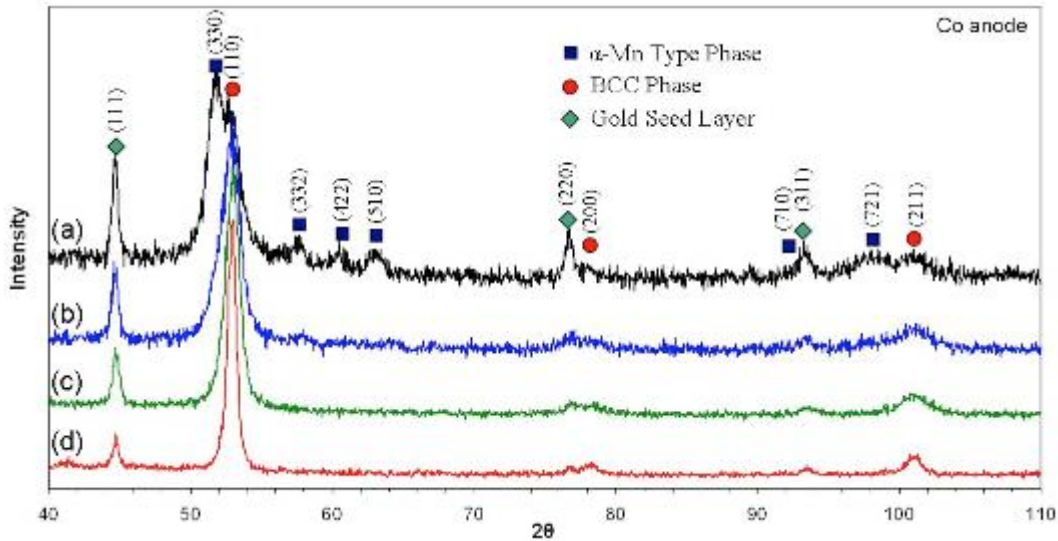


**Figure 4-22:** XRD patterns for iron-cobalt deposits plated at 20°C using the standard iron-cobalt plating solution and parameters: a) as deposited, (b) annealed at 174 °C, (c) annealed at 225 °C and (d) annealed at 390 °C.

The effects of annealing temperature on the phase structure of deposits plated at 40°C are shown in Figure 4-23. From the XRD patterns it can be seen that the  $\alpha$ -Mn type phase transforms to the BCC phase when annealed at temperatures above ~174°C. This agrees with the findings of Jay et al. [Jay01]



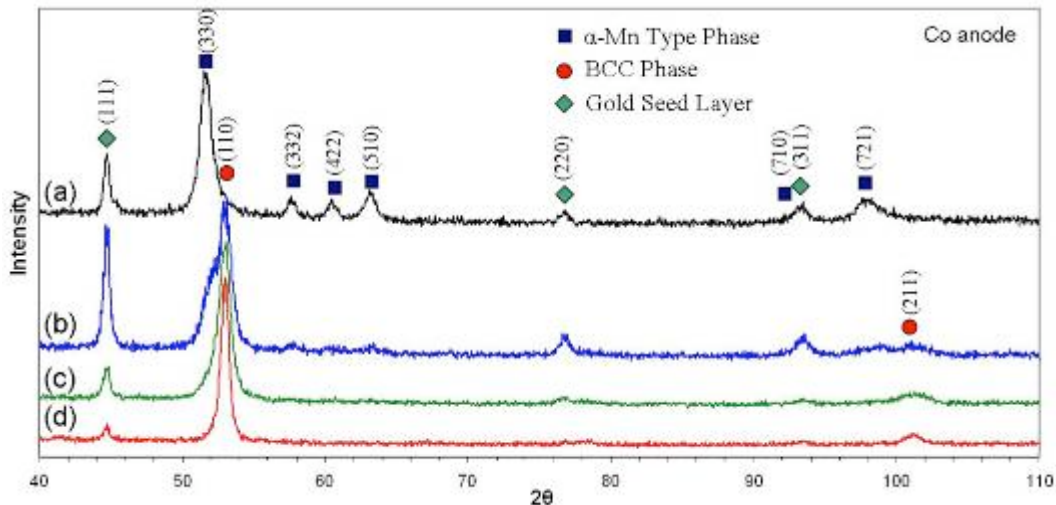
who found that transformation of the  $\alpha$ -Mn type phase commences at temperatures above 160°C. It can be seen that when annealed at ~174°C the  $\alpha$ -Mn type phase has been mostly replaced by the BCC phase. When annealed at ~225°C the transformation is complete after 4 hours of annealing. At higher temperatures narrowing of the peaks, indicating a coarsening of the grain structure, is observed.



**Figure 4-23:** XRD patterns for iron-cobalt deposits plated at 40°C using the standard iron-cobalt plating solution and parameters: a) as deposited, (b) annealed at 174°C, (c) annealed at 225°C and (d) annealed at 390°C.

The effects of annealing temperature on the phase structure of deposits plated at 60°C are shown in Figure 4-24. Partial transformation of the completely  $\alpha$ -Mn type microstructure is readily observable. Like the samples plated at 40°C, partial transformation to the BCC phase is observed in the deposits annealed at ~174°C and complete transformation is observed in the deposits annealed at ~225°C. Also noticeable is the lack of the BCC(200) peak in the annealed samples. This indicates that when the BCC phase is formed from the  $\alpha$ -Mn type phase it forms as a highly textured phase. The BCC(200) peak is visible in both Figure 4-22 and Figure 4-23, which shows that the BCC phase is not textured in its electrodeposited form. Texturing occurs upon annealing during the phase transformation from the  $\alpha$ -Mn type phase to the BCC phase. The textured nature of the  $\alpha$ -Mn type phase in the deposits plated at elevated temperatures was already

observed through dark field TEM micrographs and electron diffraction patterns (Section 4.2.3). It is, therefore, likely that the preferred orientation observed in the transformed BCC phase is attributable to it being formed from the textured  $\alpha$ -Mn type phase. Based on relative peak intensities, the  $\alpha$ -Mn type phase appears to have a (330) preferred texture, which is preserved as a (110) preferred orientation in the newly formed BCC phase. The (330) and (110) crystallographic planes, in the  $\alpha$ -Mn type phase and the BCC phase, respectively, have similar d-spacings (2.053 nm and 2.006 nm), since the BCC phase has a lattice parameter  $\sim 1/3$  the value for the  $\alpha$ -Mn type phase. As such, the transformation of the  $\alpha$ -Mn type phase to the BCC phase appears to involve only slight movement of the Co and Fe atoms. This would account for the conservation of texture during transformation and is consistent with the low transformation temperature ( $\sim 160^\circ\text{C}$ ), which is prohibitive to the large-scale diffusion of atoms.

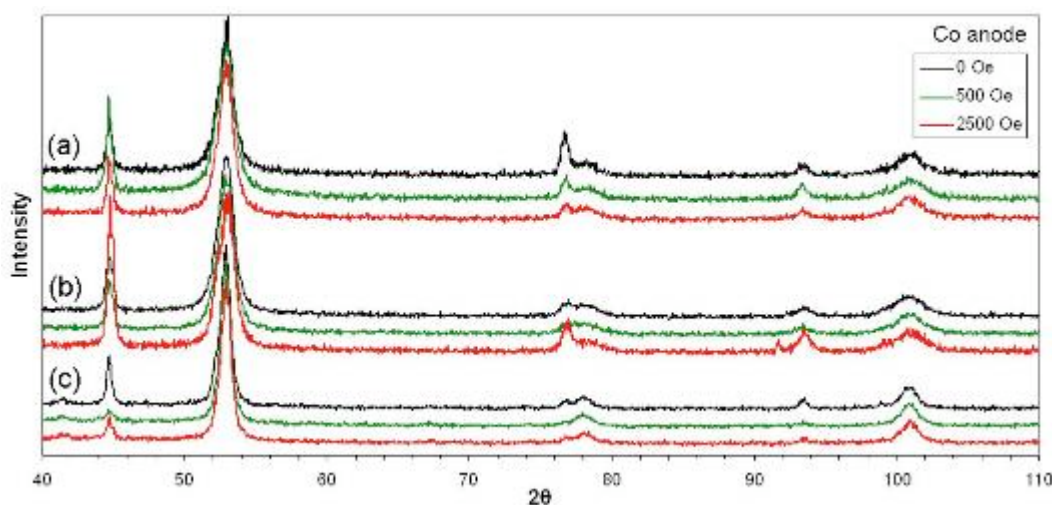


**Figure 4-24:** XRD patterns for iron-cobalt deposits plated at  $60^\circ\text{C}$  using the standard iron-cobalt plating solution and parameters: a) as deposited, (b) annealed at  $174^\circ\text{C}$ , (c) annealed at  $225^\circ\text{C}$  and (d) annealed at  $390^\circ\text{C}$ .

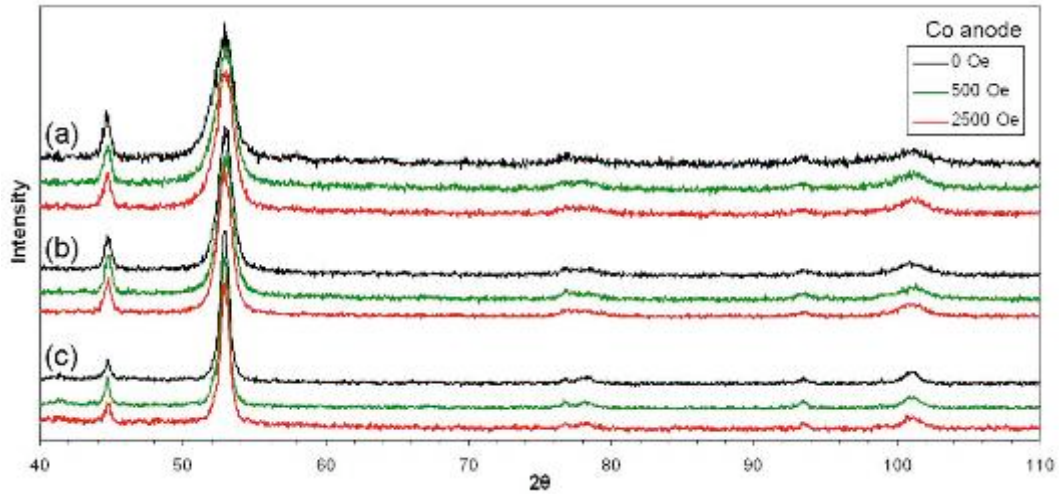
#### 4.3.2.2 Effects of applied magnetic field during annealing

The effects of various applied magnetic fields on phase transformation during annealing are shown in Figure 4-25, Figure 4-26 and Figure 4-27. The

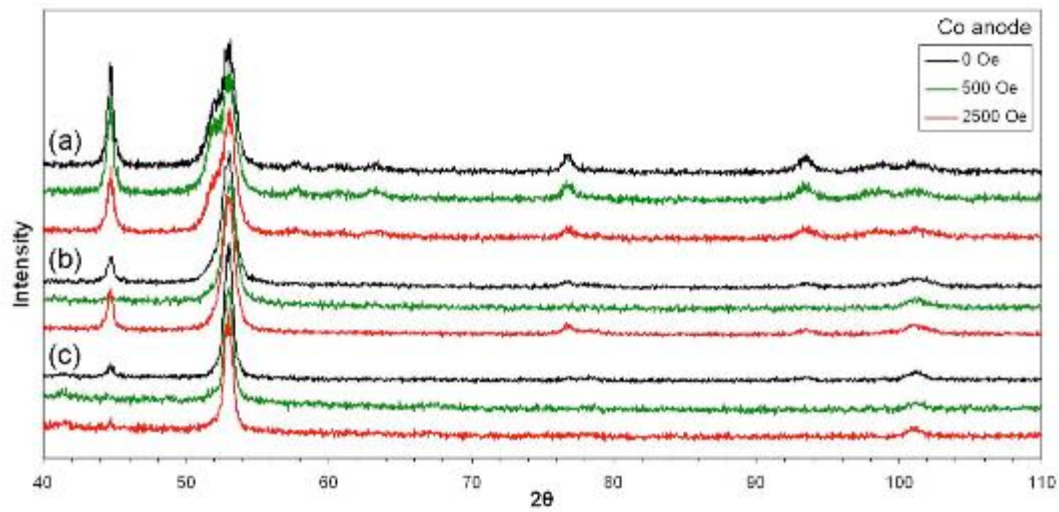
results in the below figures show that there is no difference between the XRD patterns of deposits annealed with and without an applied external magnetic field nor does the strength of the magnetic field affect the XRD patterns of the deposits. While annealing under the influence of strong magnetic fields have been shown to influence the texture development of magnetic material [Bacaltchuk03, Masahashi98] these effects are typically seen when annealing at much higher temperatures and under much stronger magnetic fields. It is unlikely that, under the conditions tested, the annealing temperatures and magnetic fields were high enough to cause the formation of textured phases. Magnetic annealing however does not require a change in crystallographic texture but rather an introduction of a small degree of atomic ordering within the alloy [Cullity72]. The results, therefore, indicate only that any changes observed in the magnetic properties of the deposits after magnetic annealing cannot be attributed to changes in the crystallographic texture of the deposits.



**Figure 4-25:** XRD patterns for iron-cobalt deposits plated at 20°C using the standard iron-cobalt plating solution and parameters, and annealed under various magnetic fields at: a) 174°C, (b) 225°C and (d) 390°C.



**Figure 4-26:** XRD patterns for iron-cobalt deposits plated at 40°C using the standard iron-cobalt plating solution and parameters, and annealed under various magnetic fields at: a) 174°C, (b) 225°C and (d) 390°C.



**Figure 4-27:** XRD patterns for iron-cobalt deposits plated at 60°C using the standard iron-cobalt plating solution and parameters, and annealed under various magnetic fields at: a) 174°C, (b) 225°C and (d) 390°C.

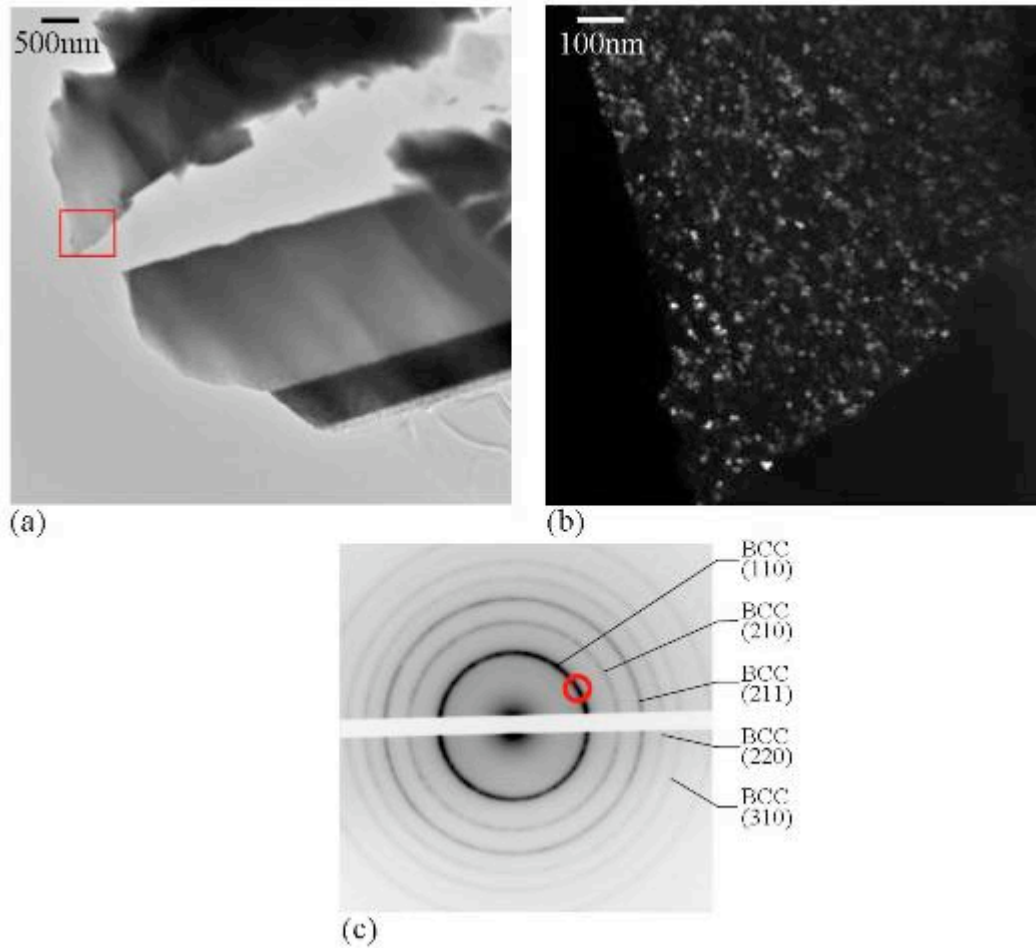
### 4.3.3 TEM analysis of annealed deposits

#### 4.3.3.1 TEM analysis of deposits plated at 20°C and then annealed

TEM micrographs and electron diffraction patterns taken from a deposit plated at 20°C and annealed at ~174°C are shown in Figure 4-28. The TEM micrographs (Figure 4-28 (a-b)) show that the morphology of the deposit plated at 20°C has not undergone any substantial change after being annealed at ~174°C. The dark field micrograph (Figure 4-28 (b)) shows that the grains are 5-20nm in size and are randomly oriented in the deposit, which is similar to the characteristics observed in the unannealed deposits. The electron diffraction pattern (Figure 4-28 (c)) indicates that the deposit is still composed of the BCC phase.

TEM micrographs and electron diffraction patterns taken from a deposit plated at 20°C and annealed at ~390°C are shown in Figure 4-29. The bright field image (Figure 4-29 (a)) shows that the microstructure though the thickness of the film is quite uniform, with no evidence of a fine and coarse grained microstructure as was seen in the as-plated 20°C deposits. The Au seed layer and substrate regions, however, look considerably different from those seen in previous samples. The gold seed layer has had its grain size greatly reduced and has become highly porous. The pores indicate that the gold has diffused from the seed layer and into the titanium layer and silicon substrate or into the deposit itself. EDX analysis indicates that, while there was no gold in the bulk deposit, gold was detected in the deposit near the seed layer. There is also a noticeable change in the silicon substrate near the interface which changed from a single silicon crystal to a multiphase polycrystalline region. The formation of new phases indicates that reactions have taken place between the silicon substrate and either the deposit or, more likely, the gold/titanium layers. The dark field micrograph (Figure 4-29 (b)) shows that the deposit has an average grain size of ~20nm, although the grain size ranges from ~12-40nm, and the grain size is consistent through the thickness of the deposit. There was also no sign of any preferred orientation in the grains

through the deposit. These results confirm the XRD results obtained from similar deposits (Figure 4-22), which showed a sharpening of the diffraction peaks, indicating grain growth and no change in texture, unlike the deposits plated at higher temperatures.



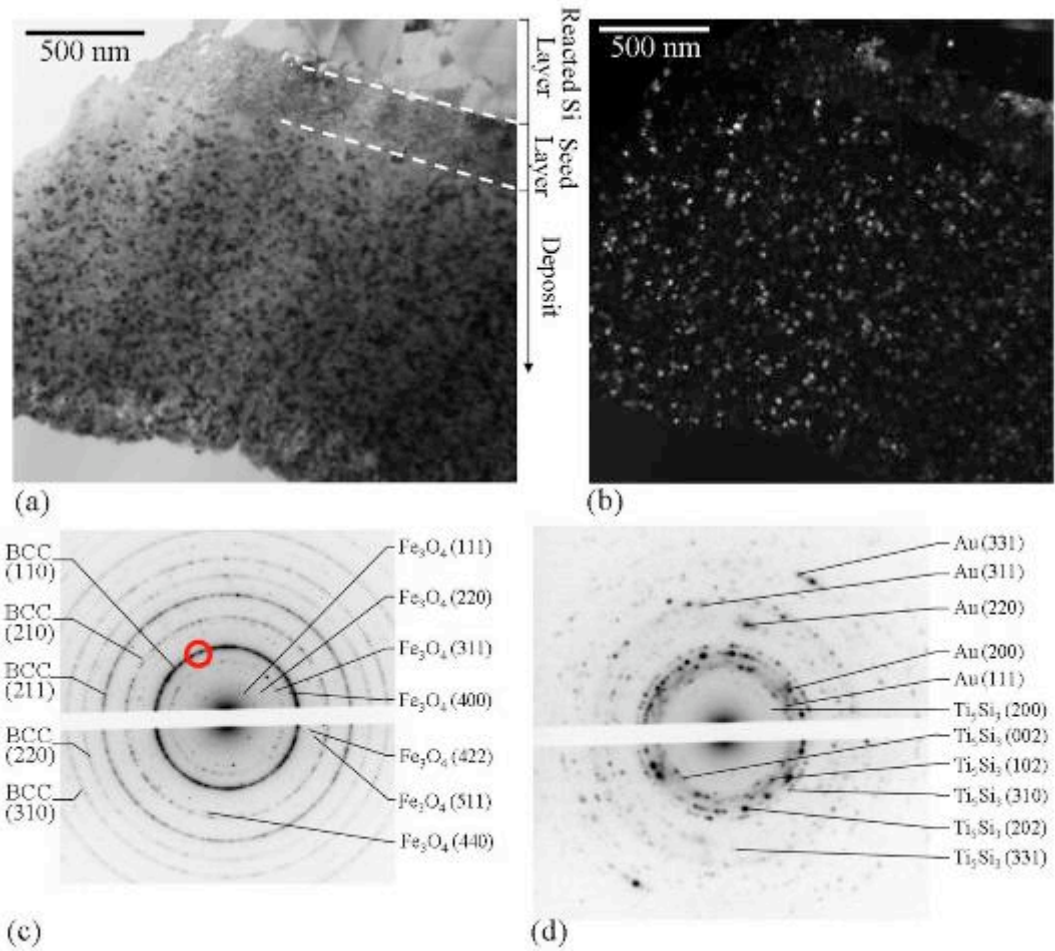
**Figure 4-28:** TEM micrographs and electron diffraction patterns from the cross-section of a deposit plated at 20°C and annealed at ~174°C: (a) bright field image, (b) dark field image and (c) electron diffraction pattern from the bulk of the deposit. The dark field image was taken from the region marked with a red box using the portion of electron diffraction ring denoted with the red circle.

The electron diffraction pattern taken from the bulk deposit (Figure 4-29 (c)) confirms that the BCC phase is still present in the deposit after annealing at ~390°C, however, a second phase is also present which has been identified as



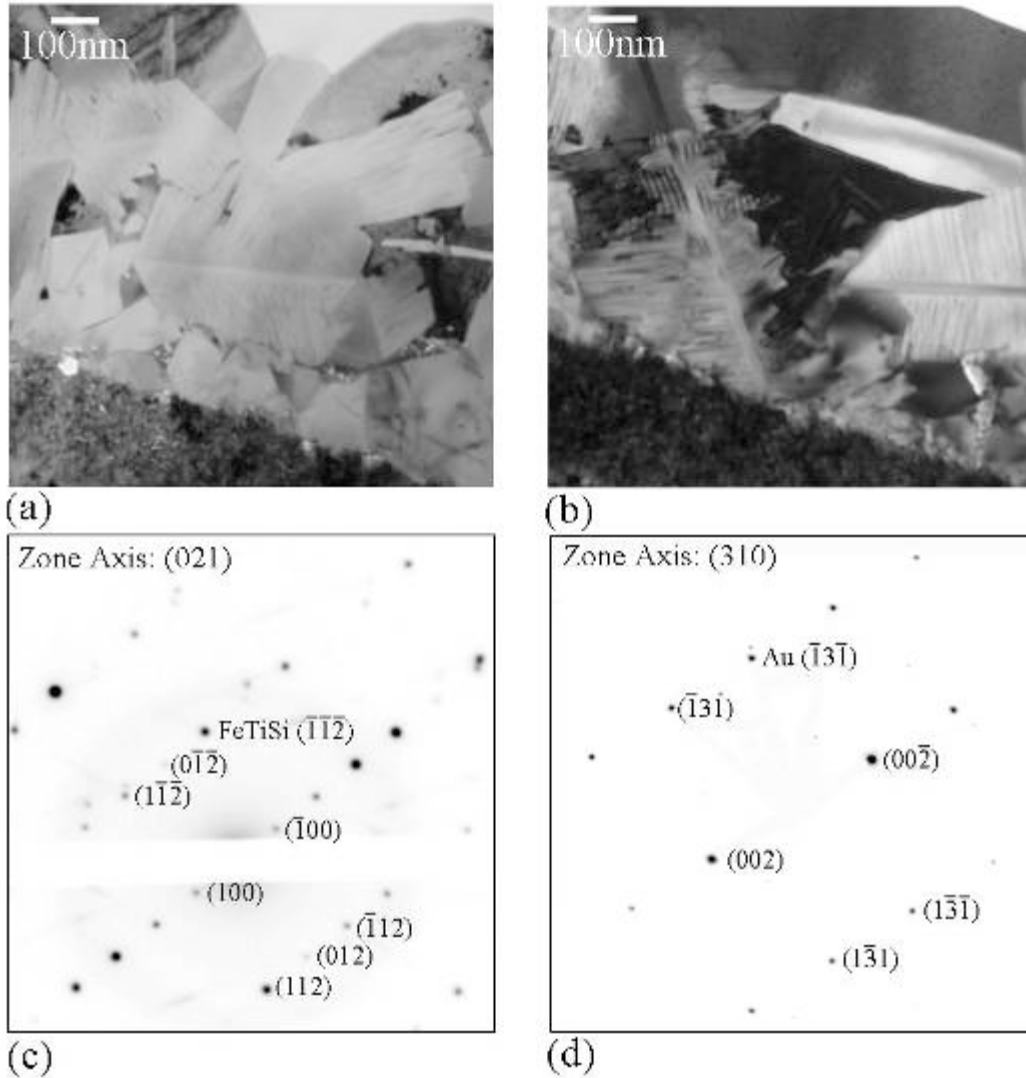
$\text{Fe}_3\text{O}_4$  (space group:  $Fd\bar{3}m$ ). The  $\text{Fe}_3\text{O}_4$  phase appears to be present in only trace amounts which is likely why it is not detected though XRD analysis. This phase was also detected in the as-deposited films plated at room temperature (Section 4.2.3) but the rings were much less intense. The increased intensity of the rings could indicate that more  $\text{Fe}_3\text{O}_4$  was incorporated in the film during deposition or  $\text{Fe}_3\text{O}_4$  could have formed during the annealing process despite the use of a reducing atmosphere. Another possibility is that the oxide had some amorphous character when deposited and was able to crystallize during annealing, which resulted in more visible diffraction rings. The electron diffraction pattern taken from the original gold seed layer (Figure 4-29 (d)) shows that, in addition to the expected gold phase, a  $\text{Ti}_5\text{Si}_3$  phase (space group:  $P63/mcm$ ) was also identified. The presence of this phase confirms that the titanium adhesion layer and silicon substrate diffuse into the gold seed layer when annealed at  $\sim 390^\circ\text{C}$  for 4 hours.

TEM micrographs and electron diffraction patterns from the reacted region of the silicon substrate are shown in Figure 4-30. The bright field micrographs (Figure 4-30 (a-b)) show that the reacted layer is composed of several large grains. Based upon electron diffraction patterns obtained from the reacted Si region (Figure 4-30 (c-d)), at least two distinct phases are present. The bright grain at the centre of Figure 4-30 (a) was identified as an orthorhombic (Fe,Co)TiSi phase (space group:  $Ima2$ ). EDX analysis of the phase supports this identification as the Ti to (Co,Fe) ratio was approximately 1:1. The presence of this phase indicates that, in addition to the seed layer, adhesion layer and substrate, the deposit atoms diffuse through the seed layer and react when annealing is done at  $\sim 390^\circ\text{C}$ . The consumption of the iron-cobalt in the reaction should decrease the overall amount of magnetic material in the deposit and cause a decrease in the saturation flux density. The dark phase at the centre of Figure 4-30 (b), which was also seen in the reacted layer, was identified through its electron diffraction pattern to be gold (space group:  $Fm\bar{3}m$ ). The presence of gold in the silicon substrate shows that its diffusion is favorable when annealed at  $390^\circ\text{C}$  and accounts for the porous appearance of the original seed layer.



**Figure 4-29:** TEM micrographs and electron diffraction patterns from the cross-section of a deposit plated at 20°C and annealed at ~390°C: (a) bright field image, (b) dark field image and (c-d) electron diffraction patterns from the bulk deposit and the gold seed layer, respectively. The dark field image was taken using the portion of the electron diffraction ring denoted with the red circle.





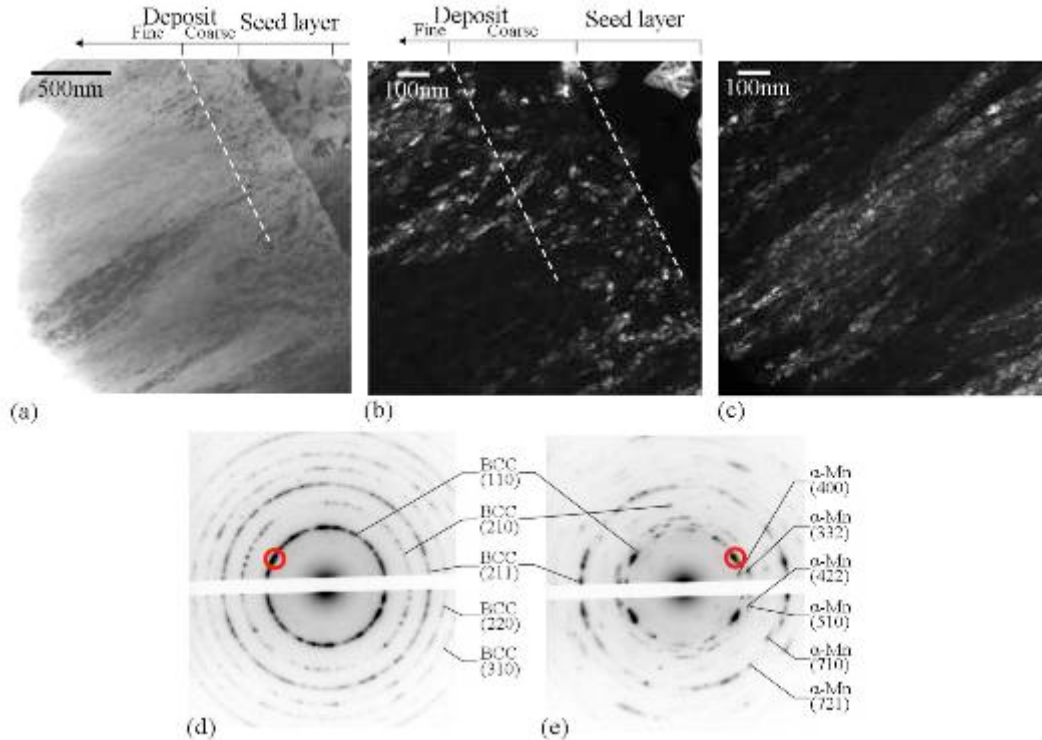
**Figure 4-30:** TEM micrographs and electron diffraction patterns from two grains formed in the reacted region of the silicon substrate after annealing at  $\sim 390^\circ\text{C}$ : (a) bright field image showing several grains (bright contrast) in the reacted region, (b) bright field image showing a dark grain in the reacted region, (c) electron diffraction pattern from the light grain at the centre of (a) identified as  $(\text{Co,Fe})\text{TiSi}$  and (d) electron diffraction pattern from the dark grain at the centre of (b) identified as gold.

#### 4.3.3.2 TEM analysis of deposits plated at $60^\circ\text{C}$ after annealing

TEM micrographs and electron diffraction patterns taken from a deposit plated at  $60^\circ\text{C}$  and annealed at  $\sim 174^\circ\text{C}$  are shown in Figure 4-31. The bright field micrograph (Figure 4-31 (a)) shows that after annealing at  $\sim 174^\circ\text{C}$ , the two

distinct morphological regions next to the seed layer and in the bulk deposit are still apparent. The dark field micrograph of the region next to the seed layer (Figure 4-31 (b)) indicates that the grain structure in this region is very similar to the corresponding region in the as-deposited film. The grains are still randomly orientated, and the grain size still ranges from ~10-20nm. The electron diffraction pattern taken from this region, however, shows that the original  $\alpha$ -Mn type phase, which comprised the entire deposit in the as-plated state, has completely transformed to the BCC phase. The dark field micrograph of the bulk deposit (Figure 4-31 (c)) shows that bands of similarly oriented grains are still aligned perpendicular to the substrate, but the bands are localized to discrete regions. These regions of preferred orientation are apparent in the electron diffraction pattern (Figure 4.3-11(e)) as well. The electron diffraction pattern also shows that transformation of the  $\alpha$ -Mn type phase to the BCC phase has begun, but is not complete in the bulk layer after 4 hours of annealing. These results indicate that the transformation either starts earlier near the seed layer or proceeds faster there than it does in the bulk deposit. This could be the result of heat gradients within the deposit; however, this is unlikely as the sample's surface would be expected to heat up faster than the seed layer as it was held in contact with the wall of the copper sample holder. It is still unclear as to why the transformation completes near the substrate before it completes in the bulk deposit.

Based upon some faint diffracted spots observed close to the centre spot in the electron diffraction patterns, there is evidence that  $\text{Fe}_3\text{O}_4$ , which was observed in other deposits, may also be present in the deposit. The proximity of strongly diffracting oxide rings and possible rings from the  $\alpha$ -Mn type phase makes it impossible to conclusively identify the oxide in the deposit.

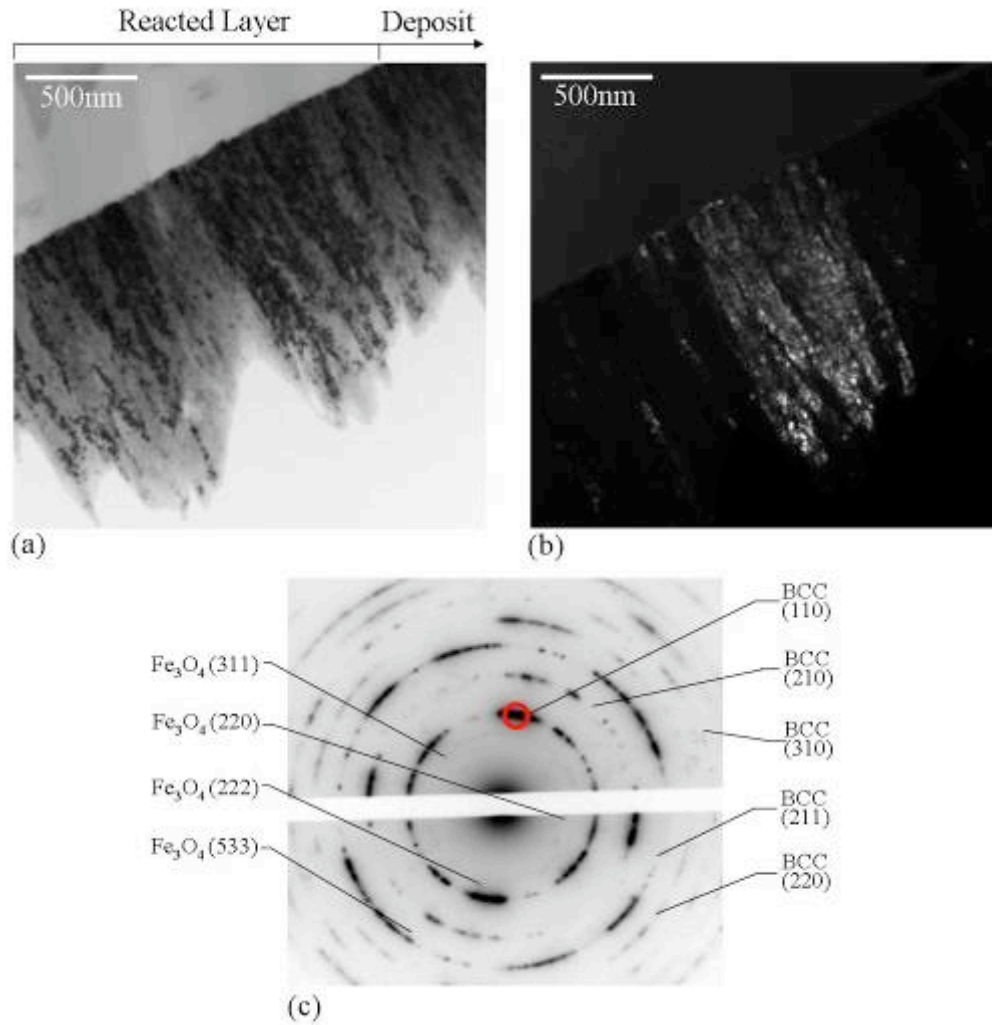


**Figure 4-31:** TEM micrographs and electron diffraction patterns from the cross-section of a deposit plated at 60°C and annealed at ~174°C: (a) bright field image, (b-c) dark field images near the seed layer and the deposit surface, respectively and (d-e) electron diffraction patterns from near the seed layer and the bulk deposit, respectively. The dark field images were taken using the portions of the electron diffraction rings denoted with red circles.

TEM micrographs and electron diffraction patterns taken from a deposit plated at 60°C and annealed at ~390°C are shown in Figure 4-32. The micrographs (Figure 4-31 (a-b)) show that after annealing at ~390°C the preferentially oriented regions observed in Figure 4-31 have widened and coarsened. There is no randomly orientated layer at the deposit's base like in the previous deposit. The grains which make up the deposit range from 20-30nm in size. The Au seed layer has apparently completely diffused into the substrate as it no longer appears in the micrographs. EDX analysis showed that no gold was present in the deposit itself. A reacted zone is visible in the bright field image (Figure 4-32 (a)) as faint grains within the former silicon substrate.

The electron diffraction pattern (Figure 4-32 (c)) confirms the XRD data and shows that the deposit has been completely transformed from the  $\alpha$ -Mn type

phase into the BCC phase. The incomplete rings in the electron diffraction pattern indicate the high amount of texture in the deposit which also confirms the XRD results. The preferred orientation observed in the BCC phase is likely a result of the phase forming from the textured  $\alpha$ -Mn type phase. In addition to the BCC phase, the  $\text{Fe}_3\text{O}_4$  phase was also detected in the deposit. This phase was also detected previously in other deposits, both annealed and unannealed. It is likely that this phase was present since the deposition of the thin-film but its presence was not verifiable due to the faintness of the pattern and its proximity to potential rings for the  $\alpha$ -Mn type phase. There exists the possibility that the  $\text{Fe}_3\text{O}_4$  phase forms as a result of oxidation during the annealing process. The presence of the  $\alpha$ -Mn type phase, however, prevents the conclusive identification of the  $\text{Fe}_3\text{O}_4$  phase in the unannealed samples, which makes the formation of the oxide during annealing difficult to corroborate.



**Figure 4-32:** TEM micrographs and electron diffraction patterns from the cross-section of a deposit plated at 60°C and annealed at ~390°C: (a) bright field image, (b) dark field and (c) electron diffraction patterns from the bulk deposit. The dark field image was taken using the portion of the electron diffraction ring denoted with the red circle.

#### **4.4 Magnetic properties of iron-cobalt thin films**

Measurements of both the saturation flux densities and coercivities of iron-cobalt deposits were conducted using a super quantum interference device (SQUID) at Sun Yat-sen University, which is located in the People's Republic of China. The error bars that appear in this section represent the standard error of the results for both the annealing temperature and the magnetic property being measured. Unfortunately, in some cases, insufficient magnetic property data at particular experimental conditions made statistical analysis impossible. Therefore, some data points in the following figures do not have error bars along the y-axis. Reasons for insufficient data include: delamination of the films from their substrates, discovery of atypical phase structures after the magnetic measurement were taken or magnetic results which were not physically possible (measurement of a negative magnetic remanence for instance) and these measurements were, therefore, excluded from analysis.

Saturation flux density measurements are prone to larger amounts of error than coercivity measurements as their accuracy is dependent on an accurate estimation of the deposit volume. Since the deposits were thin films with large surface area to thickness ratios, the errors in the thickness measurements of the deposits contributes the most to the errors in the calculated volume. It has already been stated in Section 4.2.1.2 that the iron-cobalt deposits are not flat but concave, due to edge effects during the plating process, which makes accurate estimation of deposit thickness difficult. This adds to the errors associated with measurement of the saturation flux densities of the deposits.

In addition, estimation of the volume lost due to cracking and delamination also needs to be considered when estimating the volume of the deposits. Determination of this volume loss was done by weighing the substrates before and after electroplating and then again before and after annealing. In this way, it was possible to estimate the mass loss due to the annealing process. The volume loss was then estimated using the densities of the deposits. As the density

of thin films can vary significantly from that of bulk metals, the deposit density was estimated using the mass and volume of the original deposits. Estimates for the material loss due to cracking of the deposits are shown in Table 4-7.

**Table 4-7:** Estimated volume loss for iron-cobalt deposit due to cracking and delamination after annealing.

<b>Plating temperature (°C)</b>	<b>Annealing Temperature (°C)</b>	<b>Average Deposit Loss (%)</b>	<b>2* Std. Error (%)</b>
<b>20</b>	174	6.7	2.7
	225	10.1	1.2
	390	14.5	0.7
<b>40</b>	174	1.4	1.4
	225	10.5	7.9
	390	4.2	2.1
<b>60</b>	174	0.0	n/a
	225	6.3	2.7
	390	---	---

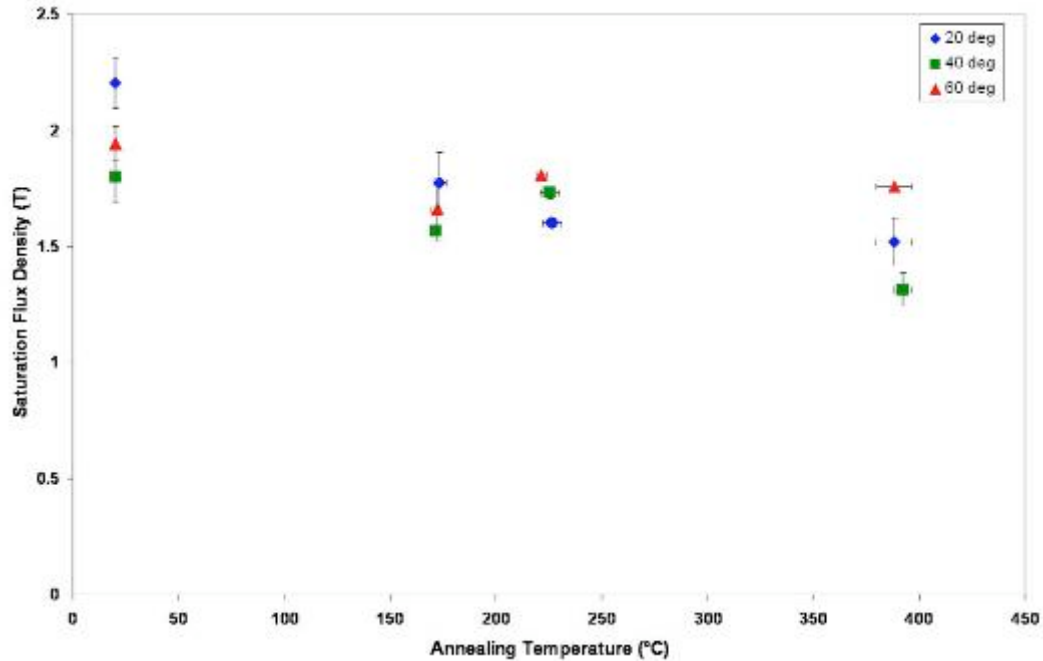
Based on the calculations, the volume loss was most severe in deposits plated at 20°C and least severe for deposits plated at 60°C. The volume loss from deposits plated at 60°C and annealed at ~390°C is not shown because these deposits appeared to gain volume based on the calculations. This is clearly impossible, and is probably due to inaccuracies in estimating the thickness, and thus the density, of the deposits at 60°C as these deposits tended to have less uniform thicknesses across their surfaces. Oxidation of the deposits during annealing is also a possible reason for the volume increase; however, as this effect was not seen in other deposits annealed at the same temperature, it is unlikely that oxidation played a major role. It was assumed for these deposits that no mass was lost for the sake of saturation flux density calculations. The material loss estimates for the deposits

plated at 40°C do not follow the expected trend i.e., that the largest amount of material would be lost at the highest annealing temperature. It is unclear as to why this result was obtained.

#### **4.4.1 Saturation flux density of iron-cobalt thin films**

The saturation flux densities of iron-cobalt deposits annealed without the application of an external magnetic field are shown in Figure 4-33. The results show that all of the deposits are magnetic despite the presence of the  $\alpha$ -Mn type phase in the deposits plated at elevated temperatures. The highest saturation flux densities were measured in the as-plated 20°C deposits. The average saturation flux density of these deposits was 2.2 T, which approximates the value that would be expected in bulk alloys with similar composition (Figure 2-25). Due to their lower iron contents, unannealed deposits plated at 40°C and 60°C should fall between 2 T and 2.2 T according to Figure 2-25; however, these values fell short of those expected from bulk alloys with similar compositions. The lower than expected saturation flux densities may be attributed to the presence of the  $\alpha$ -Mn type phase; however, after annealing at ~225°C to cause complete transformation of the  $\alpha$ -Mn type phase into the BCC phase no consistent difference in saturation magnetization was observed. The lower than expected values are, therefore, more likely due to the larger quantities of non-magnetic precipitates that are believed to be incorporated into the films when plated at elevated temperatures. It is curious that the deposits plated at 60°C had higher saturation flux densities than deposits plated at 40°C, despite the lower iron contents of the films. At present the higher saturation flux densities displayed by the deposits plated at 60°C (than 40°C) cannot be explained.



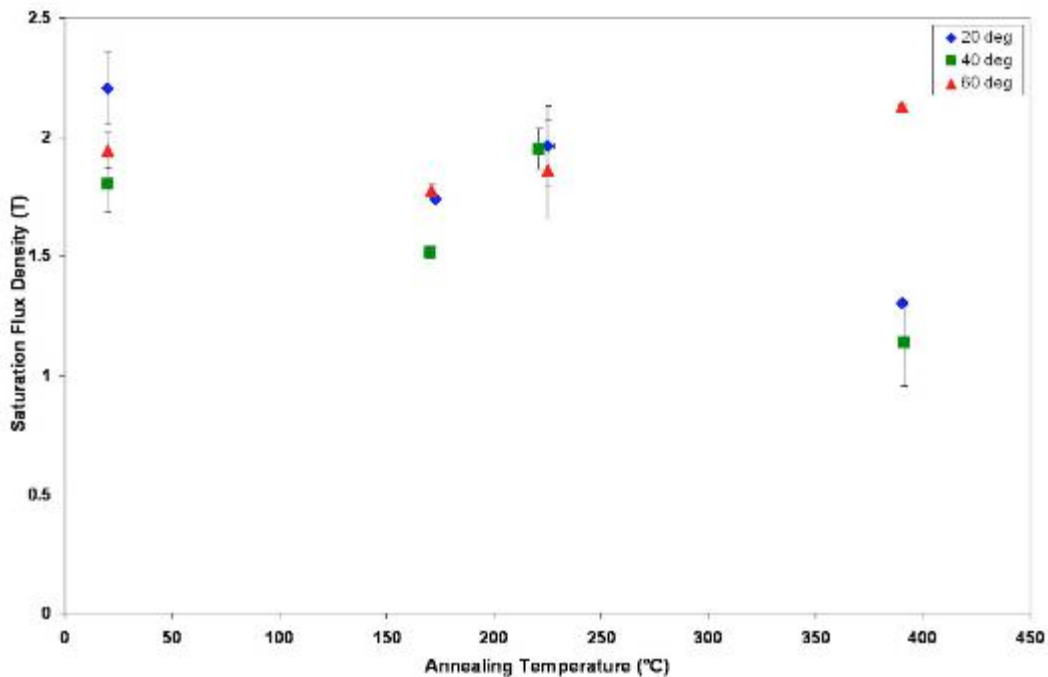


**Figure 4-33:** Saturation magnetic flux densities for iron-cobalt deposits plated at various temperatures, using the standard plating solution and parameters, after being annealed at various temperatures in the absence of an external magnetic field.

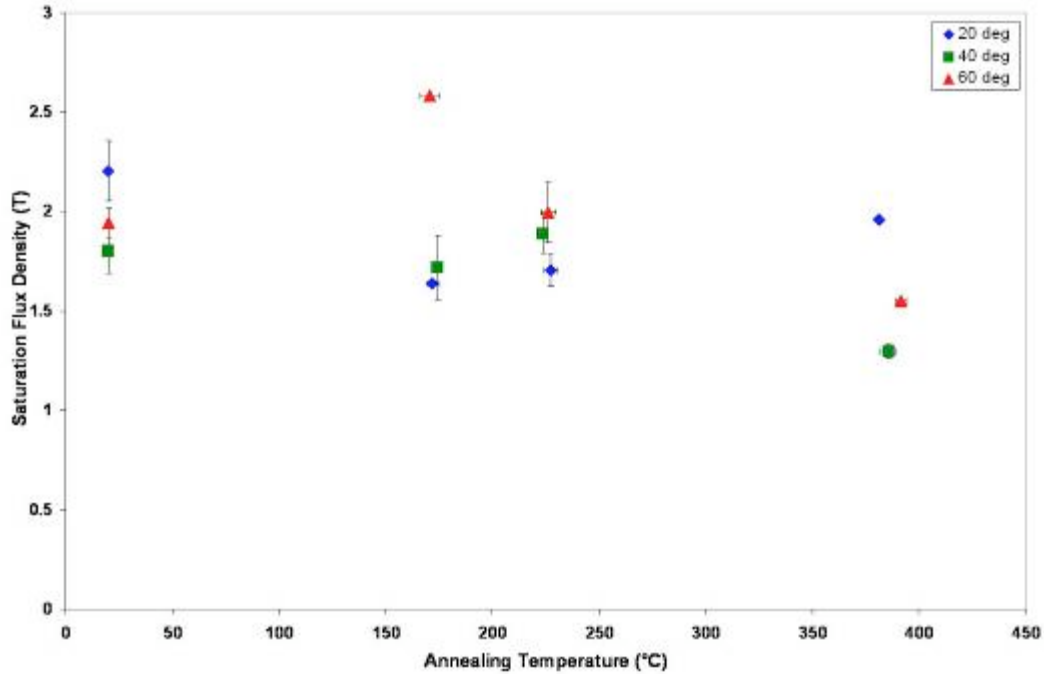
Annealing resulted in a decrease in the saturation magnetization values for iron-cobalt deposits plated at all temperatures. The deposits plated at 20°C showed the greatest drop in saturation flux density. These deposits experienced a significant drop in saturation flux density even after being annealed at the lowest annealing temperature tested, ~174°C. This is probably due to larger amounts of material loss due to cracking in these deposits during the annealing process. The deposits plated at 40°C and 60°C suffered from less severe cracking than the deposits plated at 20°C, which explains the less severe drop in their saturation flux densities after annealing. The drop in saturation flux densities of deposits annealed at ~390°C are likely exacerbated by reactions between the iron-cobalt deposits and the substrates, as evidenced by the presence of non-magnetic FeTiSi, which was detected using electron diffraction (Section 4.3.3) in the reacted layer of the silicon substrate when the deposit was annealed at this temperature.

The saturation flux densities of iron-cobalt deposits annealed under the

influence of an external magnetic field are shown in Figure 4-34 and Figure 4-35. It is difficult to discern any trends regarding the strength of the applied magnetic field on the saturation flux densities of iron-cobalt deposits. The same general trend as for deposits annealed without an external magnetic field was observed; a decrease in saturation flux density occurred as the annealing temperature was increased. There appears, however, to be a great deal of inconsistency between the saturation flux density values in the figures. Anomalously high values were measured in deposits plated at 60°C in two instances, Figure 4-34 at ~390°C and Figure 4-35 at ~174°C. For both cases, only one measurement was made, so the results could not be confirmed. The scatter and inconsistencies for the results in Figure 4-33, Figure 4-34 and Figure 4-35 prevents the formation of any clear conclusions regarding the effects of the applied magnetic field on the saturation flux densities of iron-cobalt deposits.



**Figure 4-34:** Magnetic saturation flux densities for iron-cobalt deposits plated at various temperatures, using the standard plating solution and parameters, after being annealed at various temperatures in a 500 Oe external magnetic field.

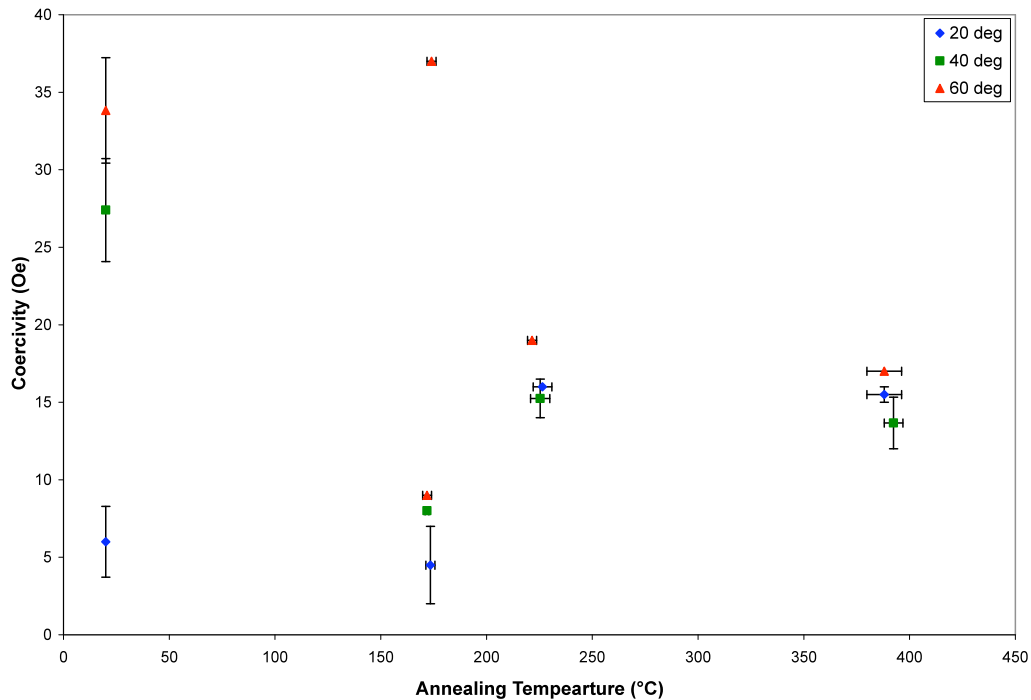


**Figure 4-35:** Magnetic saturation flux densities for iron-cobalt deposits plated at various temperatures, using the standard plating solution and parameters, after being annealed at various temperatures in a 2500 Oe external magnetic field.

#### 4.4.2 Coercivity of iron-cobalt thin films

The coercivities of iron-cobalt deposits annealed without the application of an external magnetic field are shown in Figure 4-36. The results show that in their as-deposited states, higher plating temperatures produced deposits with lower coercivities. The deposit plated at 20°C had an average coercivity of 6 Oe, while deposits plated at 40°C and 60°C had average coercivity values of 27 Oe and 34 Oe, respectively. The deposit plated at 20°C is entirely single phase (BCC), while the deposit plated at 60°C is also single phase but the  $\alpha$ -Mn type phase. The deposit plated at 40°C consists of a mixture of the two phases. It seems reasonable then that the BCC phase has a much lower coercivity than the  $\alpha$ -Mn type phase. This conclusion is borne out in the annealing results. Annealing of the deposits at ~174°C led to a significant reduction in the coercivities of the higher temperature deposits (40°C and 60°C), but only a slight reduction in the

coercivities of deposits plated at 20°C. The decrease in coercivity for the 40°C and 60°C samples is likely due to the partial transformation to the BCC phase. After 4 hours of annealing, XRD results indicate that the deposits plated at 40°C were almost completely composed of the BCC phase (Figure 4-23). As a consequence, the coercivities of these deposits dropped to a level similar to the original coercivities of deposits plated at 20°C. The coercivities of deposits plated at 60°C also dropped when annealed at ~174°C; however, since the transformation to the BCC phase is not complete under these conditions (Figure 4-24), the coercivities did not drop to the same level as the deposits plated at 40°C. In addition, a great deal of variation in the coercivities of deposits plated at 60°C and annealed at ~174°C was apparent, as shown by the two widely spaced data points that were annealed under this condition (Figure 4-36). The large difference between the two points is a result of some deposits showing no change in coercivity after annealing and others having their coercivities significantly reduced to a value slightly higher than that of the deposits plated at 40°C and annealed under similar conditions. This indicates that some deposits underwent partial transformation to the BCC phase and, thus, their coercivities decreased. Other deposits underwent no phase change and their coercivities remained high. That some deposits underwent a phase change and others did not could indicate that the phase transformation took longer to initiate in some samples. This indicates that the amount of phase change was variable for this annealing temperature. As the standard error of temperature for the annealing of these samples was less than 3°C, the extent of transformation of the  $\alpha$ -Mn type phase into the BCC phase must be very sensitive to annealing temperature under these conditions. A small decrease in coercivity was observed in deposits plated at 20°C. Since there was no phase transformation in these deposits, the decrease may be attributed to the so called “self magnetic annealing effect” which occurs in ferromagnetic materials even in the absence of an external magnetic field [Cullity72]. The effect is caused by directional ordering of atoms at elevated temperatures due to the presence of internal magnetic fields in the material.



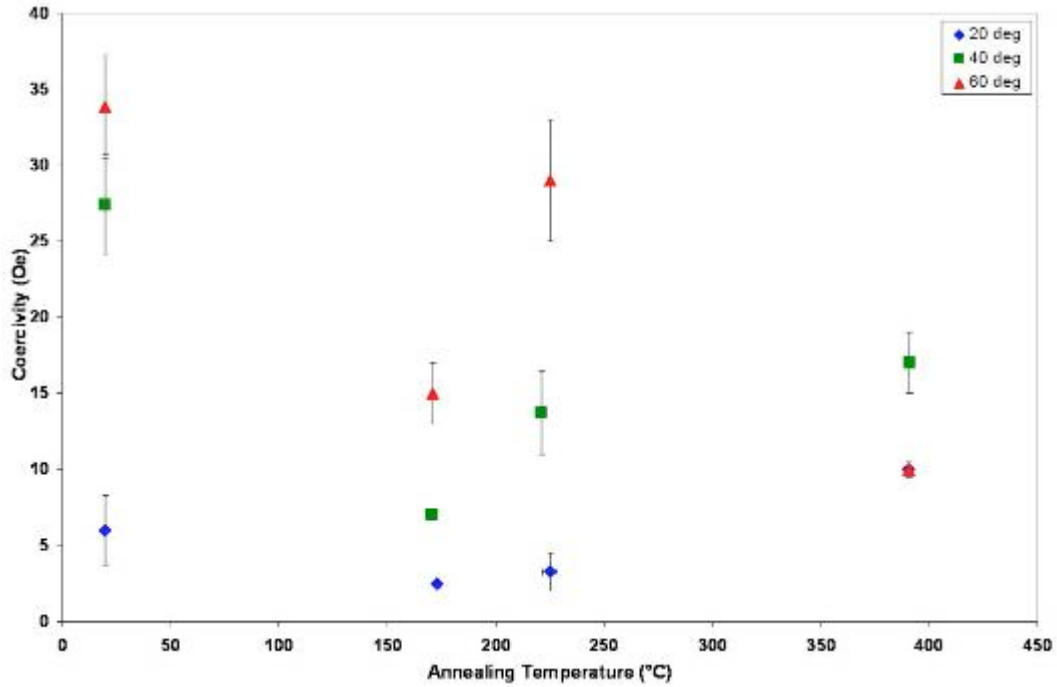
**Figure 4-36:** Coercivities for iron-cobalt deposits plated at various temperatures, using the standard plating solution and parameters, after being annealed at various temperatures in the absence of an external magnetic field.

Annealing at  $\sim 245^{\circ}\text{C}$  increased the coercivities of all the deposits to values between 15 Oe and 20 Oe. There was no significant change in coercivity values when the annealing temperature was increased further to  $\sim 390^{\circ}\text{C}$ . The similarity in coercivity values shown by all deposits regardless of plating temperature shows that the coercivities of the deposits are mostly related to the identity of the phases which are present. Deposits annealed for 4 hours at  $\sim 245^{\circ}\text{C}$  and above are completely composed of the BCC phase. The uniform increase in coercivity of the deposits when annealed above  $\sim 174^{\circ}\text{C}$  is likely due to the coarsening of the grain structure, which was corroborated using TEM in Section 4.3.3.

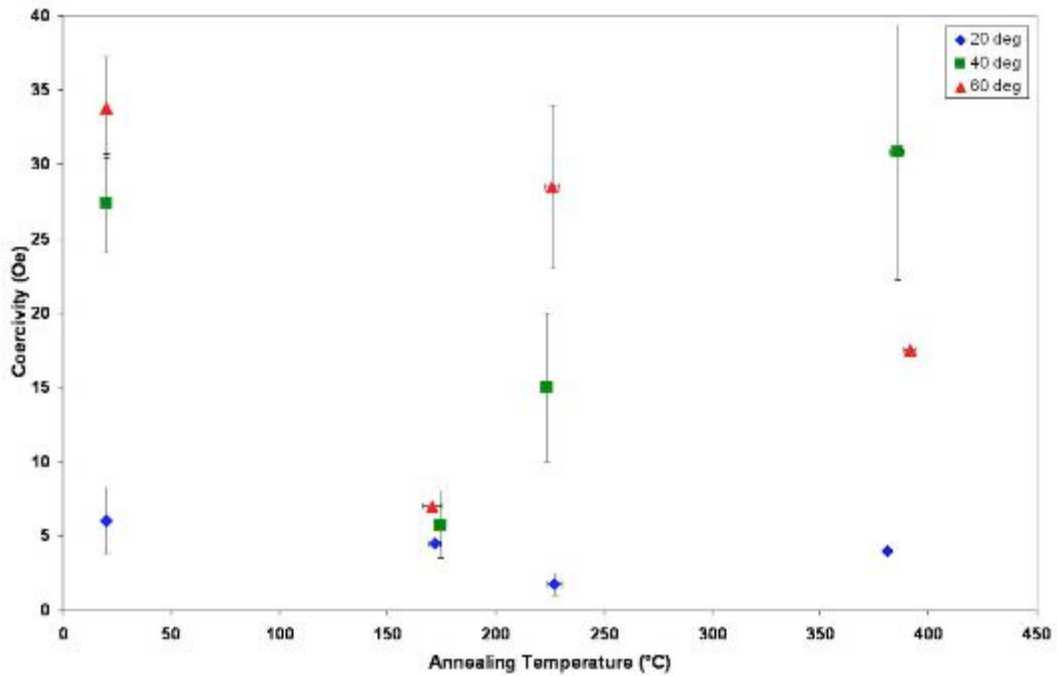
The coercivities of deposits annealed under the influence of external magnetic fields are shown in Figure 4-37 and Figure 4-38. The results show that the presence of an external magnetic field during annealing appears to improve the coercivities of deposits plated at  $20^{\circ}\text{C}$  when annealed at temperatures above

~174°C. When an external field of 500 Oe was applied, deposits plated at 20°C did not experience a substantial increase in coercivity until ~390°C, and the coercivity of the deposits did not increase substantially over the entire annealing range when an external field of 2500 Oe was used. The increase in coercivity experienced by the deposits when annealed without an external magnetic field was previously attributed to a coarsening of the deposit's grain structure. This behaviour is in agreement with the work of Herzer et al. [Herzer90] who predicted that in nano-sized grains the coercivity varies with grain size ( $D$ ) by a factor of  $D^6$ . Sharpening of the peaks in the XRD patterns of these deposits confirms that the coarsening still occurs in the deposits at these temperatures regardless of the presence of an external magnetic field (Section 4.3.2.2). Since the coercivities did not increase despite a coarsening of the deposit microstructure, magnetic ordering in the deposits as a result of the applied magnetic fields likely compensated for any loss of coercivity due to grain growth [Cullity72, Herzer89, Herzer90, Liu00, Osaka07].

Applied magnetic fields during annealing appear to have less effect on the coercivities of the deposits plated at 40°C and 60°C. Deposits plated at these temperatures still experienced an increase in coercivity when annealed at temperatures above ~174°C, unlike the deposits plated at 20°C as was previously described. The deposits plated at 40°C and 60°C also showed much more variation in coercivity after magnetic annealing as indicated by the large error bars in Figure 4-37 and Figure 4-38. When annealed at ~245°C, the applied magnetic field appears to cause a larger increase in the coercivities of the deposits plated at 40°C and 60°C. This increase is substantially larger for the deposits annealed at 60°C. There does not, however, appear to be any trend between the coercivities of deposits plated at 40°C and 60°C when annealed at ~390°C under a magnetic field.



**Figure 4-37:** Coercivities of iron-cobalt deposits plated at various temperatures, using the standard plating solution and parameters, after being annealed at various temperatures in a 500 Oe external magnetic field.

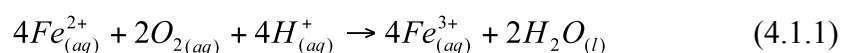


**Figure 4-38:** Coercivities of iron-cobalt deposits plated at various temperatures, using the standard plating solution and parameters, after being annealed at various temperatures in a 2500 Oe external magnetic field.

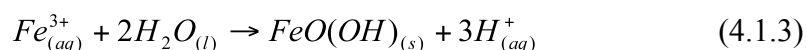
## Chapter 5 Conclusions and Recommendations for Future Work

### 5.1 Summary of research results and conclusions

Ammonium citrate had previously been reported to be an effective agent for stabilizing iron-cobalt plating solutions by preventing the formation of precipitates and therefore extending the useful life of the solution [Zhang04,Zhang07]. While it was confirmed that the addition of dibasic ammonium citrate significantly delayed the formation of precipitates in the solutions, visual examination and UV-visual spectroscopy showed that the solutions had a measureable change in colour, from a pink to an orange hue, after only 1 day. The colour change intensified as the solution aging time was lengthened, eventually resulting in the solution with a deep red colour and observable precipitates. The colour change was also accompanied by a decrease in solution pH. The initial colour change from pink to orange appeared to result from the oxidation of iron ions in the solution, from iron(II) to iron(III), due to the presence of dissolved oxygen. As dissolved oxygen is required for the oxidation of the iron(II), it was found that limiting contact between the solution and the atmosphere significantly improved the long term stability of the solutions. After significant aging the solution obtained a deep red colour, which was attributable to the formation of precipitates in the solution. The precipitates were identified using XPS as primarily  $\beta$ -FeO(OH) (akaganeite) with small quantities of Fe<sub>3</sub>O<sub>4</sub> (magnetite). A likely mechanism for the colour change and precipitate formation in the iron-cobalt solutions is:

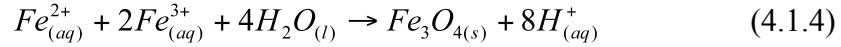


followed by:



and





Solution stability was shown to be further reduced by increases in temperature and the application of voltage across the solution. These effects are cumulative and result in significant aging effects even in fresh solutions after electroplating. This likely results in the incorporation of larger amounts of precipitates into the iron-cobalt deposits after electroplating at elevated temperatures.

Iron-cobalt deposits plated from a dibasic ammonium citrate plating solution typically had very smooth surfaces and were very compact and uniform through their thickness. The thickness of the deposits tended to increase slightly in response to increases in plating temperature. This was attributable to the lower overpotentials necessary for plating at higher temperatures. The lower plating overpotentials were also likely the reason that deposits plated at elevated temperatures showed less cracking than deposits plated at room temperature because of lower residual stress.

The composition of the deposits was found to be influenced by the plating temperature. It had been previously established that iron deposits preferentially at room temperature despite cobalt's higher reduction potential [Liao87, Bretazzoli93, Liu00, Zhou09]. This "anomalous" plating behaviour is counteracted when the plating temperature is increased. Plating at 20°C led to deposits which were iron-rich, plating at 40°C produced deposits with metal ratios similar to the metal ion ratio of the solution and deposits plated at 60°C were cobalt-rich. XPS analysis indicated that increasing plating temperature also led to a small increase in oxygen content in the deposits. This oxygen increase likely reflected a higher quantity of iron oxide precipitate incorporated into the deposits during the plating process.

The phase structure of the electrodeposited alloys was found to be greatly influenced by the temperature and pH of the electroplating solution, as well as by the presence of stabilizing agents. The standard dibasic ammonium citrate plating solution, used at its natural pH of 3.5, produced deposits composed of the equilibrium BCC phase at room temperature. As the plating temperature was increased in the region between 30°C and 40°C, the equilibrium BCC phase was

codeposited along with a metastable phase which is isostructural to  $\alpha$ -Mn. When the temperature was increased further, the proportion of the film which was deposited as the  $\alpha$ -Mn type phase gradually increased until it eventually replaced the BCC phase at some temperature between 50°C and 60°C. Deposits plated from plating solutions without the dibasic ammonium citrate stabilizer, used at an adjusted pH of 3.5, were the  $\alpha$ -Mn type phase at room temperature. As the plating temperature was increased, the  $\alpha$ -Mn type phase was gradually replaced by metastable HCP and  $\Omega$ -HCP phases. When plated at 60°C, the  $\beta$ -FeO(OH) phase was also detected. If the pH of either of the plating solutions, with and without dibasic ammonium citrate, was adjusted to 2.3 the equilibrium BCC phase was the only phase that is deposited.

The mechanism for metastable phase formation is unknown, however, it is suspected that the phases may result from residual stresses, which could result from the inclusion of precipitates in the deposits during deposition. High temperature and pH likely promoted the formation of the metastable phases by increasing reaction kinetics and provided ample hydroxyl ions for the formation of precipitates. Dibasic ammonium citrate appeared to partially stabilize the electroplating solution, but the amount was insufficient for complete stabilization of the solution at elevated temperatures.

Higher current densities were found to increase the relative amount of BCC phase deposited in deposits plated at 40°C. As conventional theory predicts that increased current densities should promote the deposition of metastable phases, further study is necessary to determine the reason for this behaviour.

Annealing of the deposits at temperatures greater than  $\sim 174^\circ\text{C}$  led to substantial cracking of the deposits, with the severity of cracking increasing with temperature. The cracking was most severe for deposits plated at 20°C and 60°C. Cracking was largely attributed to the differential thermal expansion of the deposit, substrate and seed layer. Deposits plated at 20°C already showed evidence of cracking when plated and this was likely enhanced during annealing. It was speculated that the substantial cracking in the deposits plated at 60°C was due to residual stresses, which result from the incorporation of precipitates in the

deposit. The deposits remained well adhered to the substrate when annealed at temperatures up to 225°C. When deposits were annealed at 390°C, the films tended to delaminate and bow away from the substrate. Inter-diffusion and reactions between the substrate, seed layer and deposit were also observed when annealing was conducted at ~390°C. Electron diffraction was used to identify one of the phases formed as (Co,Fe)TiSi, which indicates that some of the deposit is consumed in the reactions.

TEM analysis showed that deposits plated from the dibasic ammonium citrate stabilized plating solution had very fine-grained microstructures, typically less than 20nm. Deposits plated at 20°C were composed of randomly oriented grains which range from ~5-20nm in size in the bulk of the deposit, but range from ~10-40nm near the seed layer. Annealing of these deposits did not result in any change in phases or texture; however, coarsening of the grain structure was observed after annealing at ~390°C for 4 hrs.

Deposits plated at 40°C also showed two distinct morphological regions through the deposits cross-section. A narrow band of deposit near the seed layer was made up of randomly oriented grains which were ~5-20nm in size. Electron diffraction analysis showed that the only phase present in this layer was the BCC phase. The  $\alpha$ -Mn type phase was only detected in the bulk of the deposit, along with the BCC phase. The deposit bulk was composed of equally fine grains; however, these grains appeared to have some degree of preferred orientation. This was shown in dark field images as grains aligned with other similarly orientated grains perpendicular to the seed layer. This morphology was much more dominant in the deposits plated at 60°C, which were composed of only the  $\alpha$ -Mn type phase. The reason for the formation of this particular microstructure is unclear; however, it is suspected that the microstructure may be related to the recrystallisation of the deposit at some point after deposition. Recrystallization may be caused by strain effects in the deposits due to the incorporation of impurities during electroplating. That the deposits plated at 40°C initially form as only the BCC phase could reflect the lag in time between the start of plating and

the formation and incorporation of precipitates into the deposit.

Annealing of deposits at 174°C for 4 hours caused the almost complete transformation of the  $\alpha$ -Mn type phase into the BCC phase in the deposits plated at 40°C and a partial transformation of the  $\alpha$ -Mn type phase in deposits plated at 60°C. Annealing of the deposits at 225°C for 4 hours caused the complete transformation of the  $\alpha$ -Mn type phase into the BCC phase in all deposits. As a result of the initial texture of the  $\alpha$ -Mn type phase, the BCC phase that formed from it during annealing was also heavily textured, as evidenced by the lack of BCC(200) peak in the XRD patterns taken from transformed deposits. When annealed at 390°C, deposits plated at 60°C considerably coarsened to a grain size of 20-40nm. The presence of an external magnetic field during annealing did not appear to have any effect on the texture and phase transformation in the deposits.

In addition to the iron-cobalt phases that were detected using XRD, trace amounts of Fe<sub>3</sub>O<sub>4</sub> were detected by XRD. The oxide was typically only detectable in deposits that had only the BCC phase, as the strongest Fe<sub>3</sub>O<sub>4</sub> rings were overlapped the  $\alpha$ -Mn type phase rings. It is likely, however, that oxide was present in all deposits.

Magnetic measurements of the as-deposited films showed that the deposits plated at 20°C displayed the highest average saturation flux densities at 2.2T. This value is in the range expected for a bulk alloy with a similar composition. Deposits plated at 40°C and 60°C had saturation flux density values of ~1.8T and ~1.9T, respectively; these were lower than those expected for bulk alloys with their compositions. This is likely due to the presence of non-magnetic precipitates, which were incorporated into the deposits plated at elevated temperatures. The presence of the  $\alpha$ -Mn type phase did not appear to affect the saturation flux densities of the deposits, as no significant difference was seen after the transformation of the phase.

The saturation flux density measurements taken from the annealed deposits were erratic and definite trends using the data were hard to identify. The problem stems from saturation flux density's dependence on accurate

measurement of the deposit's volume in conjunction with cracking and delamination of the deposits during annealing. The saturation flux densities of the deposits tended to decrease as the annealing temperature increases. The largest drop in saturation flux density was observed in deposits plated at 20°C; the saturation flux density decreased by ~0.7T after annealing at ~390°C. These deposits also experienced the most severe cracking and delamination after annealing. No clear trends between the presence of an external magnetic field during annealing and the saturation flux densities of the deposits were observed.

Coercivity measurements of iron-cobalt deposits showed that the presence of the  $\alpha$ -Mn type phase causes deposits to display higher coercivities. Deposits plated at 20°C had an average coercivity of 6 Oe, while deposits plated at 40°C and 60°C had average coercivity values of 27 Oe and 34 Oe, respectively. Annealing of deposits containing the  $\alpha$ -Mn type phase at ~174°C, and hence the transformation of the phase to the BCC phase, led to a significant reduction in coercivities of the deposits to ~8.5 Oe. Annealing of deposits which did not contain the  $\alpha$ -Mn type phase at ~174°C resulted in only slight improvement to coercivity to 4.5 Oe, which is attributable to the self magnetic annealing effect. When annealing at temperatures higher than 174°C in the absence of an external magnetic field all the deposits had their coercivities increased to ~15-20 Oe. This was attributed to the coarsening of the grain structure of the deposits, which was corroborated using TEM.

The application of an external magnetic field during annealing was found to improve the coercivities of deposits plated at 20°C when annealed at higher temperatures. When an external field of 500 Oe was applied, the deposits did not experience a substantial increase in coercivity until ~390°C. When an external field of 2500 Oe was used the coercivity of the deposits did not increase substantially over the entire annealing range. This effect was attributed to the influence of magnetic annealing which acts in opposition to the coarsening of the deposits' grain structure when annealed at elevated temperatures. Deposits plated at 40°C and 60°C still underwent a significant increase in coercivity when annealed at temperatures above ~174°C despite the application of an external

magnetic field. These deposits had much more variability in their coercivity values making it difficult to determine any trends.

The major conclusions from this work are given as follows:

- The standard dibasic ammonium citrate stabilized plating solution is prone to oxidation by dissolved oxygen, which initially causes iron(II) to oxidize to iron(III) and eventually leads to the formation of FeO(OH) and Fe<sub>3</sub>O<sub>4</sub> precipitates.
- The stability of the standard dibasic ammonium citrate plating solution is reduced by increasing temperature and the application of a voltage across the cell.
- Room temperature plating produces deposits which are anomalously cobalt-poor. However, higher temperatures promote the deposition of cobalt over iron resulting in cobalt-rich deposits when plated at 60°C.
- The oxygen content of deposits increases with increasing plating temperature, with up to 4.5 at%O at 60°C, indicating the incorporation of greater quantities of oxide/hydroxide precipitates.
- The phase structure of the electrodeposited alloys is greatly influenced by the plating temperature, as well as the pH and presence of stabilizing agents in the plating solution.
  - The presence of dibasic ammonium citrate promotes the deposition of the equilibrium BCC phase. In the absence of dibasic ammonium citrate the metastable  $\alpha$ -Mn type phase is deposited at room temperature, and the metastable HCP and dHCP phases are deposited at higher temperatures.
  - Elevated plating temperatures promote the deposition of metastable phases. In the dibasic ammonium citrate stabilized plating solution this translates to the BCC phase being deposited at room temperature and the metastable  $\alpha$ -Mn type phase being deposited when plating is done at 60°C.

- Lowering the pH of the plating solution to 2.4 prevents the deposition of the metastable phases at any temperature.
- The formation of metastable phases may be attributable to the incorporation of precipitates into the deposits during electrodeposition.
- Increasing the current density during deposition has the effect of promoting the deposition of the equilibrium BCC phase over the deposition of metastable phases.
- Deposits plated from the dibasic ammonium citrate plating solution are typically fine grained (<40nm) and are generally quite flat and compact through their thickness.
- Deposits plated from the dibasic ammonium citrate stabilized plating solution contain both the BCC and  $\alpha$ -Mn type phases; the BCC phase forms initially. The  $\alpha$ -Mn type phase is codeposited along with the BCC phase as the deposition process proceeds.
- The metastable  $\alpha$ -Mn type phase, plated from the dibasic ammonium citrate plating solution at elevated temperatures, is deposited with some degree of preferred orientation. This preferred orientation is conserved in the BCC phase which forms from the  $\alpha$ -Mn type phase during annealing. The application of an external magnetic field during annealing had no apparent effect on this behaviour.
- Deposits plated at room temperature show the greatest saturation magnetic flux densities at 2.2T. Deposits plated at elevated temperatures have lower than expected saturation flux densities, i.e., ~1.8T and ~1.9T for deposits plated at 40°C and 60°C, respectively. This may be due to the presence of precipitates in these deposits.
- Annealing of the deposits tends to lower their saturation flux densities and produces erratic measurements. This can be attributed to the loss of deposit due to cracking and delamination. The

application of a magnetic field during annealing has no obvious effect.

- The coercivity of deposits plated from the dibasic ammonium citrate stabilized plating solutions are dependent on the phases present in the deposit. The presence of the  $\alpha$ -Mn type phase greatly increases the coercivities of the deposits. Deposits plated at 40°C have coercivities of ~27 Oe and deposits plated at 60°C have coercivities of ~34 Oe. The coercivities of these deposits can be reduced to ~8.5 Oe through the transformation of the  $\alpha$ -Mn type phase to the BCC phase by annealing at ~174°C.
- Annealing of the deposits at temperatures greater than 225°C for 4 hours causes an increase in coercivity values in all deposits up to ~15-20 Oe. The application of a magnetic field during annealing reduces the effect in deposits plated at room temperature. An applied magnetic field has little discernable effect on deposits plated at 40°C and 60°C.



## 5.2 Recommendations for future work

Over the course of this research several areas which could merit further study were noted.

The first potential area of interest concerns an in-depth study of the stability behaviour of the iron-cobalt plating solution. A mechanism for the behaviours observed as the solution is aged was proposed in this thesis, involving a valence change in the iron(II) ions and the eventual precipitation of certain iron oxides. However, an in depth study of the plating solution chemistry as the solution is aged would be required to confirm or disprove this mechanism. This could involve titrimetry or the use of selective ion electrodes to monitor changes in solution chemistry.

This work indicated that higher current densities promoted the deposition of the BCC phase over the metastable  $\alpha$ -Mn type phase. This result seems to contradict established theory that suggests that higher current densities facilitate the deposition of metastable phases. This behaviour should be investigated to shed further light on the mechanism for the formation of these phases in general.

The nature of the metastable phases, which were deposited using the dibasic ammonium citrate plating solution, should be further explored. It was suggested here that these phases could form due to strain that results from the incorporation of precipitates into the deposits during the plating process. It was also suggested that these phases are the result of recrystallization which occurs after the initial deposition. These hypotheses, however, have not been confirmed. Measurement of deposit strain by analysis of XRD peak broadening could be used to confirm the presence of residual strain in the deposits. Also precipitates could be identified though more accurate oxygen quantification than was possible in this work, e.g., using wavelength dispersive spectrometry (WDS).

Curvature along deposit surfaces, due to edge effects, made the accurate determination of the deposit thicknesses difficult. In the future this effect could be reduced through the use of stirring or the use of a leveling agent.

Accurate determination of the saturation flux densities of the annealed deposits was greatly hampered in this investigation due to the cracking and delamination of the deposits during annealing, as well as the consumption of the deposit through reactions. Both issues are largely the result of incompatibilities between the deposits and the deposits/seed layers. Future work should use a substrate/seed layer with a thermal expansion coefficient that more closely matches that of the iron-cobalt deposits in order to limit the effects of thermal expansion on deposit integrity. Also substrates/seed layers which are non-reactive with the deposits should be selected to limit the consumption of the deposited layers through reactions.

## Appendix A

### Gibbs Free Energy Calculations

The standard Gibbs free energy for a given reaction can be calculated from the standard Gibbs free energies of formation of the products minus the standard Gibbs free energies of formation of the reactants. For each reactant and product the standard Gibbs free energy of formation must be multiplied by the relative number of moles for the reaction.

$$\Delta G_r^\circ = \sum n \cdot \Delta G_f^\circ(\text{prod.}) - \sum n \cdot \Delta G_f^\circ(\text{react.}) \quad (\text{A.1.1})$$

The standard Gibbs free energy of formation values used in these calculations are tabulated below.

**Table A-1:** Gibbs free energy of formation of chemical species  
[Alberty97<sup>a</sup>, Garrelts65, Diakonov94<sup>c</sup>]

Chemical Species	$\Delta G_f^\circ$ (kJ/mol)
<b>Fe<sup>2+</sup></b>	-78.9 [a]
<b>Fe<sup>3+</sup></b>	-4.7 [a]
<b>O<sub>2</sub></b>	0 [a]
<b>H<sup>+</sup></b>	0 [a]
<b>H<sub>2</sub>O</b>	-237.1 [a]
<b>Fe(OH)<sub>3</sub></b>	-695.0 [b]
<b>Fe<sub>3</sub>O<sub>4</sub></b>	-1015.4 [a]
<b>FeO(OH)</b>	-492.1 [c]

The Gibbs free energy under non-standard conditions is calculated using the equation:

$$\Delta G = \Delta G^\circ + RT \ln(Q) \quad (\text{A.1.2})$$

where R is the ideal gas constant, T is the absolute temperature and Q is the reaction quotient. In this analysis the activity of hydrogen ions are assumed to be equal to the hydrogen concentration in the acidic solution. The activities of all other species are equal to unity.

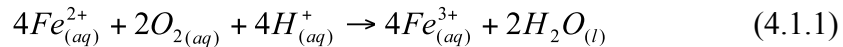
Assuming pH=3.5 and standard states for all species other than H<sup>+</sup>:

$$pH = -\log([H^+])$$

$$[H^+] = 10^{-3.5}$$

$$[H^+] = 3.162 \times 10^{-4} \text{ mol/L}$$

Reaction:



$$\begin{aligned} \Delta G_r^o &= \sum n \cdot \Delta G_f^o(\text{prod.}) - \sum n \cdot \Delta G_f^o(\text{react.}) \\ &= 4 \times (-4.7 \text{ kJ/mol}) + 2 \times (-237.1 \text{ kJ/mol}) - \\ &\quad [4 \times (-78.9 \text{ kJ/mol}) + 2 \times (0 \text{ kJ/mol}) + 4 \times (0 \text{ kJ/mol})] \\ \Delta G_r^o &= -177.5 \text{ kJ} \end{aligned}$$

$$\Delta G = \Delta G^o + RT \ln(Q)$$

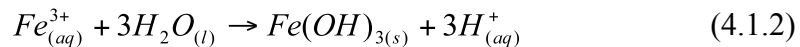
$$\Delta G = \Delta G^o + RT \ln \left( \frac{[H_2O][Fe^{3+}]}{[Fe^{2+}][H^+][O_2]} \right)$$

$$\Delta G = \Delta G^o + RT \ln \left( \frac{1}{[H^+]} \right)$$

$$= -177.5 \text{ kJ} + (0.008314 \frac{\text{kJ}}{\text{K}})(298 \text{ K}) \ln \left( \frac{1}{[3.162 \times 10^{-4}]} \right)$$

$$\Delta G = -97.6 \text{ kJ}$$

Reaction:



$$\Delta G_r^o = \sum n \cdot \Delta G_f^o(\text{prod.}) - \sum n \cdot \Delta G_f^o(\text{react.})$$

$$= 1 \times (-695.0 \text{ kJ/mol}) + 3 \times (0 \text{ kJ/mol}) - [1 \times (-4.7 \text{ kJ/mol}) + 3 \times (-237.1 \text{ kJ/mol})]$$

$$\Delta G_r^\circ = 21.5 \text{ kJ}$$

$$\Delta G = \Delta G^\circ + RT \ln(Q)$$

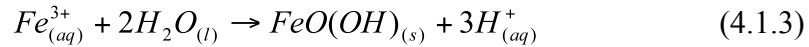
$$\Delta G = \Delta G^\circ + RT \ln \left( \frac{[Fe(OH)_3][H^+]}{[Fe^{3+}][H_2O]^3} \right)$$

$$\Delta G = \Delta G^\circ + RT \ln [H^+]$$

$$= 21.5 \text{ kJ} + (0.008314 \frac{\text{kJ}}{\text{K}})(298 \text{ K})(\ln [3.162 \times 10^{-4}])$$

$$\Delta G = -38.4 \text{ kJ}$$

Reaction:



$$\Delta G_r^\circ = \sum n \cdot \Delta G_f^\circ(\text{prod.}) - \sum n \cdot \Delta G_f^\circ(\text{react.})$$

$$= 1 \times (-492.1 \text{ kJ/mol}) + 3 \times (0 \text{ kJ/mol}) - [1 \times (-4.7 \text{ kJ/mol}) + 2 \times (-237.1 \text{ kJ/mol})]$$

$$\Delta G_r^\circ = -13.1 \text{ kJ}$$

$$\Delta G = \Delta G^\circ + RT \ln(Q)$$

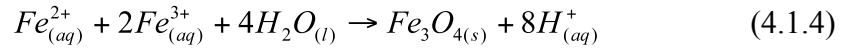
$$\Delta G = \Delta G^\circ + RT \ln \left( \frac{[FeO(OH)][H^+]}{[Fe^{3+}][H_2O]^2} \right)$$

$$\Delta G = \Delta G^\circ + RT \ln [H^+]$$

$$= -13.1 \text{ kJ} + (0.008314 \frac{\text{kJ}}{\text{K}})(298 \text{ K})(\ln [3.162 \times 10^{-4}])$$

$$\Delta G = -73.0 \text{ kJ}$$

Reaction:



$$\begin{aligned} \Delta G_r^\circ &= \sum n \cdot \Delta G_f^\circ(\text{prod.}) - \sum n \cdot \Delta G_f^\circ(\text{react.}) \\ &= 1 \times (-1015.4 \text{ kJ/mol}) + 8 \times (0 \text{ kJ/mol}) - \\ &\quad \left[ 4 \times (-237.1 \text{ kJ/mol}) + 2 \times (-4.7 \text{ kJ/mol}) \right] \\ &\quad \left[ + 1 \times (-78.9 \text{ kJ/mol}) \right] \end{aligned}$$

$$\Delta G_r^\circ = 21.42 \text{ kJ}$$

$$\Delta G = \Delta G^\circ + RT \ln(Q)$$

$$\Delta G = \Delta G^\circ + RT \ln \left( \frac{[Fe_3O_4][H^+]^8}{[Fe^{3+}]^2[Fe^{2+}][H_2O]^4} \right)$$

$$\Delta G = \Delta G^\circ + RT \ln([H^+]^8)$$

$$= 21.42 \text{ kJ} + \left( 0.008314 \frac{\text{kJ}}{\text{K}} \right) (298 \text{ K}) (\ln [3.162 \times 10^{-4}]^8)$$

$$\Delta G = -138.3 \text{ kJ}$$

## References

- [Alberty97] R.A. Alberty and R.J. Silbey, Physical Chemistry 2<sup>nd</sup> Edition, John Wiley and Sons: Toronto, 1997.
- [Andricacos98] P.C. Andricacos and N. Robertson, *IBM Journal of Research & Development*, **42**(5), 103 (1998).
- [Bacaltchuk03] C. M. B. Bacaltchuk, G. A. Castello-Branco, M. Ebrahimi, H. Garmestani and A.D. Rollett, *Scripta Materialia*, **48**(9), 1343 (2003).
- [Bauccio93] M. Bauccio eds., ASM Metals Reference Book Third Edition, ASM International: Materials Park OH, 1993.
- [Baker92] H. Baker eds., ASM Handbook Volume 3 Alloy Phase Diagrams, ASM International: Materials Park, OH, 1992.
- [BBC07] “Factfile: Hard disk drive.” *BBC News* May 21, 2007. accessed: Feb. 24, 2009. <<http://news.bbc.co.uk/1/hi/technology/6677545.stm>>.
- [Betteridge82] W. Betteridge, Cobalt and its Alloys, Ellis Horwood: Chichester, 1982.
- [Bertazzoli93] R. Bertazzoli and D. Pletcher, *Electrochimica Acta*, **38**(5), 671 (1993).
- [Bonhôte02] C. Bonhôte, H. Xu, E.I. Cooper and L.T. Romankiw, *Electrochemical Society Proceedings*, **2002-27**, 319 (2002).
- [Bonhôte04] C. Bonhôte, J.W. Lam and M. Last, *Electrochemical Society Proceedings*, **2004-23**, 363 (2004).
- [Bonnenberg80] D. Bonnenberg and K.A. Hempel, “Part B: Spinels, Fe Oxides, and Fe-Me-O Compounds”, Landolt-Börnstein - Group III Condensed Matter Volume 12b, Springer-Verlag: Berlin, 1980.
- [Bozorth51] R.M. Bozorth, Ferromagnetism, D. Van Nostrand Company, Inc.: New York, NY, 1951.

- [Bradford01] S.A. Bradford, Corrosion Control 2<sup>nd</sup> edition, CASTI Publishing Inc.: Canada, 2001.
- [Brimingham09] Applied Alloy Chemistry Group, “Magnetic materials: Properties”, *University of Birmingham*. Accessed Feb. 24, 2009. <[http://www.magnets.bham.ac.uk/magnetic\\_materials/properties.htm](http://www.magnets.bham.ac.uk/magnetic_materials/properties.htm)>
- [Callister03] W.D. Callister Jr., Materials Science and Engineering: An Introduction 6<sup>th</sup> Edition, John Wiley and Sons Inc.: USA, 2003.
- [Cavallotti05] P.L. Cavallotti, L. Nobili and A. Vincenzo, *Electrochimica Acta*, **50**, 4557 (2005).
- [Chang90] J.W. Chang, P.C. Andricacos, B. Petek and L.T. Romankiw, *Proceedings of the Symposium on Magnetic Materials, Processes and Devices*, **PV90-8**, 361 (1990).
- [Chiu96] A. Chiu, I. Croll, D.E. Heim, R.E. Jones Jr., P. Kasiraj, K.B. Klaassen, C.D. Mee and R.G. Simmons, *IBM Journal of Research & Development*, **40**(3), 283 (1996).
- [Chopra69] K.L. Chopra, *Physica Status Solidi*, **32**(2), 489 (1969).
- [Cohen-Hyams04] T. Cohen-Hyams, J.M. Plitzko, C.J.D. Hetherington, J.L. Hutchison, J. Yahalom and W.D. Kaplan, *Journal of Materials Science*, **39**, 5701 (2004).
- [Computer06] *Computer Desktop Encyclopedia*. The computer language company Inc. 2006.
- [Cooper05] E.I. Cooper, C. Bonhôte, J. Heidmann, Y. Hsu, P. Kern, J.W. Lam, M. Ramasubramanian, N. Robertson, L.T. Romankiw and H. Xu, *IBM Journal of Research & Development*, **49**(1), 103 (2005).
- [Craik65] D.J. Craik and R.S. Tebble, Ferromagnetism and Ferromagnetic Domains, North-Holland Publishing Company: Germany, 1965.
- [Crystal04] Crystal Lattice Structures, “The  $\alpha$ Manganese (A12) Structure.”, *U.S. Naval research Laboratory*, Oct. 21, 2004. Accessed Mar. 24, 2009. <<http://cst-www.nrl.navy.mil/lattice/struk/a12.html>>



- [Cullity72] B.D. Cullity, Introduction to Magnetic Materials, Addison-Wesley Publishing Company, Inc.: Reading, MA, 1972.
- [Daniel98] E.D. Daniel, C.D. Mee and M.H. Clark, eds. Magnetic recording: The first 100 years, IEEE Press: New York, NY, 1999.
- [Dykonov94] I. Diakonov, I. Khodakovsky, J. Schott and E. Sergeeva, *European Journal of Minerals*, **6**(6), 967 (1994).
- [Garrelts65] R.M. Garrels and C.L. Christ, Solutions, Minerals, and Equilibria, Harper & Row: New York, 1965.
- [Gladstein02] M. Gladstein and H. Guterman, *Metal Finishing*, **100**(8), 26 (2002).
- [Gross99] M.E. Gross, R. Drese, C. Lingk, W.L. Brown, K. Evans-Lutterodt, D. Barr, D. Golovin, T. Ritzdorf, J. Turner and L. Graham, *Materials Research Society Symposium Proceedings*, **562**, 215 (1999).
- [Herzer89] G. Herzer, *IEEE Transactions on Magnetics*, **25**(5), 3327 (1989).
- [Herzer90] G. Herzer, *IEEE Transactions on Magnetics*, **26**(5), 1397 (1990).
- [Ibl80] N. Ibl, *Surface Technology*, **81**, 81 (1980).
- [Jay01] J.P. Jay, I-S. Jurca, G. Pourroy, N. Viart, C. Me'ny and P. Panissod, *Solid State Sciences*, **3**(3), 301 (2001).
- [Kakuno97] E.M. Kakuno, D.H. Mosca, I. Mazzaro, N. Mattoso, W.H. Schreiner and M.A.B. Gomes, *Journal of the Electrochemical Society*, **144**(9), 3222 (1997).
- [Kanani04] N. Kanani, Electroplating: Basic Principles, Processes And Practice, Elsevier: Oxford, UK, 2004.
- [Kaya28] S. Kaya, *Science Reports of Tohoku Univeristy*, **17**, 1157 (1928).
- [Liao87] S. Liao, *IEEE Transactions on Magnetics*, **MAG-23**(5), 2981 (1987).
- [Liu00] X. Liu, P. Evans and G. Zangari, *IEEE Transactions on Magnetics*, **36**(5), 3479 (2000).

- [Liu03] X. Liu, G. Zangari and M. Shamsuzzoha, *Journal of the Electrochemical Society*, **150**(3), C159 (2003).
- [Lottermoser07] B.G. Lottermoser, Mine Wastes: Characterization, Treatment and Environmental Impacts 2<sup>nd</sup> Edition, Springer: Berlin, 2007.
- [Lowenheim78] F. Lowenheim, Electroplating, McGraw-Hill Book Company: New York, NY, 1978.
- [Mallinson97] J. Mallinson, Magnetoresistive Heads: Fundamentals and Applications, Academic Press: San Diego, CA, 1997.
- [Martinez07] L. Martinez, D. Leinen, F. Martín, M. Gabas, J.R. Ramos-Barrado, E. Quagliata and E.A. Dalchieleb, *Journal of the Electrochemical Society*, **154**(3), D126 (2007).
- [Masahashi98] N. Masahashi, M. Matsuo and K. Watanabe, *Journal of Materials Research*, **13**(2), 457 (1998).
- [Mattoso01] N. Mattoso, V. Fernandes, M. Abbate, W.H. Schreiner, and D.H. Mosca, *Electrochemical and Solid-State Letters*, **4**(4), C20 (2001).
- [Milazzo78] G. Milazzo and S. Caroli, Tables of Standard Electrode Potentials, John Wiley & Sons Ltd.: New York, NY, 1978.
- [Myung01] N.V. Myung and K. Nobe, *Journal of the Electrochemical Society*, **148**(3), C136 (2001).
- [NDT09] Introduction of Magnetic Particle Inspection, “The Hysteresis Loop and Magnetic Properties.”, *NDT Resource Centre*, Accessed Aug. 17, 2009. <<http://www.ndted.org/EducationResources/CommunityCollege/MagParticle/Physics/HysteresisLoop.htm>>
- [Osaka94] T. Osaka, T. Homma, K. Kageyama and Y. Matsunae, *Denki Kagaku*, **62**(10), 987 (1994).
- [Osaka03] T. Osaka, T. Yokoshima, D. Shiga, K. Imai and K. Takashima, *Electrochemical and Solid-State Letters*, **6**(4), C53 (2003).
- [Osaka07] T. Osaka and J. Sayama, *Electrochimica Acta*, **52**(8), 2884 (2007).

- [Oszkó99] Albert Oszkó, János Kiss and Imre Kiricsi, *Physical Chemistry Chemical Physics*, **1**, 2565 (1999).
- [Pangarov78] N. Pangarov and R. Pangarova. *Journal of Electroanalytical Chemistry and Interfacial Electrochemistry*, **91**(2), 173 (1978).
- [Park05] D.-Y. Park, B.Y. Yoo, S. Kelcher and N.V. Myung, *Electrochimica Acta*, **51**(12), 2523 (2005).
- [Paunovic06] M. Paunovic and M. Schlesinger, Fundamentals of Electrochemical Deposition 2<sup>nd</sup> Edition, John Wiley & Sons Ltd.: Hoboken, NJ, 2006.
- [Pourroy96] G. Pourroy, N. Viart and S. Läkamp, *Journal of Alloys and Compounds*, **244**, 90 (1996).
- [Pourroy98] G. Pourroy, *Journal of Alloys and Compounds*, **278**(1-2), 264 (1998).
- [Pourroy99] G. Pourroy, N. Viart and S. Läkamp, *Journal of Magnetism and Magnetic Materials*, **203**, 37 (1999).
- [Pourroy02] G. Pourroy, A. Valles-Minquez, I.S. Jurca, C. Meny, N. Viart and P. Panissod, *Journal of Alloys and Compounds*, **333**(1-2), 296 (2002).
- [Povetkin96] V.V. Povetkin and O.V. Devyatkova, *Transactions of the Institute of Metals Finishing*, **74**(5), 177 (1996).
- [Puipe80] J.C. Puipe and N. Ibl, *Journal of Applied Electrochemistry*, **10**(6), 775 (1980).
- [Raub67] E. Raub and K. Müller, Fundamentals of Metal Deposition, Elsevier Publishing Company: Amsterdam, 1967.
- [Saxena95] S.K. Saxena, L.S. Dubrovinsky, P. Haggkvist, G. Shen and H.K. Mao, *Science*, **269**(5231), 1703 (1995).
- [Simmonds96] M.C. Simmonds, R.C. Newman, S. Fujimoto and J.S. Colligon, *Thin Solid Films*, **279**, 4 (1996).
- [Specht04] E.D. Specht, P.D. Rack, A. Rar, G.M. Pharr, E.P. George and H. Hong, *Materials Research Society Symposium Proceedings*, **804**, JJ6.3.1 (2004).

- [Specht05] E.D. Specht, P.D. Rack, A. Rar, G.M. Pharr, E.P. George, J.D. Fowlkes, H. Hong and E. Karapetrova, *Thin Solid Films*, **493**, 307 (2005).
- [Shou03] I. Shou, P.M. Vereecken, C.L. Chien, R.C. Cammarata and P.C. Searson, *Journal of the Electrochemical Society*, **150**(3), C184 (2003).
- [Sun98] W. Sun, Electroplating of Gold-Tin Eutectic Solder, a M.Sc. thesis from the University of Alberta, Fall 1998.
- [Sun05] N.X. Sun, S. Mehdizadeh, C. Bonhôte, Q.F. Xiao and B. York, *Journal of Applied Physics*, **97**(10), 10N904 (2005).
- [Tabakovic02] I. Tabakovic, V. Inturi and S. Riemer, *Journal of the Electrochemical Society*, **149**(1), C18 (2002).
- [Tan93] A.C. Tan, Tin and Solder Plating in the Semiconductor Industry: A technical Guide, Chapman & Hall.: London, 1993.
- [Tan90] B.J. Tan, K.J. Klabunde, P.M.A Sherwood, *Chemistry of Materials*, **2**(2), 186 (1990).
- [Thompson00] D.A. Thompson and J.S. Best, *IBM Journal of Research & Development*, **44**(3), 311 (2000).
- [Tochitskii96] T.A. Tochitskii, V.G. Shadrow, L.V. Nemtsevich and A.V. Boltushkin, *Crystal Research and Technology*, **31**(5), 583 (1996).
- [Wang99] S.X. Wang and A.M. Taratorin, Magnetic Information Storage Technology, Academic Press: San Diego, CA, 1999.
- [Xu01] H. Xu, T.E. Dinan, E.I. Cooper, L.T. Romankiw, C. Bonhôte and D. Miller, *Electrochemical Society Proceedings*, **2001-08**, 346 (2001).
- [Zhang04] Y. Zhang and D.G. Ivey, *Chemistry of Materials*, **16**(7), 1189 (2004).
- [Zhang05] Y. Zhang, Electrodeposition of Nanocrystalline CoFe and CoFeNi Soft Magnetic Thin Films from Citrate-Based Baths, a Ph.D. thesis from the University of Alberta, Spring 2005.
- [Zhang07] Y. Zhang and D.G. Ivey, *Materials Science and Engineering*

*B*, **140**(1-2), 15 (2007).

- [Zhou09] S. Zhou, Q. Liu and D.G. Ivey, *IEEE International Nanoelectronics Conference*, #**4585531**, 474 (2008).
- [Zhou09-2] X.S. Zhou, Electrodeposition of Nanocrystalline Co, Fe and CoFe Soft Magnetic Films from Ammonium Citrate Solutions, a M.Sc. thesis from the University of Alberta, Spring 2009.